Memoria de tesis para optar al grado de Doctor

Universidad Autónoma de Madrid

Theoretical description of wave propagation in magnetoplasmonic nanostructures

Blanca Caballero García

Tesis codirigida por los doctores:
Antonio García Martín y Juan Carlos Cuevas Rodríguez

Enero 2016

Instituto de Microelectrónica de Madrid
- Consejo Superior de Investigaciones Científicas -

Para mis padres

Contents

Agradecimientos

Bueno, parece que llegó la hora que pensé que nunca llegaría. Hay que escribir los agradecimientos, lo que quiere decir que la tesis, para bien o para mal, ha llegado a su fin. Cinco años son muchos años y, por tanto, muchas cosas que agradecer, pero desafortunadamente la entrega de la tesis está ya ahí, así que no dispongo de todo el tiempo que me gustaría para hacerlo en condiciones. Mis disculpas de antemano. Veré que puedo hacer.

Lo primero, quería agradecer enormemente a mis directores de tesis Antonio y Carlos porque sin ellos esto no hubiera sido posible. Gracias por estar siempre disponibles, por sacar siempre tiempo para ayudar, por tener siempre la puerta abierta de vuestro despacho para cualquier pregunta y por este último esfuerzo de corregirme la tesis en vuestras vacaciones, incluso a las hora más insospechadas. Gracias a Carlos por los dos primeros años en la Autónoma, porque gracias a ti y tu manera de hacer buena ciencia, me decidí a embarcar en la aventura del doctorado. Gracias por esa facilidad para escribir que tan útil ha sido y que nunca tendremos el resto. ¡Yo de mayor quiero ser como tú! Ahora Antonio, voy contigo. Contigo he estado los tres últimos años en el IMM y de verdad que ha sido todo un placer haber trabajado contigo. En lo profesional sobran palabras, pero me gustaría hacer hincapié en lo personal. Gracias por preocuparte por mi en todo momento, ¡si es que estás hecho un amor! Jeje. Gracias por eso cafés que siempre amenizan el día y por escucharme mis tonterías cuando estoy cansada. Estoy segura de que no volveré a tener un jefe como tú.

Prosigo recordando mis años en la UAM, porque la verdad que nunca me lo he pasado tan bien trabajando como cuando estaba en el despacho 401. Gracias a mis compañeros de despacho: Andrei, por los tiempos felices vividos juntos; Carlos y Diego, porque no me he reido tanto como con vosotros; Jesús y Lucía, porque por un tiempo tuve la suerte de tener en el trabajo a dos de mis mejores amigos. Del resto del departamento mención especial requieren Alex y Colin, aunque por razones muy dispares. Colin, te agradecería por hacer más entretenidas las comidas en la Autónoma

con interesante discusiones pero sobre todo te voy a agradecer tu gran aportación en Facebook, tus post son mis highlights de noticias, gracias a ti he conseguido hacer una tesis y estar muy bien informada al mismo tiempo. También quería agradecerle a Alex, quizás nunca se lo dije, y quizás nunca leerá esto pero me sentí muy apoyada por él en un momento difícil de mi doctorado y esas cosas quedan ahí, ¡gracias!

Por lo que respecta a mi paso por el IMM tengo que agradecer a mucha gente desde los otros miembros de mi grupo, coautores de dos de mis artículos: Alfonso, Gaspar, Mariau, Meneses...; hasta todos los diferentes compañeros de despacho que he tenido: Botitas, Elías, Horacio, Huayu, Jorge, Marcos, Pedro... Pero sobre todo a mis compis de desayunos y comidas, porque sin su compañía sería mucho más difícil trabajar en el IMM: Carmen, Dani (ahora voy contigo), Estela, Etor, Lorena, Malvi, Margarita y Raquel. Una especial mención merece Patricia que, aunque ahora esté más fuera que dentro, fue mi primer gran apoyo en el IMM y ahora una gran amiga ¡Gracias por estar siempre ahí!

Ahora Dani, ya que he empezado contigo, te toca a ti. Miles de gracias por... TODO. Si bien he dicho antes que esta tesis en su conjunto no hubiera sido posible sin la ayuda de mis directores de tesis, sólo tú bien sabes que la entrega del manuscrito a tiempo en gran parte te lo debo a ti. Gracias por tu ayuda en todo momento, por tu apoyo incondicional, por siempre creer en mi y trasmitirme esa confianza. Por eso y por muchas más cosas, es un placer estar a tu lado. Gracias.

No quiero olvidarme de agradecer a mis amigos. A los de Física: Elena, Emilio, Irene, Nacho, Jesús y Lucía (sí, de nuevo, ¿por qué no?) Siempre es un placer compartir ratos con vosotros, espero que cuando todo esto acabe sean mucho más frecuentes. Por otro lado cómo no, a mis amigas del cole Agos, Paula y Vane. Ya son muchos años y saber que sigo pudiendo contar con vosotras es lo mejor que podría tener. Da igual que estéis aquí o en las chimbabas, siempre seréis una parte muy importante de mi vida. ¡Os quiero!

Como lo mejor siempre se deja para el final, quiero terminar agradeciendo a mi familia. Primero a la extendida, tíos, primos y abuela; Chilindrines y no Chilindrines. ¡Me encanta pasar tiempo con vosotros! Todo es mucho mejor sabiendo que estáis ahí, aunque sea por "la family". Chema, dentro de poco ya podremos hacer cabecera de doctores en las cenas, jeje.

Por último a mis padres. Papás, gracias. Una gran parte de mis logros es también vuestra, porque sin vosotros no sería la persona que soy. ¡Ay qué me emociono! Gracias por haberme dado las herramientas necesarias que

me han permitido llegar hasta aquí hoy. A vosotros os debo todo. ¡Sois los mejores del mundo!

Hay una frase por ahí de Rousseau que dice: "las cartas de amor se escriben empezando sin saber lo que se va a decir, y se terminan sin saber lo que se ha dicho." Pues bien, esta debe ser mi carta de amor para todos vosotros porque así me siento yo ahora mismo. ¡Gracias a todos!

Resumen

Desde hace algunas décadas estamos presenciando una carrera imparable por desarrollar dispositivos tecnológicos cada vez más pequeños, rápidos y eficientes. En este contexto surgen los dispositivos fotónicos como una alternativa muy atractiva debido a que aúnan una gran velocidad de transferencia de información y un ancho de banda, en principio, ilimitado. No obstante, dichos dispositivos aún tienen que solventar ciertos problemas para ser tecnológica y económicamente viables, siendo probablemente la miniaturización de los componentes por debajo del límite de difracción de la luz el más importante de todos. En este sentido, la opción más prometedora para confinar y manipular la luz a escala nanométrica es la excitación de plasmones de superfice, modos electromagnéticos originados por la interacción de la luz y los electrones libres de la superficie de un metal (SPP por sus siglas en inglés *"Surface Plasmon Polariton"*). Para alcanzar el nivel de control que requieren estos nuevos dispositivos, se necesita poder actuar directamente sobre los modos confinados en la superficie de forma externa y controlada. La forma más sencilla de lograrlo es, probablemente, la aplicación de un campo magnético externo, dando como resultado un nuevo campo de estudio que se conoce como magnetoplasmónica. En vista de las prometedoras posibilidades que ofrecen estos sistemas, la presente tesis doctoral está dedicada al estudio teórico de la propagación de ondas en sistemas magnetoplasmónicos.

Empezaremos esta tesis doctoral haciendo una breve introducción al concepto de SPP detallando su relación de dispersión. Tal y como se explica en el texto, para lograr excitar el SPP se tiene que cumplir la conservación de momento, por lo que debemos aportar un vector de onda extra paralelo a la superficie. Aunque existen diferentes alternativas en la literatura para conseguir acoplar el vector de onda incidente y excitar así el plasmón hemos elegido la nano-estructuración de la superficie mediante una red periódica de agujeros nanométricos (de tamaño menor que la longitud de onda de la luz). Continuaremos estudiando los efectos que tiene sobre las propiedades ópticas del sistema la presencia de un campo magnético externo; en concreto, nos centraremos en estudiar el efecto en la intensidad y polarización de la luz transmitida y reflejada, lo que se

conoce como efectos Faraday y Kerr para diferentes configuraciones de campo.

El desarrollo teórico que hemos llevado a cabo para describir la propagación de ondas en sistemas de multicapas nano-escructuradas periódicamente se basa en el método de la matriz de *scattering*. Aunque este método se ha utilizado anteriormente para estudiar la actividad magneto-óptica en estructuras formadas por multicapas planas, su aplicabilidad estaba restringida a configuraciones geométricas concretas, no pudiéndose utilizar, por ejemplo, para explicar los efectos Faraday y Kerr en configuración transversal. El problema radica en que la propagación de los estados propios en las diferentes capas, no se puede resolver como un problema de valores propios estándar. Por tanto, cuando la anisotropía óptica de los materiales incluye elementos fuera de la diagonal del tensor dieléctrico todos los métodos anteriores fallaban. A lo largo de la presente tesis doctoral se ha desarrollado una generalización del método de la matriz de *scattering* que resuelve este problema describiendo la actividad magneto-óptica en sistemas nano-estructurados para cualquier configuración utilizando la expansión en componentes de Fourier del tensor dieléctrico; en concreto, nos centraremos en el estudio de membranas magnetoplasmónicas perforadas de forma periódica.

Los metales ferromagnéticos como el hierro, el níquel o el cobalto constituyen una opción muy interesante ya que presentan una actividad magneto-óptica muy importante incluso bajo campos magnéticos relativamente pequeños, y al mismo tiempo todavía soportan la excitación de un plasmón de superficie. Utilizando el método desarrollado anteriormente, analizaremos desde el punto de vista teórico las medidas experimentales realizadas por nuestros colaboradores en Suecia y Alemania del efecto Kerr magneto-óptico en configuraciones polar y transversal de membranas de hierro y níquel con una matriz hexagonal de agujeros, llegando a la conclusión de que el origen del aumento en la actividad magneto-óptica radica en la excitación de los SPPs. Posteriormente, estudiaremos las implicaciones de la geometría de la red en dichas membranas variando el tamaño de los agujeros.

Con el fin de mejorar las propiedades de nuestras membranas, se ha optado por utilizar sistemas híbridos que aúnen las capacidades magneto-ópticas de los materiales ferromagnéticos con las buenas propiedades de los SPPs que presentan los metales nobles. Para esto se han estudiado membranas híbridas formadas por multicapas de oro – cobalto – oro con agujeros nanométricos dispuestos de forma periódica. Tal y como se explica en el texto, estos sistemas híbridos mejoran la eficiencia como rota-

dores de Faraday presentando al mismo tiempo una alta transmitancia.

Del mismo modo, vemos que el efecto Kerr transversal magneto-óptico (TMOKE por sus siglas en inglés *"Transverse Magneto-Optical Kerr Effect"*) aumenta drásticamente debido a la interacción de las propiedades magneto-ópticas de la membrana ferromagnética y de las propiedades plasmónicas de los metales nobles. Se propone entonces el uso de dichas membranas híbridas como transductores en sensores magneto-ópticos de resonancia de plasmón superficial. La respuesta magneto-óptica de estos sistemas se caracteriza por una curva de Fano muy estrecha que es extremadamente sensible a cambios en el índice de refracción del entorno, lo que da como resultado una figura de mérito varios órdenes de magnitud mayor que el estado del arte actual en este tipo de sensores basados en resonancia de plasmones.

1 Introduction

1.1 Motivation and scope of the thesis

In the last decades, we have witnessed an inexorable progress towards smaller, faster and more efficient technological devices. Until very recently, semiconductor electronic devices comfortably complied with society demands and thus became over the last five decades the first choice for technological applications. Nevertheless, nowadays state-of-the-art electronic devices are unavoidably approaching their intrinsic limitations in some important aspects such as speed or bandwidth, which is an increasing problem that prevents further advances in many areas of modern technology [1]. Photonic devices, on the other hand, posses an extraordinarily large data carrying capacity since they are not handicapped by the same speed or bandwidth limitations [2]. Thus, in recent years, light has been postulated as the most promising alternative in replacing electronic signals [1–3]. However, when using electromagnetic (EM) waves as information carriers there is still a major issue that is crucial to address, that is miniaturization. It is not possible to concentrate light in dielectric media beyond the diffraction limit [4] and, consequently, one cannot straightforwardly manipulate light at the nanometer scale, which is of essential importance to facilitate transport between electronic and photonic devices.

In this context, the excitation of surface plasmon polaritons (SPPs) [5,6], which are EM modes caused by the interaction between light and the free electrons at the surface of a metal, is likely the most feasible solution to concentrate and manipulate light at the nanoscale [1,3,7,8]. By squeezing light into subwavelength volumes, plasmonic metallic nanostructures can efficiently mediate interactions between propagating EM waves and nanoscale objects and devices. The efforts to understand these SPPs and the search for applications have resulted in a flourishing new field of science and technology, recently termed plasmonics [6,7]. The first investigations related to plasmonic effects took place over one hundred years ago [9,10] and it was back in the 1950's when several theoretical studies

led to a complete understanding of the phenomenon [11]. However, it has been during the last two decades when the field of plasmonics has become more relevant thanks to the advances in the fabrication techniques at the nanoscale. These advances in nanofabrication have permitted to take advantage of the unique ability of metallic nanostructures to concentrate light beyond the diffraction limit, making plasmonics the technology of choice for multiple applications. Thus, SPPs have shown to be a strong candidate for development of integrated nanophotonic devices, being able to bridge the gap between photonics and electronics [3]. On top of that, they have induced a significant progress in many other techniques and applications such as spectroscopy [12], sensing [13, 14] or solar cells [15], to name just a few.

In the search for applications, science and technology have put much effort in finding ways of tuning and modulating light propagation. In this way, plasmonics has made use of the nanostructuration of metals to couple light to SPPs and to guide it into reduce volumes. However, this approach by itself results in a passive control of the SPPs, which is not enough for some applications such as, for instance, modulators or switches of nanophotonic circuits that require an active control of their properties by an external agent. Thus, in the last years, important progress has been made to achieve active plasmonic configurations based on different controlling agents such as temperature [16, 17], voltage [18, 19] or photons [20–23]. Of particular interest is the possibility to actively influence the plasmonic modes [24–28] and the optical properties [29–32] of metallic structures with an external magnetic field, which has resulted in a whole new field known as magnetoplasmonics [33,34]. Among other approaches, controlling SPPs with a magnetic field has always occupied an important place since it is proven to be an ultrafast easy-to-use technique, capable of reaching switching speeds of femtoseconds [35], making magnetoplasmonics an attractive solution.

Magnetoplasmonics studies the effects arising from the interplay between the excitation of SPPs and the magneto-optical (MO) phenomena typically occurring in nanostructures that combine metallic and magnetic elements in the same structure. In this field, as we mentioned above, one of the central ideas is to control light propagation via the modification of the plasmon properties using an externally applied magnetic field. Nonetheless, it is not the only advantage that magnetoplasmonics offers. The consequent concentration of the EM field, caused by the excitation of SPPs, leads in turn to a significant enhancement of the MO response of the system [24, 28, 36]. This latter property is also very appealing since it can

be exploited in many applications where magneto-optics plays a relevant technological role such as telecommunications [25, 37], data storage [35] or sensing [37–42]. For that reason, many works have been focused on the development of new materials and nanostructures that offer large MO activity and low losses so that they can improve the performance of such devices.

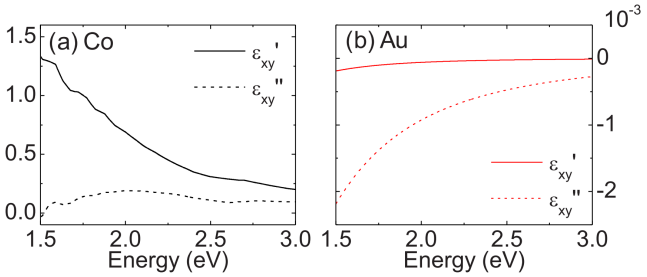

Figure 1.1: Real and imaginary part of the MO constants of (a) Co and (b) Au. As we will see in sec. 2.2, the MO constants are directly related to the MO activity. For Co, these constants were experimentally obtained whereas those for Au were obtained through a Drude model calculation considering an applied magnetic field of 1 T. We see that for reasonable magnetic fields, the MO constant of a noble metal (Au) are three orders of magnitude smaller that the ones for a ferromagnetic metal (Co). Figure from Ref. [43], reproduced with permission. Copyright 2010, American Institute of Physics.

To obtain the best results, magnetoplasmonic systems incorporate strong magneto-optically active materials, such as ferromagnets. Ferromagnetic materials are characterized by having large MO activity associated with their magnetization in presence of reasonable small magnetic fields [34] (see Fig. 1.1(a)). However, although ferromagnetic metals sustain SSPs, due to their intrinsic high absorption, the associated plasmon resonances are too broad and the propagation losses are too high, to be employed in practical devices. On the other hand, noble metals, which are the materials usually employed in plasmonics, are characterized by very well defined plasmonic resonances. However, they present the drawback that extremely high magnetic fields (of tens of Tesla) are necessary to have appreciable MO effects [34] (see Fig. 1.1(a)). As a consequence, the combination of both magneto-optically active materials and noble metals in a variety of nanostructures has been presented as a solution to maximize the trade-off between large MO activity and fair plasmon resonances. In these hybrid magnetoplasmonic systems, the excitation of low-loss SPPs in the noble metal enables a concentration of the EM field in the interior of the structure, more concretely, in the region where the magneto-optically

active component is present. This local concentration of the EM field inside the ferromagnetic material results in an enhancement of the different MO effects such as the polar MO Kerr effect [31, 43, 44], the Faraday effect [31, 45–47] or the transverse MO Kerr effect [28, 48] (see sec. 2.2 for a description of the MO effects), which makes hybrid magnetoplasmonic nanostructures very attractive for technological applications.

In view of the possibilities that these hybrid magnetoplasmonic nanostructures offer, and in order to guide their design, it is absolutely crucial to have theoretical methods that are able to accurately describe the propagation of waves in such systems. However, in spite of the numerous existent theoretical methods for the description of the optical response of nanostructures [49], at the beginning of this thesis there was no theoretical approach that could provide a unified description of the different MO effects that occur in nanostructured magnetoplasmonic devices. Previous works had been carried out to extend the so-called scattering-matrix formalism [50–52] in order to describe different magneto-optical effects [53] and to study certain types of anisotropic media [54] in nanostructured multilayer structures. However, there were still basic magnetic configurations, such as transversal or longitudinal, that were out of the scope of those works. In order to fill that gap, we present in this thesis a generalization of the scattering-matrix formalism that enables the description of the MO effects in hybrid nanostructured systems with arbitrary combination of materials and in any possible configuration of the external magnetic field. This tool will allow us to focus on the theoretical study of magnetoplasmonic nanostructures and the intertwined effects that plasmonics and magneto-optics offer from both fundamental and applied viewpoints, making special emphasis on the enhancement of the MO activity due to plasmon excitation. To be more precise, the magnetoplasmonic systems that we have chosen as a subject of study for this thesis are metallic films perforated with periodic arrays of subwavelength holes.

Metal nanohole arrays, also known as plasmonic crystals, are a paradigmatic structure in the field of plasmonics (see Fig. 1.2). As we will see in detail in the next chapter (sec. 2.1.2), the periodicity of these systems provides the extra momentum necessary to facilitate the coupling between light and the surface plasmon resonances. Nonetheless, their relevance not only resides in their facility to support the excitation of SPPs but also in their ability to present what is known as extraordinary optical transmission (EOT) [55, 56]. EOT was reported for the first time in 1998 by T. W. Ebbesen and coworkers [56]. Their observations indicated that the amount of light transmitted at certain wavelengths through periodic

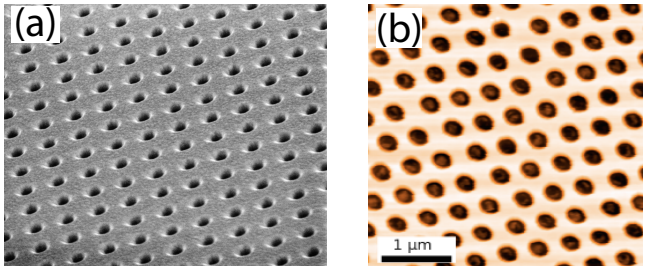

Figure 1.2: (a) SEM image of a nanohole array of circular holes of diameter of 150 nm milled in a 260 nm thick Au film that is deposited on a glass substrate. The period of the square array is 460 nm. Figure adapted from Ref. [55], reproduced with permission. Copyright (2010) by The American Physical Society. (b) AFM image of a Co film perforated with an hexagonal array of subwavelength holes. Courtesy of E. Th. Papaioannou.

arrays of subwavelength holes perforated in an otherwise opaque metal film was orders of magnitude larger than that predicted by the classical Bethe's aperture theory (see Fig. 1.3). Furthermore, more light was transmitted than the actual amount that impinged on the hole area. This unusual phenomenon was attributed to the excitation of SPPs [55–57]. The discovery represented a milestone for the field of optics and laid the foundations for modern plasmonics. Since then, extensive research on the topic of plasmonic crystals has been carried out [55,58,59], including later investigations about their MO activity led by experiments conducted on ferromagnetic nanohole arrays [60–63]. These experiments show that an enhancement of the MO response of these systems is possible thanks to the ability of periodic nanohole arrays to sustain surface plasmon resonances. As we mentioned previously, the enhancement of the MO activity of the system is clearly a property that might be useful for technological applications and, moreover, it is not the only one that nanohole arrays might offer. Other clear examples are their ability to confine light at the nanoscale, the possibility of tailoring the transmission properties at a desired wavelength by changing the structural parameter of the array or their sensibility to changes in the refractive index of the surrounded media. All of them have already made metal nanohole arrays very suitable candidates for a vast variety of applications [59].

Although it is known that the hybridization of ferromagnetic materials with noble metals enhances the MO activity of magnetoplasmonic systems [36, 43, 44, 64], to the best of our knowledge, there are no previous studies of hybrid subwavelength-hole periodic arrays. As the ultimate goal of this thesis we want to propose a system that will allow us to

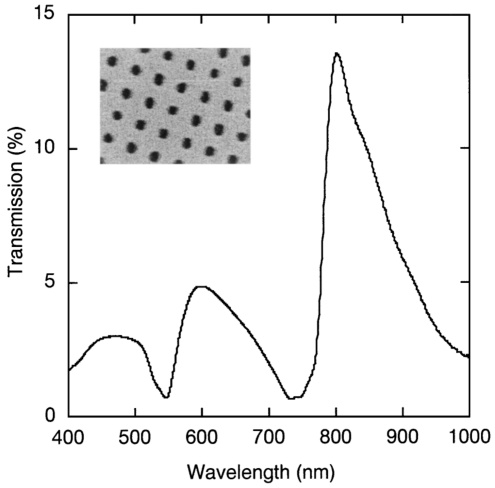

Figure 1.3: Illustration of the phenomenon of extraordinary optical transmission. The curve represents the experimental zero-order transmittance at normal incidence for a square array of holes (lattice constant of 750 nm, average hole diameter of 280 nm) in a freestanding Ag film (thickness of 320 nm). Inset: electron micrograph of the perforated metal film. Figure from Ref. [57], reproduced with permission. Copyright (2001) by The American Physical Society.

go further in the study of magnetoplasmonic nanostructures and, at the same time, that we foresee it will be very profitable for technological applications. The system put forward consists of a trilayer of noble metal-ferromagnetic-noble perforated with a periodic array of subwavelength holes (see Fig. 1.4), where we will show that it is possible to boost the magnetoplasmonic properties of the already profitable metal nanohole arrays, leading to unprecedented figures of merit in the field of refractive index sensors.

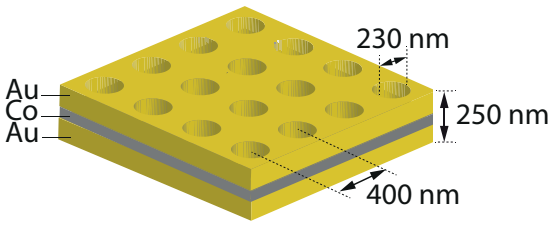

Figure 1.4: Schematic representation of the system under study, an Au-Co-Au perforated membrane with a periodic array of circular holes forming a square lattice.

1.2 Objectives

As we mentioned in the previous section, an important part of this thesis is devoted to the developement of a theoretical tool that enables the description of MO effects in magnetoplasmonic nanostructured systems for every possible magneto-optical configuration. Afterwards, with the help of this tool, we will focus on the analysis of the magneto-optical response of metal films perforated with arrays of subwavelength holes, being the ultimate goal of this thesis the study of hybrid nanohole arrays comprising ferromagnetic and noble metals both from the fundamental and applied points of view. With this in mind, we set four objectives for this thesis:

1. **Generalization of the scattering matrix approach**. This is the major technical challenge of this thesis and it is essential for achieving the other objectives. The generalization of the scattering-matrix approach will enable us to describe all the optical and MO effects of periodically nanostructured multilayer systems with arbitrary combination of materials and in any possible configuration of the external magnetic field. In particular, this generalization will allow us to describe the transverse MO Kerr effect, which cannot be addressed with any other existent theoretical techniques.

2. **Description of the MO effects of experiments performed in ferromagnetic nanohole arrays.** Making use of the theoretical tool previously described we will address the MO description of experiments conducted on ferromagnetic nanohole arrays in polar and transversal configurations. Specifically, we will focus on the intertwined effects that SPPs have on the magneto-optics of these systems. Let us remind that this fact is of particular relevance since the study of the transverse MO Kerr effect in such membranes remained without a rigorous theoretical description.

3. **Investigation of the interplay between extraordinary optical transmission and magneto-optics in hybrid nanohole arrays.** Our main interest is to study, making use of the generalized scattering-matrix formalism, the enhancement of the MO effects for transmitted waves, i.e. the Faraday effect, when nanohole arrays exhibit EOT. With this in mind, our subject to study will consist of a periodically perforated trilayer of noble metal-ferromagnetic-noble metal as in Fig. 1.4 where we expect that, upon a suitable combination of materials, the presence of the noble metal increases

both the transmission and MO activity of the system, as compared to purely ferromagnetic membranes. It is worth remarking that, despite the fact that the Faraday effect of hybrid systems exhibiting EOT has been previously investigated [31, 45–47], this is the first study where the MO activity resides inside the nanostructured part of the system.

4. **Design and optimization of novel surface plasmon resonance sensors based on the transverse MO Kerr effect in hybrid nanohole arrays.** Surface-plasmon-resonance (SPR) sensors, via measurements of reflection or transmission, are able to detect local variations of refractive index within the evanescent field of the surface plasmon in real time. Following this idea, though in this case measuring the changes on the MO signals, hybrid ferromagnetic-noble metal multilayers of nanometric thicknesses have been shown to improve the sensitivity of conventional SPR sensors by up to a factor of three [37–42]. The challenge of this thesis is to improve even further the sensitivity of magneto-optical surface-plasmon-resonance (MO-SPR) sensors by using the same hybrid magnetoplasmonic nanohole arrays as above. These periodic systems should lead, in principle, to an even more enhanced transverse MO Kerr effect. Thus, by using the generalized scattering matrix formalism, we shall investigate the performance of these systems as novel MO-SPR sensors. The goal is to guide the design of these sensors by providing the optimal combination of materials, the type of periodicity to be built in, the dimensions of the hybrid structures, etc.

1.3 Overview of the contents

We have seen previously how the upcoming technological applications require the control and modulation of light propagation, which lead to the necessity of actively influence the plasmonic modes and optical properties of nanostructured materials. In this regard, the use of magnetic fields has revealed as an attractive option due to its speed and versatility. The work presented here is somehow complimentary to the previous studies in magnetoplasmonics referenced above. In what follows, we proceed to give a general overview of the contents of the thesis.

An overview of the definition of SPP and its dispersion relation are included in Chapter 2. In order to provide the required extra momentum to fulfill the matching condition to excite a surface plasmon we have chosen

the periodically patterning of metallic films by arrays of sub-wavelength holes. With this in mind, we present the explicit matching condition, which is the conservation of the parallel wave vector, for the excitation of SPPs for different periodic arrays. Subsequently, dissertation continues studying how the optical properties of a system are affected by the presence of an external magnetic field. In particular, the intensity and polarization of the transmitted and reflected light, known as the Faraday and Kerr effects, are discussed in detail for different configurations.

Chapter 3 establishes the theoretical framework to describe the wave propagation in periodically patterned multilayer systems. Although there were previous studies in which the scattering matrix formalism was successfully extended to study MO activity in multilayer structures, there are still basic physical problems, like Kerr and Faraday effects in transverse configuration, which are beyond those versions of the scattering matrix method. The difficulty lies in the fact that the propagating eigenstates in the different layers cannot be simply described with a standard eigenvalue problem. Therefore, when the optical anisotropy of the materials involves off-diagonal elements of the permittivity tensor none of the prior existing implementations of the scattering matrix method are valid. This chapter introduces a generalization of the scattering-matrix technique to describe the MO of nanostructured systems in any configuration. Moreover, we present the implementation of the fast Fourier factorization that assures a fast convergence of the method.

The thesis continues with the study of magnetoplamonic nanohole arrays. Since ferromagnetic metals such as Fe, Ni or Co present a strong MO activity under low magnetic fields while supporting SPPs, Chapter 4 explores the ferromagnetic nanohole arrays theoretically analyzing three different experimental measurements (performed by our collaborators in Sweden and Germany) of transverse and polar MO Kerr effects. We show that the SPPs are responsible for the MO activity enhancement in periodic arrays of Fe and Ni and shed light on the role played by the geometry of the periodic pattern by studying the influence of the size of the holes on the polar MO Kerr effect.

Chapter 5 fills the gap existing in literature presenting an exhaustive study of the Faraday effect in nanohole arrays comprising both a ferromagnetic material and a noble metal. We will show that the use of hybrid Au-Co-Au trilayers perforated with two-dimensional periodic arrays of sub-wavelength holes improves the performance as Faraday rotators exhibiting a high transmittance and high Faraday rotation.

The same hybrid nanohole arrays are studied in Chapter 6, where we show that the transverse magneto-optical Kerr effect is also largely enhanced due to the interplay between the MO properties of the ferromagnetic membrane and the plasmonic properties of the noble metals. The hole-patterned Au-Co-Au films are proposed as transducers in MO surface plasmon resonance sensors. The MO response of these systems is characterized by a sharp Fano-like line shape that is very sensitive to refraction index variations, resulting in a sensing figure of merit that is several orders of magnitude larger than the one of state-of-the-art surface plasmon resonance based sensors.

2 Fundamental concepts

As we mentioned in the introduction, the work presented in this thesis is framed within the research area known as magnetoplasmonics, which deals with the interplay between plasmonics and magneto-optics [34]. Before going deeper into the discussion of the novel results presented in this thesis, we would like to review some basic notions on these two topics. Thus, in this chapter we introduce some key elements and concepts related to surface plasmons and magneto-optics that are necessary for the understanding of this thesis.

2.1 Surface plasmons polaritons

A surface plasmon is a collective excitation of the electrons at the interface between two media with permittivities of opposite sign, usually a dielectric and a metal [5, 6]. They are electromagnetic modes bounded to the surface, that arise from the interaction between light and the free electrons of a metal, resulting in a confinement of the EM field of light. Depending on where these modes are present, surface plasmons can be classified into two main categories: localized surface plasmons (LSPs) and propagating surface plasmons or surface plasmon polaritons. LSPs appear in isolated particles of dimensions of the order or smaller than the wavelength of the exciting light, such as metal nanoparticles [12, 65, 66]. On the contrary, SPPs are sustained at the interface of extended planar films [5, 7]. Since LSPs are out of the scope of this thesis, in this section we will exclusively focus on the description of propagating surface plasmons or SPPs, with particular emphasis on the excitation of SPPs in periodically patterned films.

2.1.1 SPP characteristics and dispersion relation

Let us briefly recall the characteristics of a SPP that propagates along a flat interface between a dielectric and a metal of permittivities ϵ_d and ϵ_m,

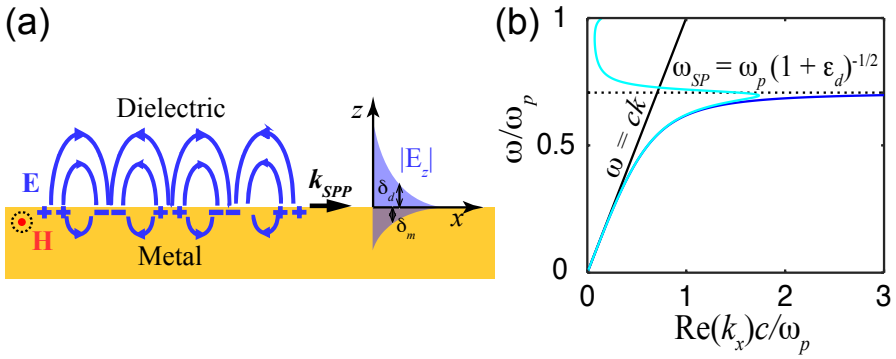

Figure 2.1: (a) Scheme of the propagation and electromagnetic field of a SPP. (b) Dispersion relation of a metal-air SPP for an ideal metal (dark blue line) and a metal with absorption (light blue line). Solid black line represents the light line while dotted line indicates the surface plasmon frequency.

respectively. SPPs are modes that propagate along the surface and are confined in the perpendicular direction. They are transverse magnetic electromagnetic waves, which means that the magnetic field, **H**, is perpendicular to the direction of propagation, and are evanescently confined to the surface since the electric field perpendicular to the surface, E_z, is exponentially decaying (see Fig. 2.1(a)). In the visible range, the penetration depth into the dielectric, δ_d, is of the order of one wavelength, while the penetration depth into the metal, δ_m, is hardly few tens of nanometers [67].

If we apply Maxwell's equations to a flat interface between a dielectric medium ($\epsilon_d > 0$) and a metal ($\mathrm{Re}(\epsilon_m) = \epsilon'_m < 0$), under appropriate boundary conditions, we find a surface mode solution with the well-known SPP dispersion relation [5]

$$k_{\mathrm{SPP}} = k_0 \sqrt{\frac{\epsilon_d \epsilon_m}{\epsilon_d + \epsilon_m}}. \tag{2.1}$$

where k_0 is the free space wave vector, and is given by $k_0 = \omega/c = 2\pi/\lambda$, being ω, c and λ the frequency, the speed of light and the vacuum wavelength, respectively. Due to the absorption in metals, since $\mathrm{Im}(\epsilon_m) = \epsilon''_m \neq 0$, k_{SPP} is in general a complex quantity. Assuming that ϵ_d is real and that $\epsilon''_m \ll \epsilon'_m$, real and imaginary parts of Eq. (2.1) can be expressed

as [5]

$$\mathrm{Re}(k_{\mathrm{SPP}}) = k_0 \sqrt{\frac{\epsilon_d \epsilon'_m}{\epsilon_d + \epsilon'_m}}, \tag{2.2}$$

$$\mathrm{Im}(k_{\mathrm{SPP}}) = k_0 \frac{\epsilon''_m}{2\left(\epsilon'_m\right)^2} \left(\frac{\epsilon_d \epsilon'_m}{\epsilon_d + \epsilon'_m}\right)^{3/2}. \tag{2.3}$$

The imaginary part of the wave vector, Eq. (2.3), is related to the attenuation that the EM field of a SPP suffers while it propagates and is inversely proportional to its propagation length, so that $L_{\mathrm{SPP}} = 1/2\mathrm{Im}(k_{\mathrm{SPP}})$. The distance L_{SPP} is usually of the order of micrometers in a real metal [67]. On the other hand, the real part of the SPP wave vector, Eq. (2.2), is related to the phase velocity of the wave and, as we explain in the following section, gives the matching condition for the excitation of the SPP. In Fig. 2.1(b), $\mathrm{Re}(k_{\mathrm{SPP}})$ is depicted for an interface between air, $\epsilon_d = 1$, and a metal with permittivity described by the Drude model, $\epsilon_m(\omega) = 1 - \omega_p^2/(\omega^2 - i\gamma\omega)$, where ω_p and γ are the plasma and damping frequency, respectively. Dark blue line shows the dispersion relation for an ideal metal, where there is no absorption so $\gamma = 0$ and $\epsilon''_m = 0$. In this case, for small wave vectors corresponding to low frequencies, k_{SPP} behaves similarly to the dispersion relation of light ($\omega = ck$, solid black line). For large wave vectors, the frequency of SPP has an asymptotic behavior towards the characteristic surface plasma frequency $\omega_{\mathrm{SP}} = \omega_p/\sqrt{1+\epsilon_d}$ (black dotted line). Light blue line represents a damped SPP in a real metal ($\gamma \neq 0$ and $\epsilon''_m \neq 0$). We show that the bound SPP now approaches a maximum wave vector at the surface plasmon frequency, ω_{SP}. Above ω_{SP} the mode becomes leaky or radiative since the region of confinement of the EM wave is now larger than the wavelength, i.e., we do not have a bound mode any more [6].

2.1.2 Excitation of SPPs in periodic arrays

As we just mentioned, the condition to excite a plasmon at a metal-dielectric interface is given by the real part of the SPP wave vector or $\mathrm{Re}(k_{\mathrm{SPP}})$. Since the component of the wave vector parallel to the interface is always conserved, the magnitude of the parallel wave vector of the incoming wave has to be equal to $|\mathrm{Re}(k_{\mathrm{SPP}})|$ in order to get the excitation of the sought SPP mode. In Fig. 2.1(b), we can see that it is not possible to fulfill the matching condition by impinging light from the air, as the

dispersion relation for the bound mode is always to the right of the light line, $\mathrm{Re}(k_{\mathrm{SPP}}) > k_0 = \omega/c$, being k_0 the momentum of light in free space. Thus, it is crucial to find different configurations to overcome this mismatching situation. There are several techniques that provide the required extra momentum to the system to get the surface plasmon excitation [5,6,68] such as impinging from a dielectric prism (Otto [69] or Kretschmann [70] configurations), through the scattering of a defect at the surface [71] or nanostructuring the surface in a periodic pattern [7]. This thesis is devoted to the study of periodic nanohole arrays, subsequently, in this section we proceed to discuss the details of the excitation of SPP in a periodic lattice.

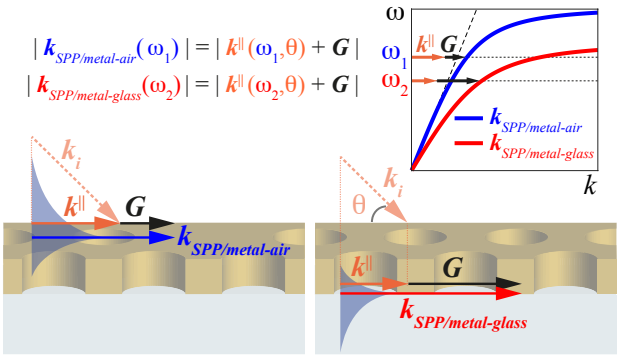

Figure 2.2: SPPs excitation in nanohole arrays. Dispersion relation and schematic representation of the excitation of SPPs at the interfaces metal-air (incident medium) and metal-glass (substrate).

In a periodic array, the extra momentum necessary to match the condition of the SPP excitation is given by the reciprocal vectors of the periodic lattice, $\mathbf{G}_{ij}$ (see Fig. 2.2). These SPP modes are known as **Bragg plasmons**. For a flat interface between a periodically nanostructured metal of wavelength-dependent permittivity $\epsilon_m(\lambda)$ and a dielectric of permittivity ϵ_d, the matching condition for the excitation of the SPPs is, in a first approximation, given by [5]

$$|\mathrm{Re}\left\{k_{\mathrm{SPP}}(\lambda_{ij})\right\}| = |\mathbf{k}_{||} + \mathbf{G}_{ij}|, \tag{2.4}$$

where $\mathbf{k}_{||} = n_i(2\pi/\lambda)\sin\theta\hat{\mathbf{x}}$ is the in-plane wave vector of the incoming light from a medium of refractive index, n_i, with an angle of incidence θ. We shall emphasize that, in nanohole arrays, both interfaces on either side (incident media-metal interface or substrate-metal interface) may sustain SPPs, which are usually excite at different frequencies (wavelengths) depending on the permittivity of the material in immediate contact, ϵ_d.

Eq. (2.4) is intended to give us at which (discrete) wavelengths can the Bragg plasmons be excited for a given angle of incidence. Notice that this approximation takes the dispersion relation $k_{\mathrm{SPP}}(\lambda_{ij})$ of a SPP for a flat interface metal-dielectric, Eq. (2.2), and thus neglects the presence of the holes and their associate scattering losses. As a consequence, predictions of the surface plasmon resonances of a nanohole array are always slightly shifted to lower wavelengths [58]. Nevertheless, most of the time this is an acceptable approximation to understand the physics of the system.

Bragg plasmons in hexagonal and square lattices

Here, we introduce the explicit expressions of the Bragg plasmon matching condition of Eq. (2.4) for hexagonal and square lattices since these two lattices will be discussed throughout this thesis. Our choice for the corresponding real $(\boldsymbol{a}_1, \boldsymbol{a}_2)$ and reciprocal $(\boldsymbol{b}_1, \boldsymbol{b}_2)$ lattice basis vectors are shown in Fig. 2.3.

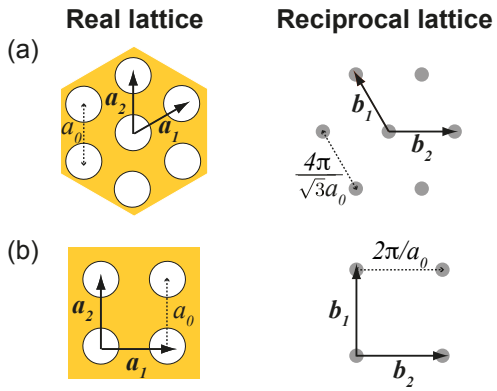

Figure 2.3: Real and reciprocal lattices for (a) a hexagonal lattice and (b) a square lattice.

For a **hexagonal lattice,** for our choice of basis vectors, a reciprocal lattice vector is described by $\mathbf{G}_{ij} = i\boldsymbol{b}_1 + j\boldsymbol{b}_2 = (2\pi/a_0\sqrt{3})\{(2j-i)\hat{\mathbf{x}} + i\sqrt{3}\hat{\mathbf{y}}\}$ (see Fig. 2.3 (a)). Consequently, the matching condition of Eq. (2.4) can be written as

$$n_i^2 \sin^2\theta + (2j-i)\frac{2\lambda}{\sqrt{3}a_0} n_i \sin\theta + (i^2+j^2-ij)\frac{4\lambda^2}{3a_0^2} - \frac{\epsilon_d \epsilon'_m}{\epsilon_d + \epsilon'_m} = 0. \quad (2.5)$$

In the case of a **square lattice** (Fig. 2.3 (b)), with a reciprocal lattice vector described by $\mathbf{G}_{ij} = i\boldsymbol{b}_1 + j\boldsymbol{b}_2 = (2\pi/a_0)(j\hat{\mathbf{x}} + i\hat{\mathbf{y}})$, the Bragg plasmon

matching condition is given by

$$n_i^2 \sin^2\theta + j\frac{2\lambda}{a_0} n_i \sin\theta + (i^2 + j^2)\frac{\lambda^2}{a_0^2} - \frac{\epsilon_d \epsilon'_m}{\epsilon_d + \epsilon'_m} = 0. \tag{2.6}$$

Equations (2.5) and (2.6) are meant to be solved numerically. For a given θ, their solutions give us the discrete values of λ that satisfy the matching conditions for the excitation of a Bragg plasmon in hexagonal and square lattices, respectively.

2.2 Magneto-optics

Magneto-optics is the branch of the Physics that studies the influence of magnetic fields on the light propagation [72, 73]. In this section we show how the optical properties of a system is affected by the presence of an external magnetic field. The presence of a magnetic field results in a change of the permittivity tensor and consequently, in a change in the intensity and/or polarization of the transmitted and reflected light, known as the Faraday effect and Kerr effect, respectively.

2.2.1 Permittivity tensor in magneto-optically active materials

The response of a material to the electric field of a wave propagating inside the medium is given by the constitutive equation which relates the electric field, $\mathbf{E}$, to the displacement vector, $\mathbf{D}$:

$$\mathbf{D} = \bar{\epsilon}\epsilon_0 \mathbf{E}, \tag{2.7}$$

where ϵ_0 is the permittivity of the vacuum and $\bar{\epsilon}$ is the permittivity tensor of the material, which describes its the macroscopic properties [**?**].

In an isotropic medium, in absence of externally applied fields, the permittivity tensor is symmetric $\bar{\epsilon} = \epsilon\hat{1}$, where ϵ is the permittivity or dielectric constant of the material and $\hat{1}$ is the 3×3 unit tensor. This means that the electric field, $\mathbf{E}$, is parallel to the displacement vector, $\mathbf{D}$, and so it is to its polarization direction, $\mathbf{P}$, since $\mathbf{P} = \epsilon_0 (\bar{\epsilon} - 1)\mathbf{E}$.

However, under the presence of a magnetic field, the permittivity tensor in linear response adopts the following non-diagonal form [72]

$$\bar{\epsilon} = \begin{pmatrix} \epsilon & \epsilon_{xy} & \epsilon_{xz} \\ -\epsilon_{xy} & \epsilon & -\epsilon_{zy} \\ -\epsilon_{xz} & \epsilon_{zy} & \epsilon \end{pmatrix}, \tag{2.8}$$

which induces an optical anisotropy to the system. Therefore, **E**, **P**, and **D** are no longer parallel to each other, which implies that the response of the material is different depending on the direction of the wave propagation and so it is the phase velocity of the wave. In Eq. (2.8) ϵ and ϵ_{ij} are the optical and magneto-optical constants, respectively, where the components are, in general, complex

$$\epsilon = (n + i\kappa)^2, \tag{2.9}$$

$$\epsilon_{ij} = \epsilon'_{ij} + i\epsilon''_{ij}, \tag{2.10}$$

being n the refractive index of the material, κ the extinction coefficient and ϵ'_{ij} and ϵ''_{ij} the real and imaginary part of the complex MO constant, respectively.

In paramagnetic and diamagnetic materials the MO constants are proportional (to lowest order) to the applied magnetic field. The problem with this type of materials is that the MO constants are usually much smaller than the optical constants, unless very high magnetic fields are applied [34]. In the case of a ferromagnetic material, the off-diagonal components are proportional (also in a linear approximation) to the magnetization, **M**, induced by the magnetic field. In these materials, the permittivity tensor of Eq. (2.8) reads as follows [72]

$$\bar{\epsilon} = \begin{pmatrix} \epsilon & aM_z & aM_y \\ -aM_z & \epsilon & -aM_x \\ -aM_y & aM_x & \epsilon \end{pmatrix}, \tag{2.11}$$

where a is a constant and M_i is the magnetization in the i-th direction. The advantage of ferromagnetic materials is that one can magnetically saturate the system with relatively small magnetic fields and still have reasonable high MO constants.

2.2.2 Faraday effect

In 1845 Michael Faraday discovered that the plane of polarization of linearly polarized light rotates when light propagates through a glass in the

presence of a magnetic field, parallel to the direction of the light propagation [74]. This effect is now known as the Faraday effect, and it is observed in nonmagnets as well as ferromagnets.

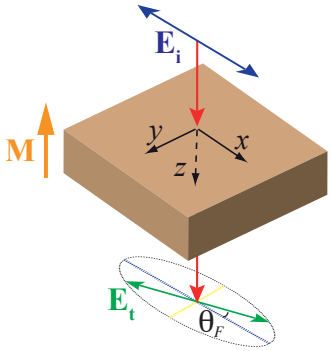

Figure 2.4: Scheme of the Faraday effect. It shows a linearly polarized light propagating through a ferromagnetic material parallel to the magnetization, **M**, where a rotation of the polarization plane of the transmitted light, θ_F, is observed, which is known as Faraday rotation.

We shall assume that we have a film of ferromagnetic material in the xy-plane with magnetization **M** along the z-axis and a linearly polarized light impinging at normal incidence so it propagates in the z direction (see Fig. 2.4). From Eq. (2.11), the permittivity tensor of our system takes the following form

$$\bar{\epsilon} = \begin{pmatrix} \epsilon & \epsilon_{xy} & 0 \\ -\epsilon_{xy} & \epsilon & 0 \\ 0 & 0 & \epsilon \end{pmatrix} = \begin{pmatrix} \epsilon & aM_z & 0 \\ -aM_z & \epsilon & 0 \\ 0 & 0 & \epsilon \end{pmatrix}. \tag{2.12}$$

It is known that linearly polarized light can be decomposed into two circularly polarized light waves: right and left. In a material with a non-symmetric permittivity tensor as the one in Eq. (2.12), right and left circularly polarized waves traveling along the z direction propagate with different velocities and also attenuate at different rates, so their relative amplitude changes. Therefore, after traveling through the ferromagnetic material, the recombination of both waves gives as a result an elliptically polarized light wave (this is shown in Fig. 2.4). The polarization of the transmitted light is rotated with respect to the one of the incident light an angle given by θ_{F}, and it is characterized by the ellipticity η_{F}, which corresponds to the ratio of the minor to the major axes of the ellipsoid. At normal incidence, if we assume that the light is polarized along the x-axis, as in Fig. 2.4, the Faraday rotation is given by $\theta_{\mathrm{F}} \approx \mathrm{Re}\{t_{yx}/t_{xx}\}$,

while the corresponding ellipticity is given by $\eta_F \approx \mathrm{Im}\{t_{yx}/t_{xx}\}$. Here, t_{ij} with $i, j = x, y$ are the complex transmission amplitudes of the structure that relate the components of the incident electric field, E_i^{inc}, with the components of the transmitted electric field, E_j^{trans}, in the following way

$$\begin{pmatrix} E_x^{\mathrm{trans}} \\ E_y^{\mathrm{trans}} \end{pmatrix} = \begin{pmatrix} t_{xx} & t_{xy} \\ t_{yx} & t_{yy} \end{pmatrix} \begin{pmatrix} E_x^{\mathrm{inc}} \\ E_y^{\mathrm{inc}} \end{pmatrix}. \tag{2.13}$$

2.2.3 Magneto-Optical Kerr effect

Three decades after Faraday's discovery, John Kerr studied the rotation of light polarization when it was reflected from a magneto-optical metal [75]. Nowadays, all the phenomena arising from the reflection of light from a magnetized medium are generally referred to as the magneto-optical Kerr effect (MOKE). Depending on the orientation of the magnetization vector relative to the sample plane and the plane of incidence of light, three types of magneto-optical effects in reflection can be distinguished: polar, longitudinal and transverse MOKE. We proceed now with the description of each of them, where we assume that xy-plane and xz-plane are the sample plane and the plane of incidence, respectively, and that the incident light is p-polarized, i.e., the electric field of the incident light is contained in the plane of incidence (see Fig. 2.5).

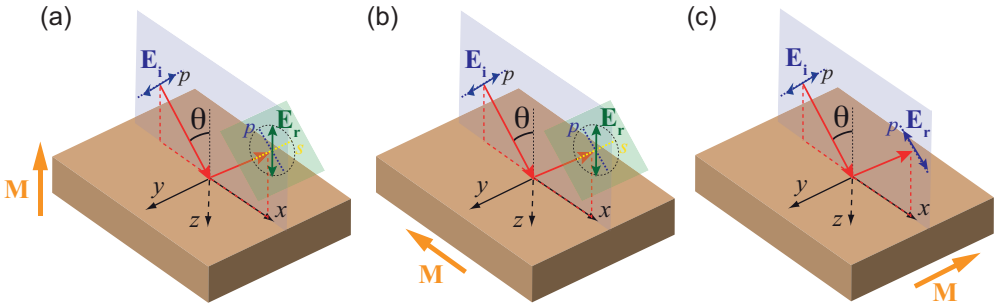

Figure 2.5: Magneto-optical Kerr effect: (a) polar configuration, (b) longitudinal configuration and (c) transversal configuration.

Polar MOKE

In polar configuration the magnetization vector, **M**, is oriented perpendicularly to the sample surface and parallel to the plane of incidence (see

Fig. 2.5(a)). This magneto-optical effect is analogous to the Faraday effect but, in this case, for reflected waves. The permittivity tensor for the ferromagnetic material in polar configuration is also given by

$$\bar{\epsilon} = \begin{pmatrix} \epsilon & \epsilon_{xy} & 0 \\ -\epsilon_{xy} & \epsilon & 0 \\ 0 & 0 & \epsilon \end{pmatrix} = \begin{pmatrix} \epsilon & aM_z & 0 \\ -aM_z & \epsilon & 0 \\ 0 & 0 & \epsilon \end{pmatrix}. \tag{2.14}$$

The result is an elliptically polarized reflected wave characterized by an ellipticity, η_{K}, and rotated with respect to the polarization of the incident light an angle, θ_{K}. θ_{K} and η_{K} are known as Kerr rotation and Kerr ellipticity, respectively, and are defined as: $\theta_{\mathrm{K}} = \mathrm{Re}\{r_{sp}/r_{pp}\}$ and $\eta_{\mathrm{K}} = \mathrm{Im}\{r_{sp}/r_{pp}\}$. In this case, r_{ij} with $i, j = s, p$ are the complex reflection amplitudes from the reflection matrix,

$$\begin{pmatrix} E_p^{\mathrm{refl}} \\ E_s^{\mathrm{refl}} \end{pmatrix} = \begin{pmatrix} r_{xx} & r_{xy} \\ r_{yx} & r_{yy} \end{pmatrix} \begin{pmatrix} E_p^{\mathrm{inc}} \\ E_s^{\mathrm{inc}} \end{pmatrix}, \tag{2.15}$$

that relates the components of the incident electric field, $\mathrm{E}_i^{\mathrm{inc}}$, with the components of the reflected electric field, $\mathrm{E}_j^{\mathrm{refl}}$. Here, s and p subscripts denote the type of polarization. The electric field of p-polarized light is contained in the plane of incidence, while the s-polarized light have the electric field perpendicular to the plane of incidence.

Considering a semi-infinite ferromagnetic material, for light impinging from a medium with a permittivity constant, ϵ_n, along the x-axis at an angle θ, Kerr rotation and ellipticity in polar configuration are given by [72]

$$\theta_{\mathrm{K}} + i\eta_{\mathrm{K}} = -\frac{\epsilon/\epsilon_n \left(\sqrt{\epsilon/\epsilon_n - \sin^2\theta} + \sin\theta\tan\theta\right)}{\epsilon(\epsilon/\epsilon_n - 1)\left(\epsilon/\epsilon_n - \tan^2\theta\right)}\epsilon_{xy}, \tag{2.16}$$

where $\theta_K + i\eta_K$ is known as the complex Kerr rotation. In Eq. (2.16) we have assumed that, for the ferromagnetic material, the MO constants are much smaller than the optical ones, $|\epsilon_{xy}| \ll |\epsilon|$, and also that $n \gg \kappa$.

For the simplest case of light at normal incidence impinging from the air, $\epsilon_n = 1$, the expressions for the polar Kerr rotation and ellipticity reduce to [73]

$$\theta_{\mathrm{K}} = -\frac{\epsilon'_{xy}}{\sqrt{\epsilon}(\epsilon - 1)} \tag{2.17}$$

$$\eta_{\mathrm{K}} = -\frac{\epsilon''_{xy}}{\sqrt{\epsilon}(1 - \epsilon)}. \tag{2.18}$$

Notice that Kerr rotation, θ_{K}, and ellipticity, η_{K}, are proportional to the real and imaginary terms of the non-diagonal component of the permittivity tensor, respectively. Moreover, it is seen from Eq. (2.14) that θ_{F} and η_{F} are proportional to the magnetization, M_z (in a linear approximation).

Longitudinal MOKE

The magnetic configuration known as longitudinal is characterized by the magnetization vector, $\mathbf{M}$, to be parallel to both the sample plane and the plane of incidence (see Fig. 2.5(b)), so the permittivity tensor for our reference system is

$$\bar{\epsilon} = \begin{pmatrix} \epsilon & 0 & 0 \\ 0 & \epsilon & -\epsilon_{zy} \\ 0 & \epsilon_{zy} & \epsilon \end{pmatrix} = \begin{pmatrix} \epsilon & 0 & 0 \\ 0 & \epsilon & -aM_x \\ 0 & aM_x & \epsilon \end{pmatrix}. \tag{2.19}$$

The MOKE in this configuration also consists in a rotation of the polarization plane of light as well as a change of intensity. Thus, given that $|\epsilon_{xy}| \ll |\epsilon|$ and $n \gg \kappa$, for a semi-infinite ferromagnetic material in longitudinal configuration, we have a characteristic Kerr rotation and ellipticity of the reflected wave given by [72]

$$\theta_{\mathrm{K}} + i\eta_{\mathrm{K}} = -\frac{\epsilon/\epsilon_n \sin^2\theta \left(\sin\theta\tan\theta - \sqrt{\epsilon/\epsilon_n - \sin^2\theta}\right)}{(\epsilon/\epsilon_n - 1)\left(\epsilon/\epsilon_n - \tan^2\theta\right)\sqrt{\epsilon/\epsilon_n - \sin^2\theta}}\epsilon_{zy}. \tag{2.20}$$

Transverse MOKE

The transverse magneto-optical Kerr effect (TMOKE) is observed when the magnetization vector, $\mathbf{M}$, is oriented perpendicularly to the plane of incidence of the light and parallel to the sample plane (see Fig. 2.5 (c)). Under this conditions the permittivity tensor adopts the following form

$$\bar{\epsilon} = \begin{pmatrix} \epsilon & 0 & \epsilon_{xz} \\ 0 & \epsilon & 0 \\ -\epsilon_{xz} & 0 & \epsilon \end{pmatrix} = \begin{pmatrix} \epsilon & 0 & aM_y \\ 0 & \epsilon & 0 \\ -aM_y & 0 & \epsilon \end{pmatrix}. \tag{2.21}$$

TMOKE is revealed in the change of intensity of the of the p-component of the linearly polarized light reflected by the ferromagnetic material. In this magnetic configuration, the s-component of the electric field is parallel to the magnetization and this implies that it does no suffer any

MO effect and, consequently, there is no rotation of the reflected light. The intensity change of the p-component of the reflected light is described by [72]

$$\text{TMOKE} = \frac{R_{pp}(+\mathbf{M}) - R_{pp}(-\mathbf{M})}{R_{pp}(+\mathbf{M}) + R_{pp}(-\mathbf{M})}, \tag{2.22}$$

where TMOKE measures the relative change in the reflectivity for p-polarized light, $R_{pp} = |r_{pp}^2|$, upon reversal of the magnetization of the ferromagnetic layer, $\mathbf{M}$. Notice that with this definition of the TMOKE, this quantity is bounded between -1 and $+1$ and it does not involve the reflection in the demagnetized state.

It can be shown that for a flat interface of ferromagnetic material-dielectric, under the same approximations as before, $|\epsilon_{xy}| \ll |\epsilon|$ and $n \gg \kappa$, the TMOKE have the following form [76]

$$\text{TMOKE} = 2\epsilon_n \sin(2\theta)\, \text{Re}\left[\frac{\epsilon_{xz}}{(\epsilon^2 - \epsilon_n^2)\cos^2\theta - \epsilon_n\epsilon + \epsilon_n^2}\right]. \tag{2.23}$$

This effect is also linear in magnetization. From Eq. (2.23) we see that the TMOKE vanishes at $\theta = 0^{\text{o}}$. This means that in transversal configuration we do not have any MO effect at normal incidence.

3 Generalized scattering-matrix approach

A powerful approach, which is widely used to describe nanostructured systems without magneto-optical activity, is the so-called scattering-matrix formalism [50–52]. In recent years, this approach was extended to study different MO effects in nanostructured multilayer structures [53] and to describe the wave propagation in periodic structures containing certain types of anisotropic media [54]. However, as it was formerly mentioned, there were still basic physical situations which lied out of the scope of those implementations of the scattering formalism. Thus, for instance, the Kerr and the Faraday effects in the transverse configuration, in which the magnetic field (or the magnetization of the sample) is parallel to the sample plane but perpendicular to the plane of incidence, could not be addressed with the existent scattering-matrix-based approaches. More generally, when the optical anisotropy of the the materials involves off-diagonal elements of the permittivity tensor along the growth direction of the multilayer structure, none of the previous implementations of the scattering-matrix approach were able to describe the wave propagation in such structures. As we will see, the technical problem lies in the fact that in such situations the propagating eigenstates in the different layers cannot be simply described with a standard eigenvalue problem. In this chapter we show our approach to solve this problem, introducing a generalization of the scattering-matrix technique to describe the magneto-optics of periodically nanostructured multilayer systems in any magnetic configuration, comprising any kind of optically anisotropic materials.

3.1 Generalized scattering-matrix formalism

Our central goal is to solve the Maxwell's equations for a patterned multilayer structure containing any combination of materials (isotropic and anisotropic). For this purpose, we shall generalize the scattering-matrix

approach developed by Whittaker and Culshaw in Ref. [50]. Following this work, we shall first discuss the Maxwell's equations to be solved. Then, we shall address the band structure of an unbounded layer to determine the propagating eigenstates in the different layers. Then, we shall discuss how to construct the fields in a multilayer structure using those eigenstates and, finally we shall describe how the scattering matrix can be used to determine the field amplitudes in the whole structure.

3.1.1 Maxwell's equations

Let us start by describing the Maxwell's equations to be solved. Assuming a harmonic time dependence $\exp(-i\omega t)$, the Maxwell's equations adopt the following form: $\nabla \cdot \epsilon_0 \bar{\epsilon} \mathbf{E} = 0$, $\nabla \cdot \mathbf{H} = 0$, $\nabla \times \mathbf{H} = -i\omega\epsilon_0 \bar{\epsilon} \mathbf{E}$, and $\nabla \times \mathbf{E} = i\omega\mu_0 \mathbf{H}$, where the permittivity is in general a tensor given by

$$\bar{\epsilon} = \begin{pmatrix} \epsilon_{xx} & \epsilon_{xy} & \epsilon_{xz} \\ \epsilon_{yx} & \epsilon_{yy} & \epsilon_{yz} \\ \epsilon_{zx} & \epsilon_{zy} & \epsilon_{zz} \end{pmatrix}. \tag{3.1}$$

Notice that we have assumed that $\bar{\mu} = \bar{1}$ since we are interested in the optical regime. Notice also that the first Maxwell's equation is automatically satisfied if the third one is fulfilled, and the second one can be satisfied by expanding the magnetic field in terms of basis functions with zero divergence. Following Ref. [50] we introduce the rescaling: $\omega\epsilon_0 \mathbf{E} \to \mathbf{E}$ and $\sqrt{\mu_0\epsilon_0}\omega = \omega/c \to \omega$. Thus, the final two equations to be solved are

$$\nabla \times \mathbf{H} = -i\bar{\epsilon}\mathbf{E}, \tag{3.2}$$

$$\nabla \times \mathbf{E} = i\omega^2 \mathbf{H}. \tag{3.3}$$

We consider here multilayer systems in which each layer can be, in principle, periodically structured. Assuming that z corresponds to the growth direction of the structure, the tensor $\bar{\epsilon}$ is independent of $z$and depends on the in-plane coordinates $\mathbf{r} \equiv (x, y)$ in a periodic fashion. Due to this periodicity, it is convenient to work in a momentum representation for the in-plane coordinates. Thus, for an in-plane wave vector $\mathbf{k}$, we can write the fields as a sum over reciprocal lattice vectors $\mathbf{G}$

$$\mathbf{H}(\mathbf{r}, z) = \sum_{\mathbf{G}} \tilde{\mathbf{H}}_{\mathbf{k}}(\mathbf{G}, z) e^{i(\mathbf{k}+\mathbf{G})\cdot\mathbf{r}}, \tag{3.4}$$

$$\mathbf{E}(\mathbf{r}, z) = \sum_{\mathbf{G}} \tilde{\mathbf{E}}_{\mathbf{k}}(\mathbf{G}, z) e^{i(\mathbf{k}+\mathbf{G})\cdot\mathbf{r}}, \tag{3.5}$$

Now, it is convenient to define the Fourier space vectors [50]

$$\boldsymbol{h}(z) \equiv \left[\tilde{\mathbf{H}}_{\mathbf{k}}(\mathbf{G}_1, z), \tilde{\mathbf{H}}_{\mathbf{k}}(\mathbf{G}_2, z), \dots\right]^T \tag{3.6}$$

$$\boldsymbol{e}(z) \equiv \left[\tilde{\mathbf{E}}_{\mathbf{k}}(\mathbf{G}_1, z), \tilde{\mathbf{E}}_{\mathbf{k}}(\mathbf{G}_2, z), \dots\right]^T. \tag{3.7}$$

Although $\tilde{\mathbf{H}}_{\mathbf{k}}$ and $\tilde{\mathbf{E}}_{\mathbf{k}}$ depend on $\mathbf{k}$, the calculation is done for a given value of $\mathbf{k}$ and therefore, we shall omit such labels in other quantities.

In what follows, we shall need the Fourier components of the permittivity tensor for the different layers

$$\tilde{\epsilon}_{ij}(\mathbf{G}) = \frac{1}{S}\int_{\text{unit cell}} d\mathbf{r}\, \epsilon_{ij}(\mathbf{r}) e^{-i\mathbf{G}\cdot\mathbf{r}}, \tag{3.8}$$

where $i, j = x, y, z$, S is the area of the in-plane unit cell, and the matrix $\hat{\epsilon}_{ij}$ is such that $(\hat{\epsilon}_{ij})_{\mathbf{G}\mathbf{G}'} = \tilde{\epsilon}_{ij}(\mathbf{G} - \mathbf{G}')$. Analogously, the components of the index tensor $\eta_{ij}(\mathbf{r}) = [\overline{\epsilon}^{-1}(\mathbf{r})]_{ij}$ have Fourier expansions $\tilde{\eta}_{ij}(\mathbf{G})$ and matrix representations $\hat{\eta}_{ij}$.

With the notation just introduced, a product such as $\epsilon_{ij}\mathbf{E}$ becomes $\hat{\epsilon}_{ij}\boldsymbol{e}$ in momentum space. Thus, Eqs. (3.2) and (3.3) can be now written as

$$i\hat{k}_y h_z(z) - h_y'(z) = -i\sum_j \hat{\epsilon}_{xj} e_j(z) \tag{3.9}$$

$$h_x'(z) - i\hat{k}_x h_z(z) = -i\sum_j \hat{\epsilon}_{yj} e_j(z) \tag{3.10}$$

$$i\hat{k}_x h_y(z) - i\hat{k}_y h_x(z) = -i\sum_j \hat{\epsilon}_{zj} e_j(z), \tag{3.11}$$

and

$$i\hat{k}_y e_z(z) - e_y'(z) = i\omega^2 h_x(z) \tag{3.12}$$

$$e_x'(z) - i\hat{k}_x e_z(z) = i\omega^2 h_y(z) \tag{3.13}$$

$$i\hat{k}_x e_y(z) - i\hat{k}_y e_x(z) = i\omega^2 h_z(z), \tag{3.14}$$

where $\hat{k}_x$ and $\hat{k}_y$ are diagonal matrices with $(\hat{k}_x)_{\mathbf{G}\mathbf{G}} = (k_x + G_x)$ and $(\hat{k}_y)_{\mathbf{G}\mathbf{G}} = (k_y + G_y)$, and the primes stand for partial derivative with respect to z.

To conclude this subsection, let us say that matrices like $\hat{\epsilon}_{ij}$ or $\hat{\eta}_{ij}$ have in practice a finite dimension equal to $N_G \times N_G$, where N_G is number of

reciprocal lattice vectors considered in the numerical calculations. It is also worth stressing that the simple Fourier factorization used above for the products like $\epsilon_{ij}E_j$, which is exact when $N_G \to \infty$, may lead in some cases to serious convergence problems when truncating the matrices $\hat{\epsilon}_{ij}$. The reason is that both the permittivity tensor and the electric field can exhibit discontinuities at the interfaces between different materials. The correct Fourier factorization of this type of products when N_G is finite is discussed in detail in sec. 3.3.

Fourier components of the permittivity tensor for periodic dot/antidot arrays

When the periodic structure under study consists of circular holes, as it is the case for this work, the Fourier expansion of the permittivity, Eq. (3.8), can be calculated analytically [77]. For holes of radius r and permittivity components ϵ_{ij}^h in a material with permittivity ϵ_{ij}^m, we have

$$\tilde{\epsilon}_{ij}(\mathbf{G}) = \begin{cases} 2(\epsilon_{ij}^h - \epsilon_{ij}^m)\beta J_1(Gr)/(Gr) & \text{if } \mathbf{G} \neq 0 \\ \epsilon_{ij}^m + \beta(\epsilon_{ij}^h - \epsilon_{ij}^m) & \text{if } \mathbf{G} = 0, \end{cases} \tag{3.15}$$

where β is the fraction of the area occupied by the holes, and J_1 is a Bessel function of first kind. In the case of a hexagonal lattice, $\beta = (2/\sqrt{3})\pi r^2/a_0^2$, while for a square lattice, $\beta = \pi r^2/a_0^2$, being a_0 is the lattice constant in both cases.

Notice that Eq. (3.15) also works for dot arrays. In that case $\epsilon_{ij}^h = \epsilon_{ij}^d$ would be the permittivity components of the disk and ϵ_{ij}^m the permittivity of the surrounding material.

3.1.2 Band structure of a single layer

Now our task is to solve the Maxwell's equations in momentum space derived in the previous subsection for the case of an unbounded layer. For this purpose, we expand the magnetic field in terms of z propagating plane waves as follows [50]

$$\begin{aligned} \mathbf{H}(\mathbf{r}, z) = \sum_{\mathbf{G}} \Bigg(& \tilde{\phi}_x(\mathbf{G}) \left[\hat{\mathbf{x}} - \frac{1}{q}(k_x + G_x)\hat{\mathbf{z}} \right] \\ & + \tilde{\phi}_y(\mathbf{G}) \left[\hat{\mathbf{y}} - \frac{1}{q}(k_y + G_y)\hat{\mathbf{z}} \right] e^{i(\mathbf{k}+\mathbf{G})\cdot\mathbf{r} + iqz}, \end{aligned} \tag{3.16}$$

where $\hat{\mathbf{x}}$, $\hat{\mathbf{y}}$, and $\hat{\mathbf{z}}$ are the Cartesian unit vectors and q is the z-component of the wave vector. Here, $\tilde{\phi}_x(\mathbf{G})$ and $\tilde{\phi}_y(\mathbf{G})$ are the expansion coefficients to be determined by substituting into Maxwell's equations. Notice that this expression satisfies $\nabla \cdot \mathbf{H} = 0$. Now, it is convenient to rewrite the previous expression in momentum representation. By defining the vectors $\phi_x = [\tilde{\phi}_x(\mathbf{G_1}), \tilde{\phi}_x(\mathbf{G_2}), \dots]^T$ and $\phi_y = [\tilde{\phi}_y(\mathbf{G_1}), \tilde{\phi}_y(\mathbf{G_2}), \dots]^T$, we can write

$$\boldsymbol{h}(z) = e^{iqz}\left\{\phi_x\hat{\mathbf{x}} + \phi_y\hat{\mathbf{y}} - \frac{1}{q}(\hat{k}_x\phi_x + \hat{k}_y\phi_y)\hat{\mathbf{z}}\right\}, \tag{3.17}$$

where $\hat{k}_x$ and $\hat{k}_y$ are the diagonal matrices previously defined. For what follows, it is convenient to rewrite this last equation in the following vector notation

$$\boldsymbol{h}(z) = e^{iqz}\left(\phi_x, \phi_y, -\frac{1}{q}(\hat{k}_x\phi_x + \hat{k}_y\phi_y)\right)^T, \tag{3.18}$$

where let us recall that every entry in this column vector is a vector of dimension N_G. With this vector notation, Eqs. (3.9-3.11) can now be written as

$$\mathcal{C}\boldsymbol{h}(z) = \hat{\hat{\epsilon}}\boldsymbol{e}(z), \tag{3.19}$$

where the block matrices $\mathcal{C}$ and $\hat{\hat{\epsilon}}$

$$\mathcal{C} = \begin{pmatrix} \hat{0} & q\hat{1} & -\hat{k}_y \\ -q\hat{1} & \hat{0} & \hat{k}_x \\ \hat{k}_y & -\hat{k}_x & \hat{0} \end{pmatrix}, \quad \hat{\hat{\epsilon}} = \begin{pmatrix} \hat{\epsilon}_{xx} & \hat{\epsilon}_{xy} & \hat{\epsilon}_{xz} \\ \hat{\epsilon}_{yx} & \hat{\epsilon}_{yy} & \hat{\epsilon}_{yz} \\ \hat{\epsilon}_{zx} & \hat{\epsilon}_{zy} & \hat{\epsilon}_{zz} \end{pmatrix}. \tag{3.20}$$

On the other hand, Eqs. (3.12-3.14) adopt now the form

$$\mathcal{C}^T\boldsymbol{e}(z) = \omega^2\boldsymbol{h}(z). \tag{3.21}$$

From Eq. (3.19) we obtain the following expression for the electric field in momentum representation

$$\boldsymbol{e}(z) = \hat{\hat{\eta}}\mathcal{C}\boldsymbol{h}(z), \tag{3.22}$$

where $\hat{\hat{\eta}} = \hat{\hat{\epsilon}}^{-1}$. Substituting this expression in Eq. (3.21) we obtain the following closed equation for the magnetic field in momentum representation

$$\mathcal{C}^T\hat{\hat{\eta}}\mathcal{C}\boldsymbol{h}(z) = \omega^2\boldsymbol{h}(z), \tag{3.23}$$

which defines an eigenvalue problem for ω^2. Indeed, only two of the three identities obtained from this equation, one for each $\hat{\mathbf{x}}$, $\hat{\mathbf{y}}$, and $\hat{\mathbf{z}}$, are independent. From the first two identities, and using Eq. (3.18), we obtain the following equations determining the allowed values for q

$$\left(\mathcal{A}_2 q^2 + \mathcal{A}_1 q + \mathcal{A}_0 + \mathcal{A}_{-1}\frac{1}{q}\right)\phi = 0, \tag{3.24}$$

where $\phi = (\phi_x, \phi_y)^T$ and the 2×2 block matrices $\mathcal{A}_n$ are defined by

$$\begin{aligned}
\mathcal{A}_2 &= \begin{pmatrix} \hat{\eta}_{yy} & -\hat{\eta}_{yx} \\ -\hat{\eta}_{xy} & \hat{\eta}_{xx} \end{pmatrix}, \\
A_1 &= \mathcal{A}_1^{(a)} + \mathcal{A}_1^{(b)} \\
&= \begin{pmatrix} -\hat{k}_y\hat{\eta}_{zy} & \hat{k}_y\hat{\eta}_{zx} \\ \hat{k}_x\hat{\eta}_{zy} & -\hat{k}_x\hat{\eta}_{zx} \end{pmatrix} + \begin{pmatrix} -\hat{\eta}_{yz}\hat{k}_y & \hat{\eta}_{yz}\hat{k}_x \\ \hat{\eta}_{xz}\hat{k}_y & -\hat{\eta}_{xz}\hat{k}_x \end{pmatrix}, \\
\mathcal{A}_0 &= -\omega^2\hat{\mathbf{1}} + \mathcal{A}_0^{(a)} + \mathcal{A}_0^{(b)} \\
&= -\omega^2\begin{pmatrix} 1 & 0 \\ 0 & 1 \end{pmatrix} + \begin{pmatrix} \hat{k}_y\hat{\eta}_{zz}\hat{k}_y & -\hat{k}_y\eta_{zz}\hat{k}_x \\ -\hat{k}_x\hat{\eta}_{zz}\hat{k}_y & \hat{k}_x\eta_{zz}\hat{k}_x \end{pmatrix} \\
&\quad + \begin{pmatrix} \eta_{yy}\hat{k}_x\hat{k}_x - \eta_{yx}\hat{k}_y\hat{k}_x & \hat{\eta}_{yy}\hat{k}_x\hat{k}_y - \hat{\eta}_{yx}\hat{k}_y\hat{k}_y \\ \hat{\eta}_{xx}\hat{k}_y\hat{k}_x - \hat{\eta}_{xy}\hat{k}_x\hat{k}_x & \hat{\eta}_{xx}\hat{k}_y\hat{k}_y - \hat{\eta}_{xy}\hat{k}_x\hat{k}_y \end{pmatrix}, \\
\mathcal{A}_{-1} &= \begin{pmatrix} \hat{k}_y\hat{\eta}_{zx}\hat{k}_y\hat{k}_x - \hat{k}_y\hat{\eta}_{zy}\hat{k}_x\hat{k}_x & \hat{k}_y\hat{\eta}_{zx}\hat{k}_y\hat{k}_y - \hat{k}_y\hat{\eta}_{zy}\hat{k}_x\hat{k}_y \\ \hat{k}_x\hat{\eta}_{zy}\hat{k}_x\hat{k}_x - \hat{k}_x\hat{\eta}_{zx}\hat{k}_y\hat{k}_x & \hat{k}_x\hat{\eta}_{zy}\hat{k}_x\hat{k}_y - \hat{k}_x\hat{\eta}_{zx}\hat{k}_y\hat{k}_y \end{pmatrix}.
\end{aligned} \tag{3.25}$$

Solving the nonlinear eigenvalue problem

In general, Eq. (3.24) is a so-called rational eigenvalue problem. This problem belongs to the category of nonlinear eigenvalue problems, which continues to be a challenge in the field of numerical analysis. However, we have found that a simple linearization strategy allows us to solve exactly such an eigenvalue problem in all the examples that we have studied. It is worth stressing that so far the scattering approach has only been applied to situations where the materials are isotropic [50] or in cases in which the MO activity is such that the off-diagonal components of the permittivity tensor involving the z component are zero [53] ($\epsilon_{xz} = \epsilon_{yz} = 0$). In those cases, Eq. (3.24) reduces to

$$\mathcal{A}_0\phi = -\mathcal{A}_2 q^2 \phi, \tag{3.26}$$

which is a generalized eigenvalue problem for q^2, which can be solved with standard techniques of linear algebra. Notice that, as explained in the

introduction of this chapter, those cases exclude the analysis of the Kerr effect in the transversal and longitudinal configurations.

The solution of Eq. (3.24) provides $4N_G$ non-vanishing complex eigenvalues for q. Half of these eigenvalues lie in the upper half of the complex plane and half of them in the lower half. We detail here a simple strategy to solve numerically the nonlinear eigenvalue problem, which we have found to work without any problem in all the cases that we have considered. The first step is to multiply both sides of Eq. (3.24) by q to convert it into the following cubic eigenvalue problem

$$\left(\mathcal{B}_3 q^3 + \mathcal{B}_2 q^2 + \mathcal{B}_1 q + \mathcal{B}_0\right) \phi = 0, \tag{3.27}$$

where we have defined $\mathcal{B}_n = \mathcal{A}_{n-1}$. Now, the simplest strategy to solve exactly this cubic problem is to use a standard linearization procedure [78]. The idea goes as follows. We first define the following vectors

$$\lambda_n = q^{n-1}\phi; \quad n = 1, 2, 3. \tag{3.28}$$

From this definition, and using Eq. (3.27), it is easy to show that the vectors λ_n satisfy the following equation

$$\begin{pmatrix} 0 & 1 & 0 \\ 0 & 0 & 1 \\ \mathcal{B}_0 & \mathcal{B}_1 & \mathcal{B}_2 \end{pmatrix} \begin{pmatrix} \lambda_1 \\ \lambda_2 \\ \lambda_3 \end{pmatrix} = q \begin{pmatrix} 1 & 0 & 0 \\ 0 & 1 & 0 \\ 0 & 0 & -\mathcal{B}_3 \end{pmatrix} \begin{pmatrix} \lambda_1 \\ \lambda_2 \\ \lambda_3 \end{pmatrix}. \tag{3.29}$$

We have thus converted the problem into a generalized linear eigenvalue problem that can be solved with standard linear algebra techniques. The obvious disadvantage of this simple procedure is that one increases the dimension of the problem by a factor of 3. In this sense, it may be advantageous in some cases to implement other methods like, for instance, the iterative Newton method. In any case, and as illustrated in sec. 3.3, we have not found any problem to converge the calculations using the linearization procedure, which provides the exact solution of the nonlinear eigenvalue problem.

3.1.3 Electric and magnetic field

The next step toward the complete solution of the Maxwell's equations in a multilayer structure is the determination of the fields in the different layers. This can be done by expressing the fields as a combination of forward and backward propagating waves with wave numbers q_n, and

complex amplitudes a_n and b_n, respectively. These amplitudes will be later on determined by using the boundary conditions at the interfaces and surfaces of the multilayer structure. Since the boundary conditions are simply the continuity of the in-plane field components, we focus here on the analysis of the field components e_x, e_y, h_x, and h_y. From Eq. (3.18), the in-plane components of $\boldsymbol{h}$ can be expanded in terms of propagating waves as follows

$$\begin{pmatrix} h_x(z) \\ h_y(z) \end{pmatrix} = \sum_n \left\{ \begin{pmatrix} \phi_{x_n} \\ \phi_{y_n} \end{pmatrix} e^{iq_n z} a_n + \begin{pmatrix} \varphi_{x_n} \\ \varphi_{y_n} \end{pmatrix} e^{-ip_n(d-z)} b_n \right\}, \tag{3.30}$$

where d is the thickness of the layer. Here, a_n is the coefficient of the forward going wave at the $z = 0$ interface, and b_n is the backward going wave at $z = d$. On the other hand, q_n correspond to the eigenvalues of Eq. (3.24) with $\mathrm{Im}\{q_n\} > 0$ and p_n are the eigenvalues with $\mathrm{Im}\{p_n\} < 0$. Notice also that, contrary to the case of isotropic materials, here the eigenfunctions of the forward and backward propagating waves are different in general. This is a signature of the fact that the existence of non-vanishing off-diagonal components of the permittivity tensor involving the z-coordinate can break the time-reversal symmetry in the system.

To make the notation more compact, we now define two $2N_G \times 2N_G$ matrices Φ_+ and Φ_- whose columns are the vectors ϕ_n and φ_n, respectively. Moreover, we define the diagonal $2N_G \times 2N_G$ matrices $\hat{\mathrm{f}}_+(z)$ and $\hat{\mathrm{f}}_-(d-z)$, such that $[\hat{\mathrm{f}}_+(z)]_{nn} = e^{iq_n z}$ and $[\hat{\mathrm{f}}_-(d-z)]_{nn} = e^{-ip_n(d-z)}$, and the $2N_G$-dimensional vectors $h_{||}(z) = [h_x(z), h_y(z)]^T$, $a = (a_1, a_2, \dots)^T$, and $b = (b_1, b_2, \dots)^T$. In terms of these quantities, the in-plane magnetic-field components become

$$h_{||}(z) = \Phi_+ \hat{\mathrm{f}}_+(z) a + \Phi_- \hat{\mathrm{f}}_-(d-z) b. \tag{3.31}$$

Similarly, using the momentum representation of $\mathbf{E}$ from Eq. (3.22) it is straightforward to show that the in-plane components of the electric field, $e_{||}(z) = [-e_y(z), e_x(z)]^T$, are given by

$$e_{||}(z) = \left(\mathcal{A}_0^{(b)} \Phi_+ \hat{q}^{-1} + \mathcal{A}_1^{(b)} \Phi_+ + \mathcal{A}_2 \Phi_+ \hat{q}\right) \hat{\mathrm{f}}_+(z) a + \left(\mathcal{A}_0^{(b)} \Phi_- \hat{p}^{-1} + \mathcal{A}_1^{(b)} \Phi_- + \mathcal{A}_2 \Phi_- \hat{p}\right) \hat{\mathrm{f}}_-(d-z) b, \tag{3.32}$$

where the $\mathcal{A}$'s are defined in Eq. (3.25) and we have defined the $2N_G \times 2N_G$ diagonal matrices $\hat{q}$ and $\hat{p}$ such that $\hat{q}_{nn} = q_n$ and $\hat{p}_{nn} = p_n$.

We can now combine Eq. (3.31) and (3.32) into a single expression as follows

$$\begin{aligned}\begin{pmatrix} e_{||}(z) \\ h_{||}(z) \end{pmatrix} &= M \begin{pmatrix} \hat{\mathrm{f}}_+(z)a \\ \hat{\mathrm{f}}_-(d-z)b \end{pmatrix} \\ &= \begin{pmatrix} M_{11} & M_{12} \\ M_{21} & M_{22} \end{pmatrix} \begin{pmatrix} \hat{\mathrm{f}}_+(z)a \\ \hat{\mathrm{f}}_-(d-z)b \end{pmatrix}, \end{aligned} \tag{3.33}$$

where the $2N_G \times 2N_G$ matrices M_{ij} are defined as

$$\begin{aligned} M_{11} &= \mathcal{A}_0^{(b)}\Phi_+\hat{q}^{-1} + \mathcal{A}_1^{(b)}\Phi_+ + \mathcal{A}_2\Phi_+\hat{q}, \\ M_{12} &= \mathcal{A}_0^{(b)}\Phi_-\hat{p}^{-1} + \mathcal{A}_1^{(b)}\Phi_- + \mathcal{A}_2\Phi_-\hat{p}, \\ M_{21} &= \Phi_+, \quad M_{22} = \Phi_-. \end{aligned} \tag{3.34}$$

3.1.4 The scattering matrix

The final step in our calculation is to use the scattering matrix (S-matrix) to compute the field amplitudes needed to describe the different relevant physical quantities. It should be noted that this part of the calculation is practically independent of the type of materials present in the structure (isotropic or anisotropic).

By definition, the S-matrix relates the vectors of the amplitudes of forward and backward going waves, a_l and b_l, where l now denotes the layer, in the different layers of the structure as follows

$$\begin{pmatrix} a_l \\ b_{l'} \end{pmatrix} = S(l', l) \begin{pmatrix} a_{l'} \\ b_l \end{pmatrix} = \begin{pmatrix} S_{11} & S_{12} \\ S_{21} & S_{22} \end{pmatrix} \begin{pmatrix} a_{l'} \\ b_l \end{pmatrix}. \tag{3.35}$$

The field amplitudes in two consecutive layers are related via the boundary conditions for the fields, namely the continuity of the in-plane components of the fields in every interface and surface. If we consider the interface between the layer l and the layer $l+1$, the corresponding boundary conditions read

$$\begin{pmatrix} e_{||}(d_l) \\ h_{||}(d_l) \end{pmatrix}_l = \begin{pmatrix} e_{||}(0) \\ h_{||}(0) \end{pmatrix}_{l+1}, \tag{3.36}$$

where d_l is the thickness of layer l. From this condition, together with Eq. (3.33), it is easy to show that the amplitudes in layers l and $l+1$

are related by the interface matrix $I(l, l+1) = M_l^{-1} M_{l+1}$ in the following way

$$\begin{aligned}\begin{pmatrix} \hat{f}_l^+ a_l \\ b_l \end{pmatrix} &= I(l, l+1) \begin{pmatrix} a_{l+1} \\ \hat{f}_{l+1}^- b_{l+1} \end{pmatrix} \\ &= \begin{pmatrix} I_{11} & I_{12} \\ I_{21} & I_{22} \end{pmatrix} \begin{pmatrix} a_{l+1} \\ \hat{f}_{l+1}^- b_{l+1} \end{pmatrix}, \end{aligned} \tag{3.37}$$

where $\hat{f}_l^+ = \hat{\mathrm{f}}_{l,+}(d_l)$ and $\hat{f}_{l+1}^- = \hat{\mathrm{f}}_{l+1,-}(d_{l+1})$.

Now, with the help of the interface matrices, the S-matrix can be calculated in an iterative way as follows. The matrix $S(l', l+1)$ can be calculated from $S(l', l)$ using the definition of $S(l', l)$ in Eq. (3.35) and the interface matrix $I(l, l+1)$. Eliminating a_l and b_l we obtain the relation between $a_{l'}$, $b_{l'}$ and a_{l+1}, b_{l+1}, from which $S(l', l+1)$ can be constructed. This reasoning leads to the following iterative relations

$$\begin{aligned} S_{11}(l', l+1) &= \left[I_{11} - \hat{f}_l^+ S_{12}(l', l) I_{21} \right]^{-1} \hat{f}_l^+ S_{11}(l', l) \\ S_{12}(l', l+1) &= \left[I_{11} - \hat{f}_l^+ S_{12}(l', l) I_{21} \right]^{-1} \\ &\qquad \times \left(\hat{f}_l^+ S_{12}(l', l) I_{22} - I_{12} \right) \hat{f}_{l+1}^- \\ S_{21}(l', l+1) &= S_{22}(l', l) I_{21} S_{11}(l', l+1) + S_{21}(l', l) \\ S_{22}(l', l+1) &= S_{22}(l', l) I_{21} S_{12}(l', l+1) + \\ &\qquad S_{22}(l', l) I_{22} \hat{f}_{l+1}^-. \end{aligned} \tag{3.38}$$

Starting from $S(l', l') = 1$, one can apply the previous recursive relations to a layer at a time to build up $S(l', l)$.

From the knowledge of the S-matrix one can compute all the field amplitudes needed to describe a physical situation. Thus for instance, labeling the surface $l = 0$ and the substrate $l = N$, the calculation of the reflectivity and the transmission coefficients requires the knowledge of the amplitudes b_0 and a_N, which can be calculated from $S(0, N)$. On the other hand, it may be interesting to calculate the fields inside the structure, for which we need the amplitudes a_l and b_l. These can be obtained by calculating $S(0, l)$ and $S(l, N)$, and using Eq. (3.35) to get [50]

$$\begin{aligned} a_l &= \left[1 - S_{12}(0, l) S_{21}(l, N) \right]^{-1} \\ &\quad \times \left[S_{11}(0, l) a_0 + S_{12}(0, l) S_{22}(l, N) b_N \right] \\ b_l &= \left[1 - S_{21}(l, N) S_{12}(0, l) \right]^{-1} \\ &\quad \times \left[S_{21}(l, N) S_{11}(0, l) a_0 + S_{22}(l, N) b_N \right]. \end{aligned}$$

From these amplitudes, together with Eq. (3.33), one can determine the fields everywhere in the system, which usually provides an important physical insight into the different MO effects [36].

3.2 Spatially uniform slabs

A multilayer structure may contain some uniform (non-structured) layers. In particular, this is always the case for the medium of incidence and for the substrate layer. In this sense, it is interesting to discuss how the formalism discussed in section sec. 3.1 is simplified in the case of uniform slabs. In this case, the permittivity tensor is diagonal in momentum space: $(\hat{\epsilon}_{ij})_{\mathbf{G},\mathbf{G}'} = \tilde{\epsilon}_{ij}(0)\delta_{\mathbf{G},\mathbf{G}'}$, although it can remain fully anisotropic in real space. This implies that all the matrices in momentum representation are also diagonal. The eigenvalue problem of Eq. (3.24) leads to the following quartic secular equation for $q(\mathbf{G})$. Focusing on $\mathbf{G} = 0$, this equation reads

$$\sum_{n=0}^{4} D_n q^n = 0, \tag{3.39}$$

where the coefficients are given by

$$\begin{aligned}
D_4 &= \eta_{xx}\eta_{yy} - \eta_{xy}\eta_{yx}, \\
D_3 &= k_x\left[\eta_{xy}\eta_{yz} + \eta_{yx}\eta_{zy} - \eta_{yy}(\eta_{xz} + \eta_{zx})\right] \\
&\quad + k_y\left[\eta_{yx}\eta_{xz} + \eta_{xy}\eta_{zx} - \eta_{xx}(\eta_{yz} + \eta_{zy})\right], \\
D_2 &= k_x^2\left[\eta_{yy}(\eta_{xx} + \eta_{zz}) - \eta_{xy}\eta_{yx} - \eta_{yz}\eta_{zy}\right] \\
&\quad + k_y^2\left[\eta_{xx}(\eta_{yy} + \eta_{zz}) - \eta_{xy}\eta_{yx} - \eta_{xz}\eta_{zx}\right] \\
&\quad + k_x k_y\left[\eta_{xz}(\eta_{yz} + \eta_{zy}) + \eta_{yz}(\eta_{zx} - \eta_{xz})\right. \\
&\quad \left. - \eta_{zz}(\eta_{xy} + \eta_{yx})\right] - \omega^2(\eta_{xx} + \eta_{yy}), \\
D_1 &= k_x^3\left[\eta_{xy}\eta_{yz} + \eta_{yx}\eta_{zy} - \eta_{yy}(\eta_{xz} + \eta_{zx})\right] \\
&\quad + k_y^3\left[\eta_{yx}\eta_{xz} + \eta_{xy}\eta_{zx} - \eta_{xx}(\eta_{yz} + \eta_{zy})\right] \\
&\quad + k_x^2 k_y\left[\eta_{xy}\eta_{zx} + \eta_{xz}\eta_{yx} - \eta_{xx}(\eta_{yz} + \eta_{zy})\right] \\
&\quad + k_y^2 k_x\left[\eta_{yx}\eta_{zy} + \eta_{yz}\eta_{xy} - \eta_{yy}(\eta_{xz} + \eta_{zx})\right] \\
&\quad + \omega^2\left[k_x^2(\eta_{xz} + \eta_{zx}) + k_y^2(\eta_{yz} + \eta_{zy})\right],
\end{aligned}$$

$$
\begin{aligned}
D_0 \;=\; & k_x^4(\eta_{yy}\eta_{zz}-\eta_{yz}\eta_{zy})+k_y^4(\eta_{xx}\eta_{zz}-\eta_{xz}\eta_{zx}) \\
& +k_x^3k_y\left[\eta_{xz}\eta_{zy}+\eta_{yz}\eta_{zx}-\eta_{zz}(\eta_{xy}+\eta_{yx})\right] \\
& +k_y^3k_x\left[\eta_{yz}\eta_{zx}+\eta_{xz}\eta_{zy}-\eta_{zz}(\eta_{yx}+\eta_{xy})\right] \\
& +k_x^2k_y^2\left[\eta_{zz}(\eta_{xx}+\eta_{yy})+\eta_{xy}\eta_{yx}-\eta_{xz}\eta_{zx}-\eta_{yz}\eta_{zy}\right] \\
& +\omega^2\left[\omega^2-k_x^2(\eta_{yy}+\eta_{zz})-k_y^2(\eta_{xx}+\eta_{zz})\right. \\
& \qquad \left.+k_xk_y(\eta_{xy}+\eta_{yx})\right]. \qquad (3.40)
\end{aligned}
$$

For $\mathbf{G}\neq 0$, one just needs to replace $k_{x,y}$ by $k_{x,y}+G_{x,y}$. Eq. (3.39) has been previously derived (in terms of the components of the permittivity tensor) in the context of the analysis of uniform multilayer structures containing MO and anisotropic materials [79]. This equation simplifies in several limiting cases. Thus for instance, if we consider the typical configuration for measuring the TMOKE, then the permittivity tensor is given by Eq. (2.21). In this case, $D_3=D_1=0$ and setting $k_y=0$ the solutions of Eq. (3.39) are $q_1^2=\omega^2/\eta_{yy}-k_x^2$ and $q_2^2=\omega^2/\eta_{xx}-k_x^2$. Moreover, in this case the layer matrix defined in Eq. (3.33) adopts the following simple form (for $\mathbf{G}=0$)

$$
M=\begin{pmatrix}
\omega^2/q_1 & 0 & -\omega^2/q_1 & 0 \\
0 & \eta_{xx}q_2-\eta_{xz}k_x & 0 & -\eta_{xx}q_2-\eta_{xz}k_x \\
1 & 0 & 1 & 0 \\
0 & 1 & 0 & 1
\end{pmatrix}. \qquad (3.41)
$$

On the other hand, for an isotropic layer $\bar{\epsilon}=\epsilon\hat{1}$, and in this case $D_3=D_1=0$ and $q^2=\epsilon\omega^2-(k_x^2+k_y^2)$. The corresponding layer matrix reads now (for $\mathbf{G}=0$)

$$
M=\begin{pmatrix} M_{11} & -M_{11} \\ \hat{1} & \hat{1} \end{pmatrix}, \qquad (3.42)
$$

where $\hat{1}$ is the 2×2 unit matrix and

$$
M_{11}=\frac{1}{q}\begin{pmatrix} \omega^2-k_y^2\eta & \eta k_xk_y \\ \eta k_xk_y & \omega^2-k_x^2\eta \end{pmatrix}. \qquad (3.43)
$$

3.3 Fast Fourier factorization

The scattering approach, as formulated in sec. 3.1, is known to have important convergence problems when metals are involved, more notably when the infrared range is investigated. These problems are well-known in the theory of gratings [80] and it has been understood that they originate from the incorrect factorization of the product of two periodic discontinuous functions. Such a product appears, in particular, in the constitutive relation $\mathbf{D} = \bar{\epsilon}\mathbf{E}$, where $\mathbf{D}$ is the displacement vector. When calculating the Fourier components of $\mathbf{D}$ in sec. 3.1.1, we have used the so-called Laurent's rule. This rule states that the Fourier components h_n of the product $h(x)$ of two arbitrary functions $f(x)$ and $g(x)$ are given by

$$h_n = \sum_{m=-\infty}^{\infty} f_{n-m} g_m. \tag{3.44}$$

Although this result is correct, as long as the sum extends to infinity, it is not always correct when one truncates the series, as we do numerically. This was recognized by Li [81], who established the following rules for factorization:

1. Let $h(x) = f(x)g(x)$ and either $f(x)$ or $g(x)$ be continuous at some $x = x_0$. The other quantity may be discontinuous there. Then, Laurent's rule applies, *i.e.*

   $$[h] = [[f]]\,[g]\,. \tag{3.45}$$

   Here, $[g]$ denotes a column vector constructed with, let us say, N_G Fourier components g_n and by $[[f]]$ we denote the $N_G \times N_G$ Toeplitz matrix whose (n, m) entry is f_{n-m}.

2. Let $h(x) = f(x)g(x)$ and both $f(x)$ and $g(x)$ be discontinuous at some $x = x_0$, but the product $f(x)g(x)$ be continuous there. Then, the so-called inverse rule holds, which is given by

   $$[h] = \left[\left[\frac{1}{f}\right]\right]^{-1} [g]\,. \tag{3.46}$$

3. Let $h(x) = f(x)g(x)$ and both $f(x)$ and $g(x)$ be discontinuous at some $x = x_0$ and the product $f(x)g(x)$ be discontinuous there as well. Then, the product of the two functions in Fourier space cannot be formed by either the Laurent's rule or the inverse rule.

Obviously, in our analysis of the Maxwell's equations in sec. 3.1.1, see Eqs. (3.9-3.11), we are violating these factorization rules. We are simply using the Laurent's rule, although in the interface between different materials we may have concurrent discontinuities in both the permittivity tensor and the electric field, and in some cases the product (the displacement vector) is discontinuous as well. Thus, our goal now is to reformulate the Maxwell equations in momentum space in order to respect the factorization rules stated above. For this purpose, we make use of the so-called *fast Fourier factorization* put forward by Popov and Nevière in Ref. [82].

For the sake of concreteness, let us consider a two-dimensional periodic system consisting of an array of circular holes or circular pillars. Now, let us define a vector with the continuous components of the $\mathbf{E}$ and $\mathbf{D}$ fields, *i.e.* $\mathbf{G} = [E_t, D_n, E_z]^T$. Here, E_t is the tangential component of the electric field in the xy plane, D_n is the normal component of the displacement vector in the xy plane, and E_z is the z component of the electric field. These three components are continuous in the xy plane when we cross the boundary of a hole (or pillar) and the permittivity tensor undergoes a discontinuity. Now, let us establish the relation between these field components and the three Cartesian components of the electric field $\mathbf{G} = \hat{F}\mathbf{E}$, where $\mathbf{E} = [E_x, E_y, E_z]^T$. There are many possible choices for $\hat{F}$. We choose to express its matrix elements in terms of the polar angle $\phi(x, y)$ defined as $re^{i\phi(x,y)} = x + iy$. It is straightforward to show that

$$\hat{F} = \begin{pmatrix} -s & c & 0 \\ \epsilon_{xx}c + \epsilon_{yx}s & \epsilon_{xy}c + \epsilon_{yy}s & \epsilon_{xz}c + \epsilon_{yz}s \\ 0 & 0 & 1 \end{pmatrix}, \tag{3.47}$$

where c and s are abbreviations for $\cos\phi$ and $\sin\phi$, respectively.

We now define the inverse of this matrix $\hat{C} = \hat{F}^{-1}$. Thus, $\mathbf{E} = \hat{C}\mathbf{G}$. Let us recall the constitutive relation $\mathbf{D} = \bar{\epsilon}\mathbf{E}$, where $\bar{\epsilon}$ is given by Eq. (3.1). This relation can be now written as

$$\mathbf{D} = \bar{\epsilon}\hat{C} \cdot \mathbf{G} = \bar{\epsilon}\hat{C} \cdot \hat{F}\mathbf{E}, \tag{3.48}$$

whose elements are now expressed as the product of a discontinuous function and a continuous one. Thus, using Laurent's rule for the first term of the product and the inverse rule for the second one, the Fourier components of the displacement vector can be calculated as

$$[\mathbf{D}] = [[\bar{\epsilon}\hat{C}]]\,[[\hat{C}]]^{-1}[\mathbf{E}]. \tag{3.49}$$

This indicates that the Toeplitz matrix of the index tensor $\hat{\eta}$ in the formalism of sec. 3.1 has to be calculated as follows

$$[[\hat{\hat{\eta}}]] = [[\hat{C}]][[\bar{\epsilon}\hat{C}]]^{-1}. \tag{3.50}$$

This is indeed the only change that we need to introduce in the formalism to improve significantly the convergence in the problematic cases. Notice that in practice this requires the calculation of the Toeplitz matrix of several trigonometric functions, which in general has to be done numerically.

For the sake of completeness, we now provide simplified expressions for $[[\hat{\hat{\eta}}]]$ in some cases of special interest for us.

Isotropic material

In the case of an isotropic material, for which $\bar{\epsilon} = \epsilon\hat{1}$, it is straightforward to show that Eq. (3.50) reduces to [83, 84]

$$\left[\left[\hat{\hat{\eta}}\right]\right] = \begin{pmatrix} [[\epsilon]]^{-1} + [[X]]\,[[c^2]] & [[X]]\,[[cs]] & 0 \\ [[X]]\,[[cs]] & [[1/\epsilon]] - [[X]]\,[[c^2]] & 0 \\ 0 & 0 & [[\epsilon]]^{-1} \end{pmatrix}, \tag{3.51}$$

where $[[X]] = [[1/\epsilon]] - [[\epsilon]]^{-1}$. This requires, in particular, the calculation of the Fourier components of the trigonometric functions $\cos^2\phi$ and $\cos\phi\sin\phi$, which can be easily done numerically. Notice that these components are independent of the wavelength of the light and therefore, they can be calculated once and forever for a given structure.

Polar configuration

In polar configuration, as we showed in chapter 2, the magnetization is perpendicular to the sample. Thus, following the considerations of sec. 2.2, we consider a permittivity tensor given by

$$\bar{\epsilon} = \begin{pmatrix} \epsilon & \epsilon_{xy} & 0 \\ -\epsilon_{xy} & \epsilon & 0 \\ 0 & 0 & \epsilon \end{pmatrix}. \tag{3.52}$$

In this case the expression of Eq. (3.50) reduces to

$$\left[\left[\hat{\hat{\eta}}\right]\right] = \begin{pmatrix} [[\hat{\eta}_{11}]] & [[\hat{\eta}_{12}]] & [[0]] \\ [[\hat{\eta}_{21}]] & [[\hat{\eta}_{22}]] & [[0]] \\ [[0]] & [[0]] & [[\hat{\eta}_{33}]] \end{pmatrix}, \tag{3.53}$$

where the Toeplitz matrix elements are,

$$\begin{aligned}
[[\hat{\eta}_{11}]] &= \left[\left[\frac{\varepsilon^2+\varepsilon_{xy}^2}{\varepsilon}\right]\right]^{-1} + [[X]]\left[\left[c^2\right]\right] - [[Y]]\,[[sc]] \\
[[\hat{\eta}_{12}]] &= -\left[\left[\frac{\varepsilon^2+\varepsilon_{xy}^2}{\varepsilon}\right]\right]^{-1}\left[\left[\frac{\varepsilon_{xy}}{\varepsilon}\right]\right] + [[X]]\left[\left[c^2\right]\right] + [[Y]]\,[[sc]] \\
[[\hat{\eta}_{21}]] &= \left[\left[\frac{\varepsilon_{xy}}{\varepsilon}\right]\right]\left[\left[\frac{\varepsilon^2+\varepsilon_{xy}^2}{\varepsilon}\right]\right]^{-1} + [[Y]]\left[\left[c^2\right]\right] + [[X]]\,[[sc]] \\
[[\hat{\eta}_{22}]] &= [[X]] + \left[\left[\frac{\varepsilon^2+\varepsilon_{xy}^2}{\varepsilon}\right]\right]^{-1} - [[X]]\left[\left[c^2\right]\right] + [[Y]]\,[[sc]] \\
[[\hat{\eta}_{33}]] &= [[\varepsilon]]^{-1}
\end{aligned} \tag{3.54}$$

where,

$$\begin{aligned}
[[X]] &= \left[\left[\frac{1}{\varepsilon}\right]\right] - \left[\left[\frac{\epsilon^2+\epsilon_{xy}^2}{\epsilon}\right]\right]^{-1} - \left[\left[\frac{\varepsilon_{xy}}{\varepsilon}\right]\right]\left[\left[\frac{\epsilon^2+\epsilon_{xy}^2}{\epsilon}\right]\right]^{-1}\left[\left[\frac{\varepsilon_{xy}}{\varepsilon}\right]\right] \\
[[Y]] &= \left[\left[\frac{\epsilon^2+\epsilon_{xy}^2}{\epsilon}\right]\right]^{-1}\left[\left[\frac{\varepsilon_{xy}}{\varepsilon}\right]\right] - \left[\left[\frac{\varepsilon_{xy}}{\varepsilon}\right]\right]\left[\left[\frac{\epsilon^2+\epsilon_{xy}^2}{\epsilon}\right]\right]^{-1}
\end{aligned} \tag{3.55}$$

Again, one just needs the evaluation of the Fourier components of both $\cos^2\phi$ and $\cos\phi\sin\phi$.

It is worth stressing that in the choice of the normal vectors entering in the Fourier factorization there is a freedom that one can use to further improve the convergence of the calculations. For a discussion of this issue, see Ref. [84].

Transverse configuration

Let us now show the Toeplitz matrix $\left[\left[\hat{\hat{\eta}}\right]\right]^{-1}$ in the case of transverse configuration, i.e., when the applied magnetic field is perpendicular to

the plane of incidence and parallel to the sample surface so the dielectric tensor takes the following form

$$\bar{\epsilon} = \begin{pmatrix} \epsilon & 0 & \epsilon_{xz} \\ 0 & \epsilon & 0 \\ -\epsilon_{xz} & 0 & \epsilon \end{pmatrix}. \tag{3.56}$$

In this case, the Fourier components of the index tensor $[[\bar{\epsilon}\hat{C}]]\,[[\hat{C}]]^{-1}$ are given by

$$\left[\left[\hat{\hat{\eta}}\right]\right]^{-1} = \begin{pmatrix} \left[\left[\hat{\eta}_{11}^{-1}\right]\right] & \left[\left[\hat{\eta}_{12}^{-1}\right]\right] & \left[\left[\hat{\eta}_{13}^{-1}\right]\right] \\ \left[\left[\hat{\eta}_{21}^{-1}\right]\right] & \left[\left[\hat{\eta}_{22}^{-1}\right]\right] & \left[\left[\hat{\eta}_{23}^{-1}\right]\right] \\ \left[\left[\hat{\eta}_{31}^{-1}\right]\right] & \left[\left[\hat{\eta}_{32}^{-1}\right]\right] & \left[\left[\hat{\eta}_{33}^{-1}\right]\right] \end{pmatrix}, \tag{3.57}$$

here, the terms $\left[\left[\hat{\eta}_{ij}^{-1}\right]\right]$ denote the Toeplitz matrices that comprise the inverse of $\left[\left[\hat{\hat{\eta}}\right]\right]$:

$$\begin{aligned}
\left[\left[\hat{\eta}_{11}^{-1}\right]\right] &= [[\epsilon]] + [[X]]\left[\left[c^2\right]\right], \\
\left[\left[\hat{\eta}_{12}^{-1}\right]\right] &= [[X]]\,[[cs]], \\
\left[\left[\hat{\eta}_{13}^{-1}\right]\right] &= [[\epsilon_{xz}]] + [[Y]]\left[\left[c^2\right]\right], \\
\left[\left[\hat{\eta}_{21}^{-1}\right]\right] &= [[X]]\,[[cs]], \\
\left[\left[\hat{\eta}_{22}^{-1}\right]\right] &= [[1/\epsilon]]^{-1} - [[X]]\left[\left[c^2\right]\right], \\
\left[\left[\hat{\eta}_{23}^{-1}\right]\right] &= [[Y]]\,[[cs]], \\
\left[\left[\hat{\eta}_{31}^{-1}\right]\right] &= -[[\epsilon_{xz}]] - [[Y']]\left[\left[c^2\right]\right], \\
\left[\left[\hat{\eta}_{32}^{-1}\right]\right] &= -[[Y']]\,[[cs]], \\
\left[\left[\hat{\eta}_{33}^{-1}\right]\right] &= [[\epsilon]] + [[Z]]\left[\left[c^2\right]\right],
\end{aligned} \tag{3.58}$$

where

$$\begin{aligned}
[[X]] &= [[1/\epsilon]]^{-1} - [[\epsilon]], \\
[[Y]] &= [[1/\epsilon]]^{-1}[[\epsilon_{xz}/\epsilon]] - [[\epsilon_{xz}]], \qquad (3.59) \\
[[Y']] &= [[\epsilon_{xz}/\epsilon]]\,[[1/\epsilon]]^{-1} - [[\epsilon_{xz}]], \\
[[Z]] &= [[\epsilon_{xz}^2/\epsilon]] - [[\epsilon_{xz}/\epsilon]]\,[[1/\epsilon]]^{-1}[[\epsilon_{xz}/\epsilon]]. \qquad (3.60)
\end{aligned}$$

Longitudinal configuration

As we showed in sec. 2.2, in longitudinal configuration the magnetization is parallel to both, the sample and the plane of incidence, and the

dielectric tensor is given by

$$\bar{\epsilon} = \begin{pmatrix} \epsilon & 0 & 0 \\ 0 & \epsilon & \epsilon_{yz} \\ 0 & -\epsilon_{yz} & \epsilon \end{pmatrix}. \tag{3.61}$$

After straightforward algebra we arrive at the following expression

$$\left[\left[\hat{\hat{\eta}}\right]\right]^{-1} = \begin{pmatrix} \left[\left[\hat{\eta}_{11}^{-1}\right]\right] & \left[\left[\hat{\eta}_{12}^{-1}\right]\right] & \left[\left[\hat{\eta}_{13}^{-1}\right]\right] \\ \left[\left[\hat{\eta}_{21}^{-1}\right]\right] & \left[\left[\hat{\eta}_{22}^{-1}\right]\right] & \left[\left[\hat{\eta}_{23}^{-1}\right]\right] \\ \left[\left[\hat{\eta}_{31}^{-1}\right]\right] & \left[\left[\hat{\eta}_{32}^{-1}\right]\right] & \left[\left[\hat{\eta}_{33}^{-1}\right]\right] \end{pmatrix}, \tag{3.62}$$

where the terms $\left[\left[\hat{\eta}_{ij}^{-1}\right]\right]$ again denote the Toeplitz matrices that comprise the inverse of $\left[\left[\hat{\hat{\eta}}\right]\right]$:

$$\begin{aligned}
\left[\left[\hat{\eta}_{11}^{-1}\right]\right] &= [[\epsilon]] + [[X]]\left[\left[c^2\right]\right], \\
\left[\left[\hat{\eta}_{12}^{-1}\right]\right] &= [[X]]\,[[cs]], \\
\left[\left[\hat{\eta}_{13}^{-1}\right]\right] &= [[Y]]\,[[cs]], \\
\left[\left[\hat{\eta}_{21}^{-1}\right]\right] &= [[X]]\,[[cs]], \\
\left[\left[\hat{\eta}_{22}^{-1}\right]\right] &= [[1/\epsilon]]^{-1} - [[X]]\left[\left[c^2\right]\right], \\
\left[\left[\hat{\eta}_{23}^{-1}\right]\right] &= [[1/\epsilon]]^{-1}\,[[\epsilon_{yz}/\epsilon]] - [[Y]]\left[\left[c^2\right]\right], \\
\left[\left[\hat{\eta}_{31}^{-1}\right]\right] &= -\,[[Y']]\,[[cs]], \\
\left[\left[\hat{\eta}_{32}^{-1}\right]\right] &= -\,[[\epsilon_{yz}/\epsilon]]\,[[1/\epsilon]]^{-1} + [[Y']]\left[\left[c^2\right]\right], \\
\left[\left[\hat{\eta}_{33}^{-1}\right]\right] &= [[\epsilon]] + [[Z]]\left[\left[c^2\right]\right],
\end{aligned} \tag{3.63}$$

where

$$\begin{aligned}
[[X]] &= [[1/\epsilon]]^{-1} - [[\epsilon]], \\
[[Y]] &= [[1/\epsilon]]^{-1}[[\epsilon_{yz}/\epsilon]] - [[\epsilon_{yz}]], \qquad (3.64) \\
[[Y']] &= [[\epsilon_{yz}/\epsilon]]\,[[1/\epsilon]]^{-1} - [[\epsilon_{yz}]], \\
[[Z]] &= [[\epsilon_{yz}^2/\epsilon]] - [[\epsilon_{yz}/\epsilon]]\,[[1/\epsilon]]^{-1}[[\epsilon_{yz}/\epsilon]]. \qquad (3.65)
\end{aligned}$$

3.3.1 Convergence

We now want to illustrate the convergence of the results using the fast Fourier factorization just described. In Fig. 3.1 we show an example of the convergence for our first study presented in chapter 4, an iron nanohole

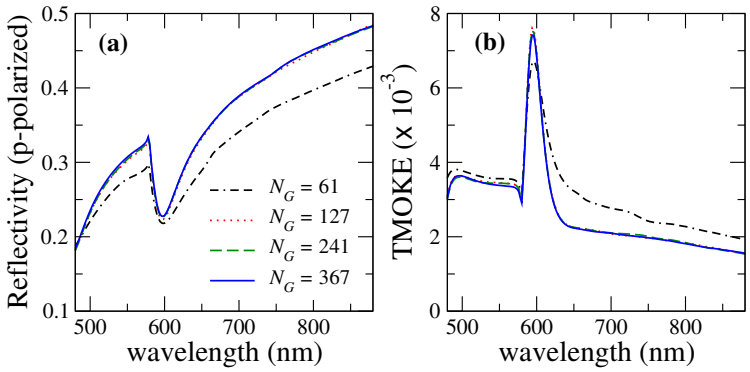

Figure 3.1: Reflectivity in the absence of magnetic field (a) and TMOKE (b) for the multilayer structure studied in sec. 4.1 for $\theta = 25^{\circ}$ and $\varphi = 0^{\circ}$ as a function of the wavelength of the incident light. The different curves correspond to results obtained with different number of reciprocal lattice vectors N_G.

array (see Fig. 4.2) where the reflectivity and the TMOKE were analyzed. In this figure, the different curves correspond to different values of N_G, which is the number of reciprocal lattice vectors taken into account in the calculations upon setting a high-momentum cutoff. As one can see, it is possible to converge the calculations to a high precision in the whole range of wavelengths. Moreover, the convergence is fast and uniform. It is important to emphasize that in order to get results of similar quality for this example without the use of the fast Fourier factorization, values of N_G even larger than 1000 are required (not shown here).

3.4 Conclusions

In this chapter, we have presented a generalization of the scattering-matrix approach to describe the propagation of electromagnetic waves in periodically patterned multilayer structures containing materials with any kind of optical activity and anisotropy. Additionally, we have also introduced the fast Fourier factorization, which assures a faster convergence of the results.

As we will see in subsequent chapters, this generalized formalism has allowed us to tackle important physical problems that have been traditionally out of the scope of this approach as the theoretical study of the transversal MO Kerr effect. In the rest of the thesis, apart from some particular cases, we will use this method to address the optical and MO response of the systems under analysis.

4 Ferromagnetic nanohole arrays

Periodic nanohole arrays of ferromagnetic metals such as Fe, Ni or Co are very interesting candidates to study as they offer a strong magneto-optical activity under relatively low magnetic fields while still support the excitation of surface plasmon polaritons. Moreover, it has been shown that the excitation of SPPs in such structures enhances the electromagnetic field intensity inside the ferromagnet and, consequently, the MO response of the system [60–63].

In view of the relevance that ferromagnetic nanohole arrays may represent, we devote this chapter to the analysis of the MO effects in such structures and their interplay with SPPs. With this purpose, we address and theoretically analyze three different experiments performed in ferromagnetic films perforated with hexagonal arrays of subwavelength holes in which the transverse and polar MO Kerr effects were measured. These experiments were performed by our collaborators at Uppsala University in Sweden and at Helmholtz-Zentrum Berlin, Freie Universität Berlin and Technische Universität Kaiserslautern in Germany. The samples were prepared using self-assembly nanosphere lithography (see Fig. 4.1). The experimental results of sec. 4.1 are reported in Ref. [62], whereas the experiments performed in Ni nanohole arrays of sec. 4.2 and sec. 4.3 are published, together with the theoretical calculations, in Ref. [85] and Ref. [86], respectively.

In the first two studies, we investigate the effect that the excitation of surface plasmon polaritons has over the transverse and polar MO Kerr effects by analyzing two experiments performed in ferromagnetic nanohole arrays of iron (sec. 4.1) and nickel (sec. 4.2). We show that ferromagnetic periodic nanohole arrays support the excitation of SPPs at either interface, incident medium or substrate, and demonstrate that the surface plasmon resonances are the origin of the enhancement observed in the MO response of these systems.

In sec. 4.3, the optical and MO properties of another nickel film perforated

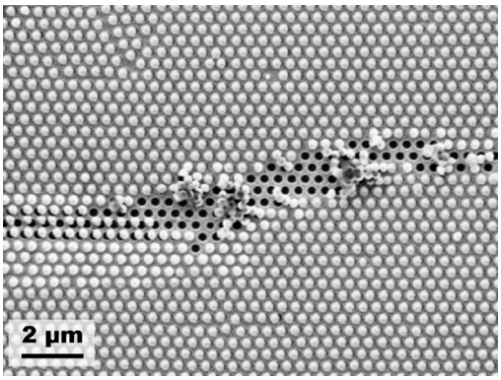

Figure 4.1: Scanning electron microscopy image of the sample surface after evaporation of Ni. The image depicts the stage of the lift off of self-assembled polystyrene beads, which leaves behind the antidot patterned film of Ni describe in sec. 4.2.

with periodic arrays of nanoholes with larger lattice parameter are studied by analyzing the dependence of the polar MO Kerr effect with the hole size of the nanostructures.

4.1 Enhanced TMOKE in iron nanohole arrays

In this section we shall analyze the experiment reported in Ref. [62] in which the transverse MO Kerr effect was studied in a periodically perforated Fe film. Let us recall that in the transversal configuration the magnetization is parallel to the ferromagnetic film and perpendicular to the plane of incidence and that this effect is described by the TMOKE signal,

$$\text{TMOKE} = \frac{R_{pp}(+\mathbf{M}) - R_{pp}(-\mathbf{M})}{R_{pp}(+\mathbf{M}) + R_{pp}(-\mathbf{M})}, \tag{4.1}$$

which is the intensity change of the p-component of the reflected light upon reversal of the magnetization of the ferromagnetic layer (see sec. 2.2 for further details).

Let us first detail the structure under study, which is described schematically in Fig. 4.2. It consists of a Fe film (100 nm thick), which is perforated with a periodic array of subwavelength circular holes (diameter of 297 nm) forming a hexagonal lattice with a lattice parameter of 470 nm.

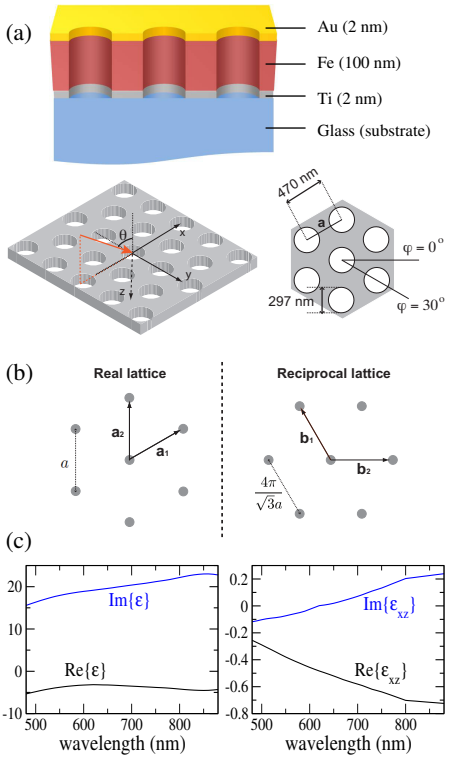

Figure 4.2: (a) Schematic representation of the system under study where we show a cut of the layered structure and a top view of the periodic array of circular holes forming a hexagonal lattice. Here, one can also see the angle definitions and the geometrical parameters of the hole array. (b) The hexagonal lattice both in real and in reciprocal space, and definition of the basis vectors. (c) The real and imaginary part of the elements ϵ (left panel) and ϵ_{xz} (right panel) of the Fe permittivity tensor used in our calculations, see Eq. (2.21), as a function of the wavelength.

The Fe film was prepared on a Si substrate and the structure contains additionally a seed layer of Ti (2 nm thick) and a capping layer of Au (2 nm thick), which were included to form a smooth Fe film and to prevent a subsequent oxidation of the surface, respectively. In our calculations we used the energy dependent permittivities taken from ellipsometric measurements of 20 nm-thick continuous films, and the off-diagonal elements of the ferromagnetic material have been extracted from Polar Kerr measurements (both rotation and ellipticity) as described in Ref. [87]. For illustrative purposes, we show in Fig. 4.2(c) the values of ϵ and ϵ_{xz} for Fe used in our calculations as a function of the wavelength. Remember that ϵ and ϵ_{xz} correspond to the optical and MO elements of the permittivity tensor described in Eq. (2.21). Notice that the magnitude of ϵ_{xz} is much smaller than the magnitude of ϵ, which explains the "smallness" of the

different MO effects.

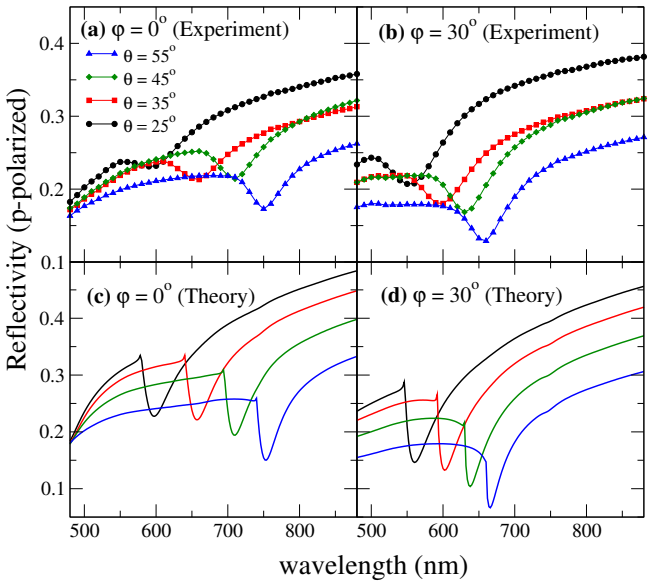

Figure 4.3: Experimental and theoretical results for the reflectivity of the demagnetized structure along the p-channel, R_{pp}, as a function of the wavelength of the incident light. As indicated in the panels, the results are shown for two different high symmetry crystallographic directions $\varphi = 0^{\text{o}}$ and $\varphi = 30^{\text{o}}$ and for various angles of incidence θ.

Let us start our discussion of the results by describing the reflectivity in this multilayer system when the Fe film is demagnetized. In the upper panels of Fig. 4.3 we reproduce the experimental results for p-polarized light obtained for two different high symmetry crystallographic directions $\varphi = 0^{\text{o}}$ and $\varphi = 30^{\text{o}}$ and for various angles of incidence θ (see Fig. 4.2(a) for a definition of these angles). The most prominent feature is the appearance of a dip which is red shifted as the angle of incidence θ is increased. Notice that the red shift depends on the crystallographic direction, and it is more pronounced for $\varphi = 0^{\text{o}}$. Such a feature is absent in the case of s-polarized light (not shown here) and it can be attributed to the excitation of surface plasmon polaritons (SPPs), as we shall discuss below. In the lower panel of Fig. 4.3, we show the corresponding theoretical results calculated with the scattering approach assuming that the MO element of the permittivity tensor, ϵ_{xz}, is zero. As one can see, our calculations nicely reproduce the experimental trends. The theoretical dips appear to be more pronounced than in the experiment, which we attribute to the unavoidable inhomogeneities in the periodic array of holes in the Fe film.

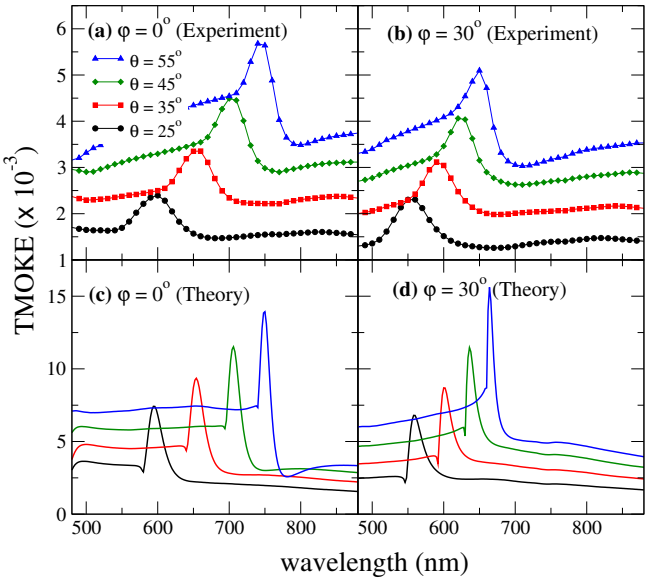

Figure 4.4: Experimental and theoretical results for the TMOKE as a function of wavelength for $\varphi = 0^{\circ}$ and $\varphi = 30^{\circ}$ and for various angles of incidence θ.

The corresponding results (both experimental and theoretical) for the TMOKE, as defined in Eq. (4.1), are displayed in Fig. 4.4. Notice that the theoretical results, in good agreement with the experiment, show that the TMOKE can be resonantly enhanced at wavelengths that follow closely those in which the dips in the reflectivity appear. Notice that at resonance the TMOKE signal increases by roughly a factor of 2 with respect to value at off-resonant wavelengths. It is worth stressing that, as illustrated in Fig. 4.5, the signal for the continuous Fe film (no perforated) is featureless in the spectral range considered here.

In order to understand the origin of the peaks in the TMOKE and the corresponding dips in the reflectivity, we have investigated these quantities in a more systematic way. In Fig. 4.6 we present the results for these two quantities as a function of the wavelength and of the angle of incidence θ. In this figure we can observe again the appearance of the dips in the reflectivity, which are accompanied by pronounced peaks in the TMOKE. The shape of the TMOKE and the dispersion of the peaks with θ suggest that these features originate from the excitation of the SPPs of this structure. To confirm this impression we have to calculate the matching condition for the excitation of these surface modes given by Eq. (2.4). For this purpose, we have ignored the thin Au layer, which is practically transparent, and calculated the mode for an iron/air interface.

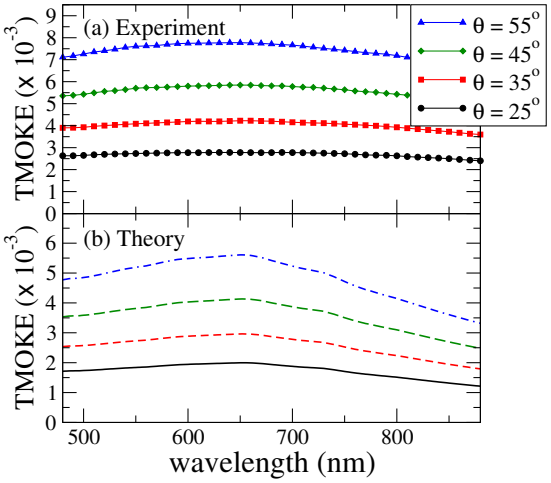

Figure 4.5: (a) Experimental results for the TMOKE for the non-perforated multilayer structure (formed by uniform slabs) as a function of wavelength for various angles of incidence θ taken from Ref. [62]. (b) The corresponding theoretical results.

In this case the reciprocal lattice vector, $\mathbf{G}_{n_1 n_2}$, with our choice for the reciprocal lattice basis vectors (see Fig. Fig. 4.2(b)) is given by

$$\begin{aligned}\mathbf{G}_{i,j} = (2\pi/a_0\sqrt{3})\{&[(2j-i)\cos\varphi + i\sqrt{3}\sin\varphi]\hat{\mathbf{x}} \\ &+ [i\sqrt{3}\cos\varphi + (i-2j)\sin\varphi]\hat{\mathbf{y}}\},\end{aligned} \tag{4.2}$$

which takes into consideration the rotation of the sample an angle φ. The condition of Eq. (2.4) tells us at which (discrete) wavelengths the SPPs can be excited for a given angle of incidence. We have solved Eq. (2.4) numerically and found that for $\varphi = 0^{\text{o}}$ the only mode that can be excited in the wavelength range analyzed here is $\lambda_{0,-1}$, while for $\varphi = 30^{\text{o}}$ we have two possibilities: $\lambda_{0,-1}$ and $\lambda_{-1,-1}$, which indeed correspond to the same wavelength. In Fig. 4.6 we have included as dashed lines the relation between the resonant wavelength and the angle of incidence θ for these two cases. As one can see, these relations nicely describe the positions of both the dips in the reflectivity and the peaks in the TMOKE. This strongly suggests that the resonant enhancement of the TMOKE is due to the excitation of SPPs in our layered structure.

Summing up, we have theoretically analyzed the TMOKE in a Fe film with a periodic array of subwavelength holes. We have shown, in excellent agreement with the experiment, that the TMOKE signal can be

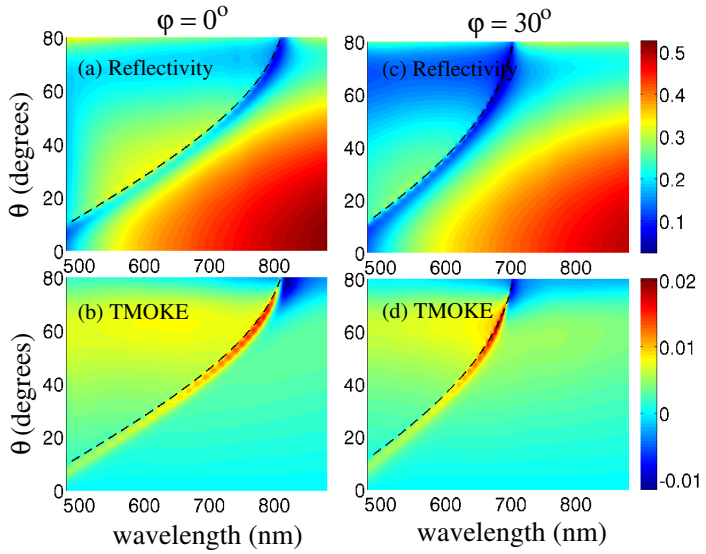

Figure 4.6: Theoretical results for the reflectivity and TMOKE as a function of the wavelength and angle of incidence θ for $\varphi = 0^{\circ}$ and $\varphi = 30^{\circ}$. The dashed lines in the different panels correspond to the resonant condition for the excitation of SPPs, as described by Eq. (2.4).

resonantly enhanced when the samples are illuminated with an appropriate wavelength, and we have attributed this phenomenon to the excitation of surface plasmon polaritons.

4.2 Study of the MO effects of transparent nickel nanohole arrays

Let us now discuss the influence of the SPPs on the MO response of another pure ferromagnetic metal, such as Ni, again patterned with a hexagonal array of subwavelength holes, in this case in both polar and transversal configurations. Ni is an interesting candidate in this context as it forms a thin and self-passivating oxide layer (approximately 1nm) [88,89]. Furthermore, it is known that the MO activity of Ni-based nanopatterns is enhanced by the presence of SPPs [63,90–93].

The sample studied consisted on a 30 nm thick Ni film deposited on sapphire substrate [85]. Ni layer was pierced with holes of a diameter of 300 nm in a hexagonal lattice of periodicity of 450 nm. The calculations have been made using the optical and MO elements of the dielectric tensor

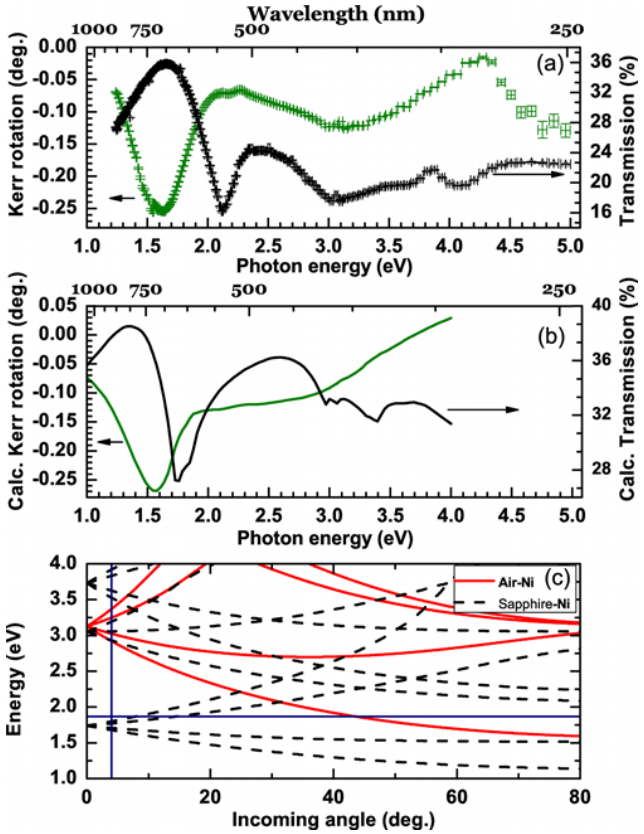

Figure 4.7: (a) Experimental transmission and polar Kerr rotation spectra for the Ni nanohole array. Kerr values were obtained with the film at the saturated state (applied magnetic field of 1.7 T). (b) Calculated Transmission and Polar Kerr rotation spectra. (c) Calculated dispersion relation of the Bragg plasmons both for the Ni-air interface and Ni-sapphire interface. The vertical line is drawn at 4° and the horizontal line at 660 nm.

given in Ref. [94], extended with those of Ref. [95] to include energies below 1.5 eV.

4.2.1 Polar MOKE

Let us start with the analysis of the polar MOKE when the magnetization is oriented perpendicularly to the sample surface (see sec. 2.2.3 for a complete description of the polar MOKE) with an angle of incidence of 4°. Fig. 4.7 shows the experimental (a) and the calculated (b) transmission and polar Kerr rotation spectra for the sample. Both the experimental and calculated transmission curves (right axis) exhibit several maxima.

As we have shown previously, if SPP modes are involved, then the energies at which the maxima appear must be close to the energies corresponding to the so-called Bragg plasmons. For that reason, we have calculated the dispersion relation of the Bragg plasmons with Eq. (2.5), see Fig. 4.7(c), finding a fair match for the transmission maxima. As we move to higher frequencies the absorption plays more and more a significant role and that implies a widening of the resonance peaks. In addition as we can see from Fig. 4.7(c), at higher frequencies, modes from the upper and lower interface begin to mix resulting in an overlapping of different resonances.

The overlap of the overall transmission maxima and the enhancement of the Kerr rotation (left axis), further prove the existence of SPPs in the sample [60, 61, 63]. The first peak in transmission records an intensity of $\sim 36\%$. Although it is expected the plasmon losses in Ni to be large, we have a clear indication of a strong SPP resonance. The propagation length of SPPs in Ni at 1.6 eV is calculated to be 840 nm and decreases strongly with increasing energy, resulting in lower transmission resonances for larger energies as shown in Fig. 4.7(a) and (b).

4.2.2 Transverse MOKE

In Fig. 4.8 we present experimental (a) and calculated (b) angular reflectivity (black, left axis) and TMOKE (red, right axis) for p-polarized light, where we see that simulated and experimental results are in very good agreement. Curves in Fig. 4.8 were measured and calculated at a wavelength of 660 nm, which corresponds to the region in between the first transmission maximum and the transmission minimum of the Fig. 4.7(a), a region with a large variation of transmission curve. The data were obtained having the hexagonal pattern aligned with one of its major symmetry axes ($\varphi = 0^{\text{o}}$) parallel to the scattering plane.

Angular resolved reflectivity measurements are also a way to explore the effect of SPPs in nanohole arrays [63]. The minima of the reflectivity at 42° observed in Fig. 4.8 (black, left axis) is a signature of surface plasmons excitation. This minimum in reflectivity is close to the theoretical value for the Bragg plasmon at that specific frequency (~ 1.85 eV), as shown by the horizontal line in Fig. 4.7(c). The width of the reflection minimum is broader than those for noble metals due to the higher absorption losses of Ni. There is an additional broadening due to the ratio of the hole depth (30 nm) to the hole diameter (300 nm). If the ratio is close to unity the features are sharper than for lower ratios [56].

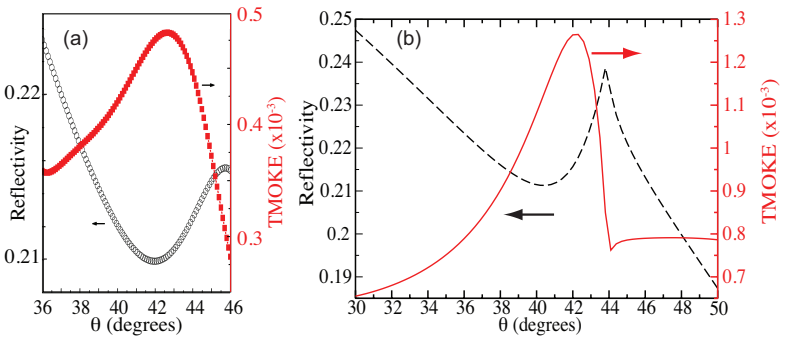

Figure 4.8: (a) Reflectivity (black dot-line, left axis) and the TMOKE (red square-line, right axis) measurements. The size of the applied magnetic field was 20 mT, enough for the magnetic saturation of the sample. (b) Calculated reflectivity (black line, left axis) and the TMOKE (red line, right axis) in the angular range of the the minimum ($\varphi = 0^{o}$).

At the same time, the TMOKE signal (red, right axis) in Fig. 4.8 shows an enhancement compared to the featureless TMOKE response of a continuous Ni film. The enhancement can be attributed to the proximity of the used wavelength (660 nm) to the plasmonic resonances at the metal/air interface (see Fig. 4.7(c)). Thus, TMOKE remains featureless when away from the excitation region.

In Fig. 4.9 we show the evolution of the reflectivity minimum and the TMOKE maximum as a function of the in-plane angle. As one can see, the position of these two features follows nicely the dispersion relation of the relevant Bragg plasmon, which is shown as a dashed line in both panels. This clearly shows that the plasmon excitation is responsible for these two features. Furthermore, Fig. 4.9 shows that outside the excitation region the reflectivity and TMOKE signals are featureless and the system behaves as a uniform medium made of a mixture of Ni and air.

In summary, in this section we have shown that a Ni thin film perforated with a hexagonal nanohole array supports the excitation of SPPs at both the air/Ni interface and Ni/substrate interface. We have observed a significant enhancement of the polar rotation and TMOKE curves for certain wavelengths and angles of incidence that we have related to the excitation of SPPs.

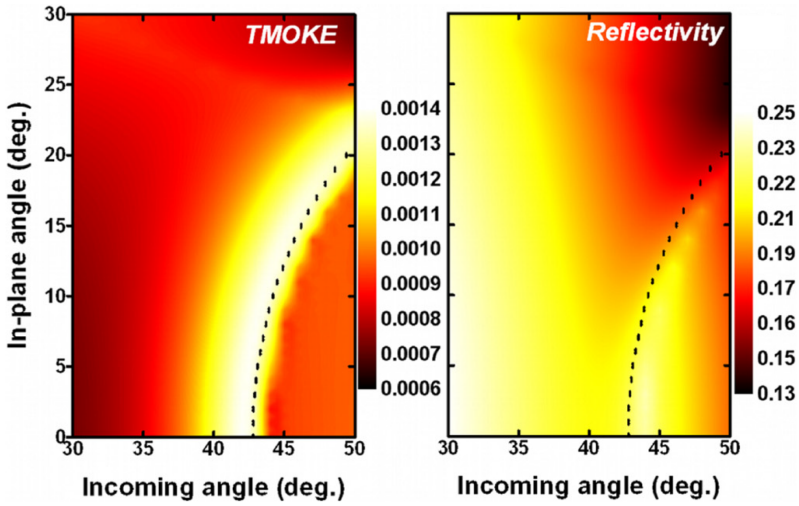

Figure 4.9: Calculated reflectivity (right panel) and TMOKE (left panel) in the same angular range as in (a) along different in-plane directions, going from $\varphi = 0^{o}$ to $\varphi = 30^{o}$.

4.3 Hole-size effects on the MO response in thin nickel nanohole arrays

Here, we present a study of the effect that the hole size has on the physics of these periodic ferromagnetic systems. The aim is to correlate the MO response to the hole size and explain the origin of the tuning effect of the Kerr rotation. The system under study consists on 50 nm height nanostructured Ni films on Si substrates [86]. The lattice parameter of the hexagonal array of holes was kept constant to 920 nm while the diameter ranged from 869 nm to 636 nm.

Fig. 4.10(b) shows the measured relative-reflectivity (upper pannels) and Kerr rotation (lower pannels) spectra of the Ni thin films perforated by arrays of nanoholes at an angle of incidence of 3^{o}. In Fig. 4.10(c), the calculated spectra for the reflectivity and the polar Kerr rotation of the corresponding Ni nanohole arrays films are presented assuming normal incidence. The simulations are in fair qualitative agreement with the experimental results. In the relative-reflectivity spectra, we can see a structure originating from the Si substrate at 3.4 eV which is most prominent in the discontinuous samples forming island (diameters of 869 and 819 nm). Apart from the Si feature, minima are observed at around 2.7 eV (A,C) and 3.3 eV (B,D).

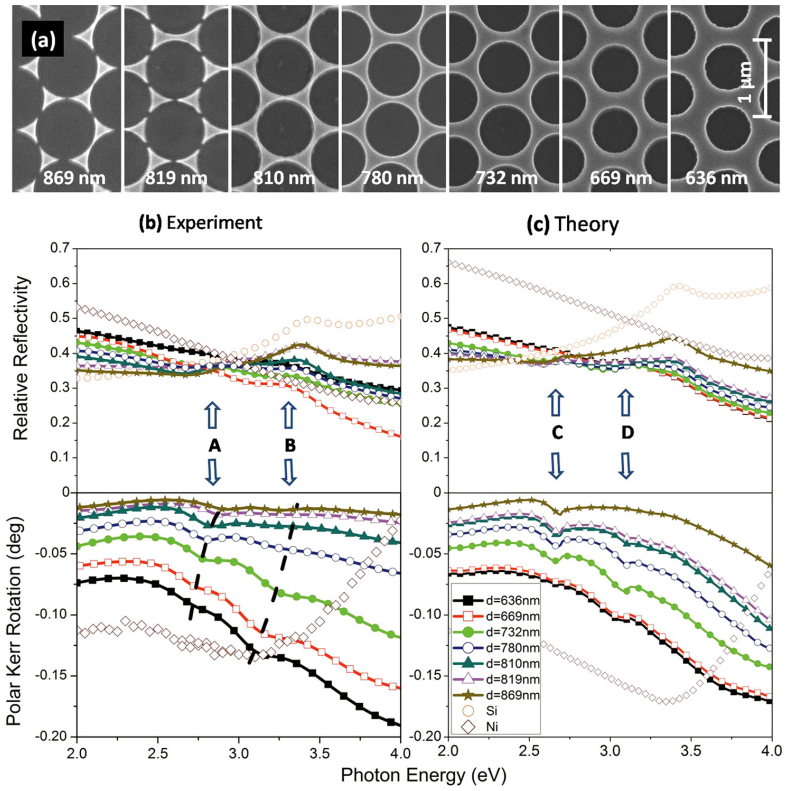

Figure 4.10: (a) Scanning electron micrographs of a series of 50nm thick Ni samples. The lattice parameter of the hexagonal array is 920nm, and the hole diameter varies from 869 down to 636 nm. (b) Measured and (c) simulated relative reflectivity (top) and polar-Kerr rotation (bottom) for the series of Ni nanohole arrays samples. For comparison, the data of a continuous Ni film and Si substrate are included as well. The reflectivity is normalized to the reflectivity of an Al mirror. The position of the observed peaks is labeled (A) and (C) and (B) and (D) in the reflectivity and marked by dashed lines as a guide to the eye in the polar Kerr rotation.

In the magneto-optic Kerr spectra, the overall (negative) polar Kerr rotation increases with decreasing hole diameter. Since the inter-hole spacing or lattice constant is kept constant at 920 nm, this increase must be directly related to the change in hole size. By decreasing the hole diameter, the surface area of the MO active material is increased yielding a larger polar Kerr rotation. Focusing now on the spectral features, we see that the MO response of the holey films is completely different from that of a continuous Ni film. We find two distinct maxima of the absolute value of the (negative) polar Kerr rotation at approximately the same photon energy as the structures in the reflectivity spectra, i.e., around 2.7 eV (A,C) and 3.3 eV (B,D). Since the spectrum of a continuous Ni film is

smooth, the structures must be related to the hole array. In addition, a red shift of the two peaks, i.e., a shift to lower photon energies with decreasing hole diameter, is clearly observed in the MOKE spectra. In the relative-reflectivity spectra, the shift can also be seen but it is less prominent. The dependence of the MO response on the hole size is clearly reproduced in the calculations. The dependence is most prominent in the structure at lower photon energy. The calculation evidences in addition a small kink close to the position of the plasmon excitation related to the Wood anomaly [96]. Because of its purely geometric origin in the periodicity of the lattice, the kink appears at the same photon energy for all samples and does not shift with decreasing hole diameter. However, the kink is not resolved in the experimental data. For the kink to be observed, a large degree of perfection of the hole lattice is needed within the area of illumination. Small variations of the lattice parameter within the spot size of ~ 5 mm^2 would wash it out.

The above-mentioned minima in the reflectivity and maxima for the absolute value of the polar Kerr rotation are the result of a resonant coupling of light to surface-plasmon excitations at the interface of the Ni films. As has been already mentioned, to obtain a resonant excitation, one needs frequency and momentum matching between incoming light and surface plasmon. Using Eq. (2.5), one can easily check that the observed spectral position of the minima in the reflectivity data and of the maxima of the absolute value of the (negative) Kerr rotation are closely related to the energy corresponding to the second and the third order of the surface plasmon excitations at the air/nickel interface. However, since in our case all samples are hexagonal lattices with the same lattice constant fixed to 920 nm, no spectral shift is expected from Eq. (2.5).

To explain the experimentally observed red shift with hole diameter, we introduced in the calculations of the SPP dispersion relation given by Eq. (2.2) an effective medium approximation. Instead of using for ϵ_m, the dielectric constant of a continuous film of Ni, an effective dielectric constant proportional to the amount of Ni (membrane) and air (holes) has been applied in the following way:

$$\epsilon_m = f \cdot \epsilon_{Ni} + (1 - f) \cdot \epsilon_{air}, \tag{4.3}$$

where f is the area fraction of Ni at the surface. As a consequence, it will depend on the radius of each sample. To compare with experiment, the photon energy of the first peak is plotted in Fig. 4.11(a) as a function of hole size as derived from experiment (solid squares) and from calculation at normal incidence (open circles). Note the different scaling. The two

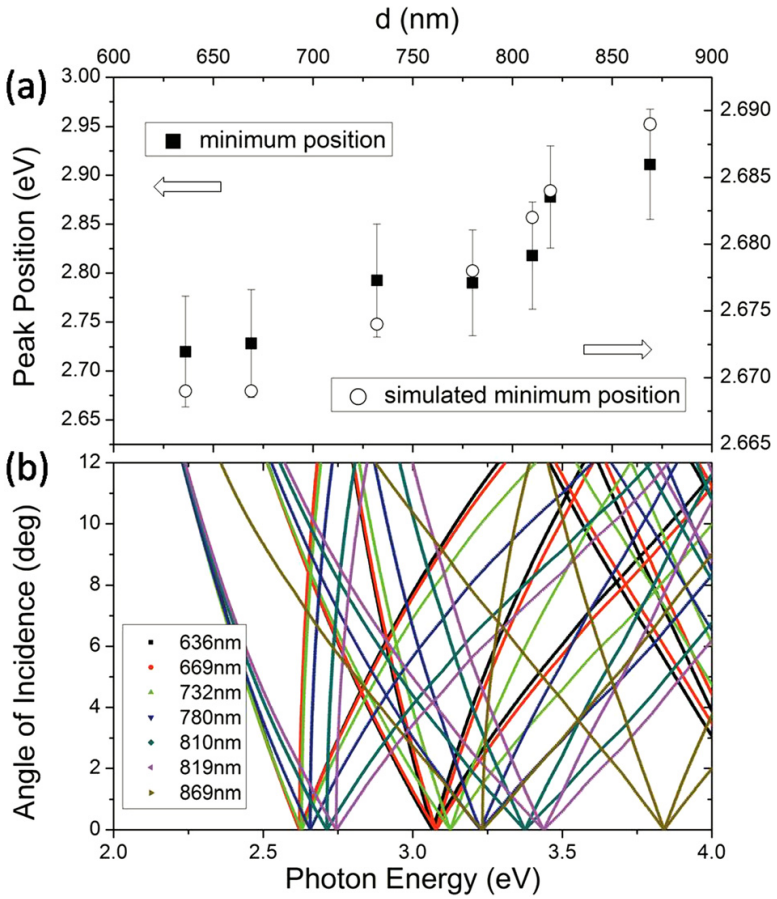

Figure 4.11: (a) Photon energy of the first structure in the polar Kerr spectra as a function of hole diameter d as derived from experimental data (solid squares) and theory (open circles). Note the different scaling. (b) Calculated dispersion relation of the Bragg plasmons at the Ni/air interface as a function of angle of incidence for different hole diameters.

curves are in fair agreement except for the size of the shift. The large error bars in the experimental data result mainly from the broadness of the structures. The broadening, and in part, the discrepancy in the size of the shift is due to the finite angle of incidence of $\sim 3^{\circ}$ used in the MOKE set-up as explained by a detailed calculation of the dispersion relation of the Bragg plasmons shown in Fig. 4.11(b). For varying angle of incidence, it reveals an asymmetric splitting of the Bragg peaks. For an angle of incidence of 3°, the splitting amounts to ~ 0.2 eV. Due to the limited photon-energy resolution of the MOKE spectrometer, the splitting is merely observed as an additional broadening of the peaks. This has been taken into account in the error bars. The asymmetry of the splitting,

on the other hand, will increase the hole-size-dependent shift because the branching is larger on the high-energy side yielding a better agreement with experiment.

In conclusion, we have analyzed the optical and MO effects of thin Ni films perforated with nanohole arrays, where a large lattice parameter was kept constant while varying the hole diameter. We have observed an enhancement of the absolute value of the polar Kerr rotation at two different energies that we have attributed to the excitation of SPPs. The broadening of the experimentally observed plasmon resonances was explained by the splitting of the Bragg peaks as a function of angle of incidence. We have also shown that the minima in the Kerr rotation spectra move to lower energies when decreasing the hole size. This dependence is qualitatively explained by introducing an effective metal permittivity constant directly proportional to the amount Ni-air of the membrane.

4.4 Conclusions

All in all, we have investigated the polar and transverse magneto-optical Kerr effects in ferromagnetic films with a periodic array of subwavelength holes, comparing theory and experiment.

In particular, we have shown that the TMOKE signal can be resonantly enhanced when the samples are illuminated with an appropriate wavelength. Similarly, pronounced maxima of the absolute value of the Kerr rotation were observed at certain energies. Through the analysis of the Bragg plasmons, we were able to attribute the enhancement observed in the MO properties of the system to the excitation of surface plasmon polaritons which can lay at either interfaces (air/ferromagnetic-metal interface or ferromagnetic-metal/substrate interface).

We have also addressed the optical and magneto-optical properties of Ni nanohole arrays with large lattice parameter varying the hole diameter while keeping the lattice periodicity constant. Although the lattice parameter of the array was kept constant, we have shown that the position of the minimum of the Kerr rotation was red shifted when decreasing the hole size. It was possible to qualitatively explain this dependence by introducing an effective metal-dielectric constant instead of the bulk ferromagnetic permittivity constant when computing the Bragg equation. This fact indicates that such membranes behave as an "effective" material when a surface plasmon is excited.

5 Hybrid nanohole arrays: Faraday rotation

We have seen in previous chapters that the propagation of electromagnetic waves in the visible range through metal arrays of subwavelength holes is governed by the extraordinary optical transmission, phenomenon that has been explained in terms of the resonant excitation of surface plasmons polaritons (see sec. 1.1). Thus, it seems natural when investigating the magneto-optical effects of magnetoplasmonic nanohole arrays and its interplay with SPPs to focus on the study of the transmitted waves, i.e., the Faraday effect. However, despite the fact that the MO Kerr effect for reflected waves has been extensively investigated in ferromagnetic nanohole arrays (see chapter 4), it is very remarkable that the Faraday effect in arrangements where the MO activity resides in the nanostructured part of the system has not been studied in detail and only a few works in literature deal with transmission in such systems [97]. Previous investigations of the MO properties of transmitted light were carried out for systems where the nanostructuration was restricted to the non-magnetic material, usually nanostructures where the MO active material was either a continuous layer [31, 46] or the material filling the holes [98]. The work presented in this chapter fills the existing gap in literature performing an in-depth study of the Faraday effect in nanohole arrays where the MO activity resides in the nanostructured membrane. In order to take the most of it, the system proposed for the study comprises both a ferromagnetic material and a noble metal. This fact is very advantageous since, as we saw in sec. 1.1, the combination of such materials enhances the MO activity of the system. Furthermore, to the best of our knowledge, there are no previous studies of hybrid sub-wavelength-hole periodic arrays (including noble and ferromagnetic metals).

Thus, in this chapter we present a systematic theoretical analysis of the Faraday effect in hybrid Au-Co-Au membranes with two-dimensional periodic arrays of sub-wavelength holes. We show that the combination of noble and ferromagnetic metals leads to an improvement of the performance of these nanohole arrays as Faraday rotators, i.e., present a better

trade-off between high transmittance and high Faraday rotation. In particular, we show that the excitation of the surface plasmons responsible for the occurrence of the extraordinary optical transmission gives rise to an enhancement of the Faraday rotation that coexists with the relatively high transmission. Moreover, as the MO response in hybrid nanostructures is sensitive to the amount of electromagnetic field probing the active material [99–101], we find that the analysis of the Faraday effect in these nanohole arrays provides a further insight into the origin of the extraordinary transmission.

5.1 System under study: Au-Co-Au nanohole array

The system that we investigate in this work consists of a hybrid Au-Co-Au[1] perforated membrane featuring a periodic array of sub-wavelength holes forming a square lattice, see Fig. 5.1(a). The Co layer, which is sandwiched between the two Au layers, has a thickness of t_{Co} and it is located at a distance d from the upper part of the membrane, see Fig. 5.1(b). Unless otherwise stated, we assume that the substrate is made of glass with a refractive index of 1.5 in the whole visible range and the incident medium is air. For the sake of concreteness, the lattice parameter of the hole array is 400 nm, the hole diameter is 228.6 nm (lattice parameter/1.75), and the total thickness of the membrane is 250 nm. These numbers were inspired by the experiments of [103] where the optical transmission was investigated in nanohole arrays of several noble and transition metals. Let us emphasize that with this choice for the geometrical parameters of the system, the optical transmission through these sub-wavelength-hole arrays is dominated by the extraordinary optical transmission.

5.2 Analysis of the Faraday effect in hybrid nanohole arrays

Our main goal is the theoretical analysis of the Faraday effect in the above-mentioned hybrid nanohole arrays. Let us remind that this magneto-optical phenomenon consists in a rotation of the polarization plane, θ_F,

[1] The optical constant of Au used in the calculations were taken from [102], while the optical and magneto-optical constants of Co were taken from [87].

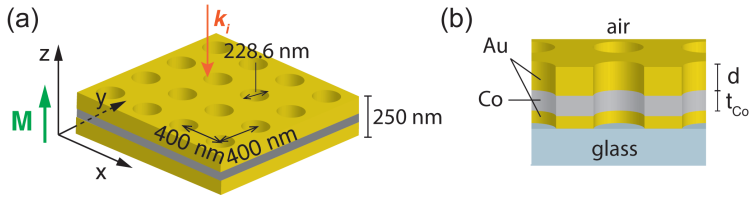

Figure 5.1: (a) Schematic representation of the system under study where one can see the Au-Co-Au perforated membrane with a periodic array of holes forming a square lattice. We specify the values of different geometrical parameters such as the lattice constant, the hole diameter, and the membrane total thickness. We also indicate that in the Faraday configuration the Co magnetization, M, is perpendicular to the plane of the membrane and parallel to the light propagation. (b) Lateral cut of the hybrid membrane that sits on a glass substrate. We define here the Co thickness, t_{Co}, and the Co depth or distance between the Co layer and the upper part of the membrane, d.

and a change in the ellipticity, η_F, of the transmitted light (with respect to the incident light) when the magnetization of the sample is parallel to the direction of the light propagation (see sec. 2.2.2). In our case, we shall assume that the light has a perpendicular incidence and it is polarized along the x-axis, which coincides with the high symmetry direction of the square lattice, see Fig. 5.1(a). In this section we focus on the analysis of the magnitude of the polarization conversion, $|t_{yx}|$, since this quantity represents the purely magneto-optical contribution and leads us to a better understanding of the physics behind our system. It is also customary to quantify the magneto-optical activity by combining the rotation and ellipticity in the following quantity: $\Phi_{\mathrm{F}} = \sqrt{\theta_F^2 + \eta_F^2}$, which we report in degrees. On the other hand, since it is highly desirable that a Faraday rotation be accompanied by a high transmission, to assess the performance of the system as a Faraday rotator it is convenient to define a figure of merit (FoM) as the product of Φ_{F} and the zero-order transmittance (for x-polarized light), T, *i.e.*

$$\mathrm{FoM} = \Phi_{\mathrm{F}} T. \tag{5.1}$$

5.2.1 Influence of the thickness and position of the Co layer

Here we present a detailed study of the Faraday effect in our Au-Co-Au perforated membranes as a function of both the thickness of the Co layer, t_{Co}, and its position d measured with respect to the upper part of the membrane.

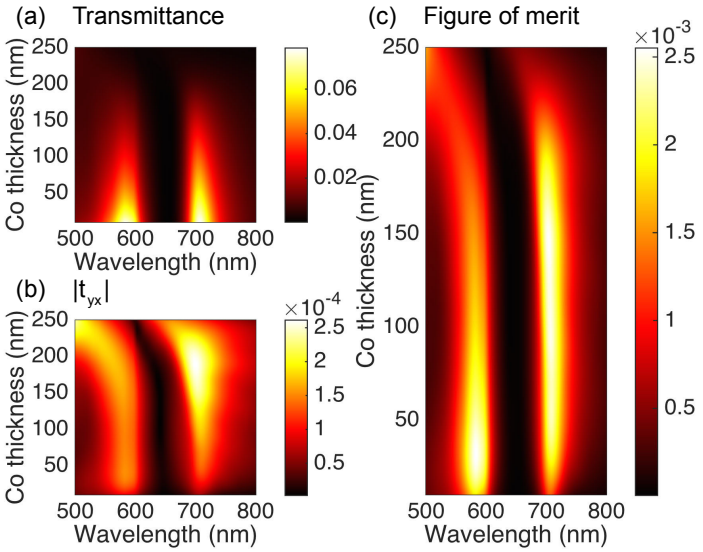

Figure 5.2: (a) Transmittance as a function of the wavelength and the thickness of the Co layer, which lies in the middle of the structure. (b) The corresponding magnitude of the coefficient t_{yx} that describes the polarization conversion of the transmitted light. (c) FoM, as defined in Eq. (5.1).

Let us start analyzing how the amount of Co influences the Faraday rotation and the corresponding figure of merit. In Fig. 5.2 we show the results for transmittance T, the polarization conversion in the transmitted light $|t_{yx}|$, and the corresponding figure of merit. These quantities are shown as colormap as a function of the wavelength and the thickness of the Co layer. The Co layer is kept in the middle of the structure and its thickness varies from 10 nm to 250 nm (this latter value corresponds to a pure Co system).

Starting with the results for the transmittance, shown in Fig. 5.2(a), notice first that for the thinest Co layer ($t_{\mathrm{Co}} = 10$ nm), the transmittance exhibits two maxima at wavelengths around $\lambda_1 = 585$ nm and $\lambda_2 = 710$ nm, which are very close to the spectral position of the two maxima observed in pure Au nanohole arrays [103]. These maxima are the manifestation of the extraordinary optical transmission and they are reported to originate from the excitation of the SPPs in both Au-dielectric interfaces. To be precise, a simple analysis of the Bragg plasmons in these nanohole arrays with Eq. (2.6) of sec. 2.1.2, points to that the maximum around λ_1 has a mixed character, and is mainly due to the excitation of the SPP in the air-Au interface with a weaker contribution from a second order plasmon formed in the back interface. On the other hand, the

transmittance maximum around λ_2 is due to the SPP in the Au-glass interface, see sec. 5.2.3 below. The mixed character of the high frequency maximum will unravel itself along the manuscript. As the Co thickness increases, the transmittance not only decreases, but the maxima are also shifted to smaller wavelengths, reaching values of 460 nm and 660 nm respectively when the film is 100% Co. The reduction of the transmittance is a simple consequence of the larger absorption in Co, as compared to Au (notice that there is also a broadening of the peaks, also consequence of a larger absorption). Paying attention now to the polarization conversion, see Fig. 5.2(b), the situation is basically reversed, *i.e.* the conversion progressively increases as the amount of Co increases in the structure and the maxima occur approximately at the same wavelength as the maxima in the transmittance of the nanohole array without Au. Notice, however, that the polarization conversion does not reach a maximum when the Au is entirely removed. This illustrates the fact that the presence of a Au layer next to the incident medium is beneficial for both the transmittance and the magneto-optical properties, which is due to the low-damping SPPs excited in the air-Au interface.

Finally, when combining these two properties into the figure of merit to find the best compromise between a large rotation and a good transmittance, see Fig. 5.2(c), we find that there is no a unique optimal configuration for the whole visible range. Depending on the working range of wavelengths, it would be possible to choose between two different configurations. For smaller wavelengths, an optimal configuration is reached when $t_{\mathrm{Co}} \simeq 30$ nm, while for larger wavelengths the choice would be $t_{\mathrm{Co}} = 150$ nm. It is worth remarking that in both cases, the figure of merit of these hybrid systems can reach values that are more than one order of magnitude larger than in the case of a pure Co nahohole array.

Let us now analyze the role of the position of the Co layer, as it has been reported to play an important role in both continuous films [99, 101] and disks [100]. For this purpose, we have fixed the thickness of the Co layer to $t_{\mathrm{Co}} = 10$ nm (this thickness is enough to have a reasonable MO activity while it does not perturb significantly the internal electromagnetic field [100]) and varied its position from $d = 0$ (top of the membrane) to $d = 240$ nm (bottom of the membrane). In Fig. 5.3 we gather the results for the transmittance, polarization conversion, and figure of merit as a function of both the wavelength and the distance d. The first thing to notice is that for all positions of the Co layer, there is a maximum for the three quantities around λ_1 and λ_2. However, when the Co is placed close to the top the transmittance around λ_1 exhibits a broadened, damped

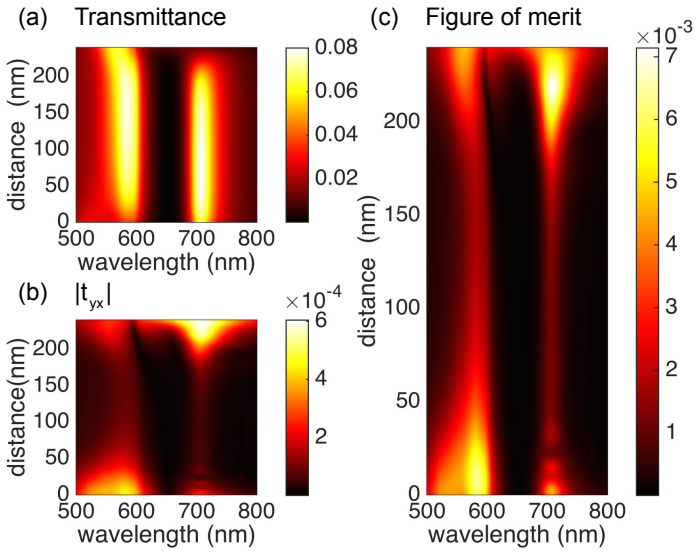

Figure 5.3: (a) Transmittance as a function of the wavelength and the position of a 10 nm-thick Co layer, measured with respect to the upper part of the hybrid membrane. (b) The corresponding value of the polarization conversion $|t_{yx}|$ and (c) figure of merit.

maximum, while the one around λ_2 is more intense and sharper. Conversely, the polarization conversion and the figure of merit exhibit a maximum more intense and broader around λ_1. This is a clear indication of the influence of the Co on the plasmon at the top interface, with a larger influence on the polarization conversion and broadening of the features. The situation is reversed when the Co layer is placed close to the bottom, the transmittance peak around λ_2 appears damped and broadened, whereas the polarization conversion and figure of merit reaches its maximum. However, the features at λ_1 also experiment modifications, such as a weak damping and blue shift of the transmission peak, as well as a pronounced enhancement of the figure of merit and polarization conversion. This reflects the fact that there is an influence of a plasmon excitation at the back side, pointing to the aforementioned mixed character of the mode occurring at λ_1.

In this case, as one can see in Fig. 5.3(c), the best compromise between reasonable transmission and large Faraday rotation for wavelengths around λ_1 is found when the Co layer is close to the top, but not right at the top, to avoid the large damping due to the high absorption of Co. For wavelengths close to λ_2, it is best to place the Co close to the bottom, but, for the same reason, not at the very bottom. These results for the figure

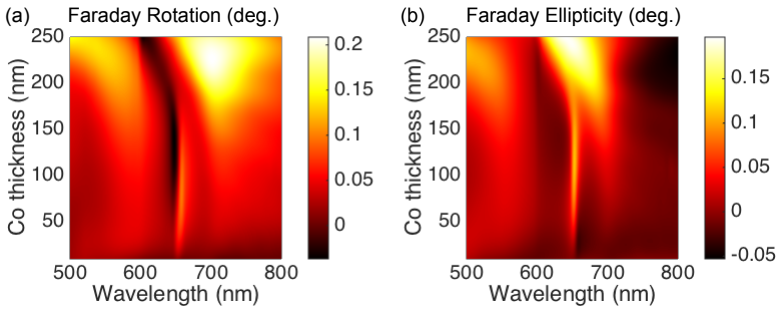

Figure 5.4: (a) Faraday rotation and (b) Faraday ellipticity as a function of the wavelength and the thickness of the Co layer, which lies in the middle of the structure. The results correspond to those of Fig. 5.2.

of merit are easy to interpret and, in turn, they provide a very useful insight into the origin of the underlying extraordinary optical transmission. It is obvious that the maximum in the figure of merit close to λ_1 that appears at $d \approx 10$ nm is due to the resonant excitation of the SPP at the air-Au interface. Similarly, the maximum of the figure of merit around λ_2 appears at $d \approx 220$ nm because of the excitation of the corresponding SPP at the Au-glass interface. As we illustrate below in sec. 5.2.3, surface plasmon excitation enhances the electromagnetic field at the interfaces and, therefore, placing the Co layer close to the surface where the plasmon is excited we get an amplification of the electromagnetic field inside the ferromagnetic layer, which leads to an increase in the magneto-optical activity. The mixed character of the SPP around λ_1 is manifested by the peak for d close to the membrane-substrate interface. The larger absorption in Co makes it disadvantageous to place the layer of this material right at the top or bottom of the membrane.

Faraday rotation and ellipticity

Throughout this section we have evaluated the performance of our nanohole arrays in terms of the figure of merit, FoM, and the polarization conversion, $|t_{yx}|$. For completeness, we report here the Faraday rotation, $\theta_F = \mathrm{Re}\{t_{yx}/t_{xx}\}$, and ellipticity, $\eta_F = \mathrm{Im}\{t_{yx}/t_{xx}\}$, of our Au-Co-Au membranes for the two issues just discussed. Fig. 5.4 illustrates the Faraday rotation and ellipticity corresponding to the first issue where we place a Co layer in the middle and vary its thickness from 10 nm to 250 nm. As one can see, the maximum Faraday rotation takes place at around 700 nm and when the structure does not contain almost any Au. This seems

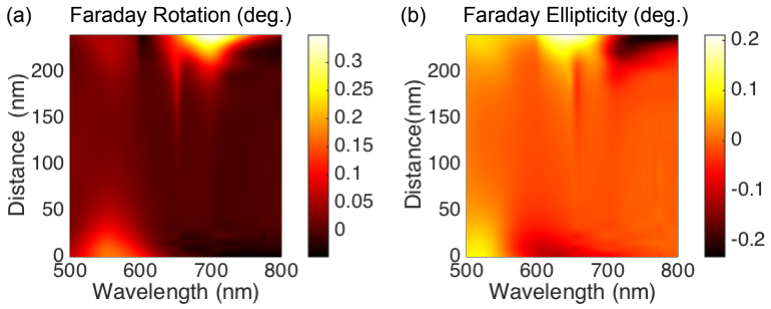

Figure 5.5: (a) Faraday rotation and (b) Faraday ellipticity as a function of the wavelength and the position of a 10 nm-thick Co layer, measured with respect to the upper part of the hybrid membrane. The results correspond to those of Fig. 5.3.

to suggest that it is deleterious to include Au in the structure. However, this impression is wrong since the maximum of the Faraday rotation is accompanied by a vanishing transmission, see Fig. 5.2(a), which is obviously not desirable. This fact nicely illustrates why it is much more convenient in our case to gauge the performance of the device in terms of the figure of merit introduced in Eq. (5.1). Finally, we display in Fig. 5.5 the Faraday rotation and ellipticity of our system with a 10 nm-thick Co layer as a function of its distance from surface, which correspond to the results shown in Fig. 5.3.

5.2.2 Dependence with the incident medium and substrate refractive index

So far, we have kept fixed the refractive index of the incidence and the substrate media. In what follows, we show that the polarization conversion, and the corresponding figure of merit, can be further tuned (both in magnitude and in wavelength) by playing with the dielectric material both in the medium of incidence and in the substrate. In Fig. 5.6 we show the same information as in the previous figures, but now as a function of the wavelength and of the refractive index of the medium of incidence, n_{inc}. In this case, we have fixed the refractive index of the substrate to $n_{\text{subs}} = 1.5$ and the Co layer has a thickness of 50 nm and it is placed in the center of the membrane, *i.e.* $d = 100$ nm. For single metal membranes, it has been established, both experimentally and theoretically, that the transmittance of a nanohole array is maximized when the incidence medium and the substrate are made of the same material [104]. The results of Fig. 5.6 not only confirm this idea, but they also show that

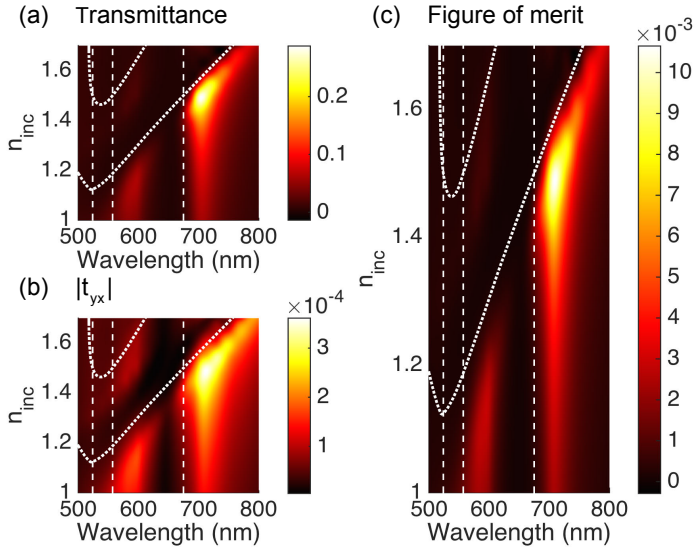

Figure 5.6: (a) Transmittance as a function of the wavelength and the refractive index of the medium of incidence. The refractive index of the substrate is 1.5. The Co layer has a thickness of 50 nm and it is placed in the middle of the membrane. (b) The corresponding value of $|t_{yx}|$ and (c) figure of merit. In all the panels, the short-dashed lines correspond to the position of the Bragg SPPs of the interface between the incidence medium and the upper Au layer, while the vertical long-dashed lines indicate the position of the Bragg SPPs in the interface between the lower Au layer and the substrate.

the polarization conversion and the figure of merit reach a maximum in the symmetric situation $n_{\text{inc}} = n_{\text{subs}}$. In this symmetric case the SPPs of the upper and lower interface are excited at the same wavelength and the maxima in the different quantities appear at λ_2. It is worth noticing that when the refractive index of the incidence medium is 1.5 there is a peak at λ_1, albeit much less intense than that at λ_2. This points to the appearance of a second SPP at λ_1 for $n_{\text{inc}} = 1.5$, explaining the mixed character of the SPP at λ_1.

To give further insight of the mentioned effect we plot in Fig. 5.6 the position of a continuous-film SPP with parameters equivalent to those of the upper interface (short-dashed lines) and its evolution as the refraction index of the incidence medium is varied. A continuous-film SPP with parameters equivalent to those of the substrate is also plot (long-dashed lines). All the SPPs alluded in this section referred to the Bragg plasmons of a single interface between a metal and a dielectric. These SPP positions were calculated with Eq. (2.6), that for the case of normal incidence,

$\theta = 0$, reduces to

$$\lambda = \frac{a_0}{\sqrt{i^2 + j^2}} \sqrt{\frac{\epsilon_d \epsilon'_m(\lambda)}{\epsilon_d + \epsilon'_m(\lambda)}}, \tag{5.2}$$

where remember that a_0 is the lattice parameter which for our system is 400 nm, i and j denote the order of the surface plasmon resonances and $\epsilon_{\mathrm{d}} = n^2_{\mathrm{inc/subs}}$ and $\epsilon_{\mathrm{m}}(\lambda)$ represent the permittivity constants of the dielectric and the metal, respectively. In this case, we have simply considered the metal permittivity $\epsilon_{\mathrm{m}}(\lambda)$ to be a geometrical average of $\epsilon_{\mathrm{Au}}(\lambda)$ and $\epsilon_{\mathrm{air}} = 1$. It should be noticed that the approximation is far from accurate for small wavelengths, since the size of the hole becomes more similar to that of the wavelength of the incident light.

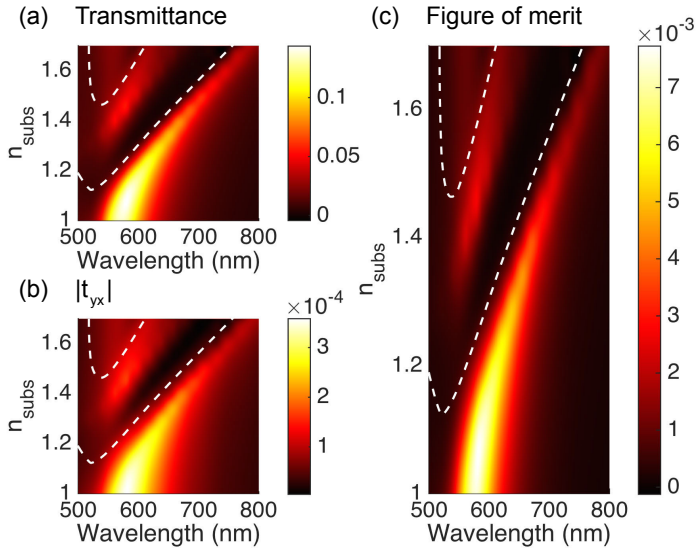

Figure 5.7: (a) Transmittance as a function of the wavelength and the refractive index of the substrate. The refractive index of the incident medium is 1.5. The Co layer has a thickness of 50 nm and it is placed in the middle of the membrane. (b) The corresponding value of $|t_{yx}|$ and (c) figure of merit. In all the panels, the dashed lines correspond to the position of the Bragg SPPs of the interface between the lower Au layer and the substrate.

Similarly, the same quantities can be tuned by changing the refractive index of the substrate, n_{subs}. This is shown in Fig. 5.7 where we display the three quantities as a function of the wavelength and n_{subs}. In this case, we have fixed n_{inc} to 1 and use the same geometrical parameters of the membrane as in Fig. 5.6. As it can be seen, in Fig. 5.7, the transmittance, the polarization conversion, and the figure of merit are again maximal in

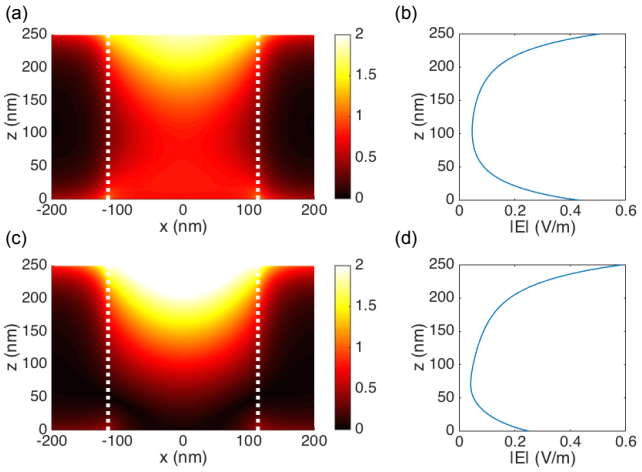

Figure 5.8: (a) and (c) Cross section of the electric field distribution in the Au membrane at the resonance wavelength ($\lambda = 710$ nm) and out-of-resonance ($\lambda = 655$ nm), respectively. White dotted line represents the hole boundaries. (b) and (d) Mean value of the electric field in the Au membrane along the z-axis for $\lambda = 710$ nm and $\lambda = 655$ nm, respectively. These calculations have been carried out with the modeling software COMSOL Multiphysics.

the symmetric case $n_{\text{inc}} = n_{\text{subs}}$. Obviously, this time the maximum in the different quantities appears at λ_1, when the wavelength of the SPP of the upper and lower interfaces when the refraction index is equal to 1. Notice also that at a given value of n_{subs}, the maximum of the three quantities appears at the position of the SPP of the lower interface, and a second SPP appears, being close to λ_1 for $n_{\text{subs}} = 1.5$.

5.2.3 Electric field and surface plasmon excitation

In order to illustrate the excitation of a surface plasmon in a nanohole array, in this subsection we present the distribution of the electric field inside a Au nanohole array with the same dimensions at two different wavelengths, one corresponding to the substrate surface plasmon resonance, Fig. 5.8(a) and Fig. 5.8(b), and one out-of-resonance wavelength, Fig. 5.8(c) and Fig. 5.8(d). First, let us compare the distributions of the electric field in a cross-section (xz-plane at $y = 0$) of the Au membrane corresponding to the resonance and out-of-resonance wavelengths, Fig. 5.8(a) and Fig. 5.8(c), respectively. We can unmistakably see an enhancement of the electric field inside the lower part of the hole at the wavelength where a plasmon excitation takes place. This situation is in

accordance with the phenomenon of the extraordinary optical transmission reported for that concrete wavelength [103]. Moreover, we see that the electric field at the base of our membrane - substrate interface - is enhanced compared to the field at the wavelength where we do not expect to have any plasmon resonance. To see this fact more clearly, we have depicted the magnitude of mean value of the electric field inside the metallic part of the membrane along the z-axis, Fig. 5.8(b) and Fig. 5.8(d). In Fig. 5.8(b) we observe a noticeable enhancement of the electric field close to the substrate ($z = 0$), which corroborates a surface plasmon polariton excitation at $\lambda = 710$ nm. As we state in sec. 5.2.1, this localized enhancement of the electric field in the membrane due to the presence of the surface plasmon leads to the amplification of the MO activity of the system when the ferromagnetic material is present due to the consequent enhancement of the electromagnetic field inside the ferromagnetic layer.

5.3 Conclusions

We have shown that the Faraday polarization conversion in a magneto-plasmonic crystal made of a perforated membrane with a period array of sub-wavelength holes can be greatly enhanced by combining ferromagnetic and noble metals. This enhancement originates from the phenomenon of the extraordinary optical transmission, which in turn stems from the resonant excitation of SPPs at the interfaces of these nanohole arrays. We have illustrated this idea with a systematic analysis of the Faraday effect in a hybrid Au-Co-Au nanohole array. We have shown that the performance of these metallic membranes as Faraday rotators can be maximized, for a certain wavelength range, by placing the Co layer close to the upper or lower interfaces, but not right at the edge. In both cases, the enhanced performance is due to the excitation of the SPPs in the outer Au layer. This excitation leads to an enhancement of the electromagnetic field in the Co layer, which in turn is reflected as an increase in the magneto-optical signal (the polarization conversion). Moreover, we have shown that the analysis of the magneto-optical activity of these nanohole arrays provides a new insight into the extraordinary optical transmission. Finally, we can anticipate that the combination of ferromagnetic and noble metals in the context of perforated membranes with periodic arrays of sub-wavelength holes may lead to a dramatic enhancement of a variety of magneto-optical phenomena.

6 Hybrid nanohole arrays: sensing

In this chapter we show that the transverse magneto-optical Kerr effect in hybrid nanohole arrays is also largely enhanced due to the interplay between the magneto-optical properties of the ferromagnetic membrane and the excellent plasmonic properties of noble metals. In particular, we propose to use Au-Co-Au films perforated with a periodic array of sub-wavelength holes as transducers in magneto-optical surface plasmon resonance sensors, where the sensing principle is based on these measurements of the TMOKE. We show that the MO response of these systems is characterized by extremely sharp Fano-like features very sensitive to changes in the refractive index of the surrounding medium. In fact, as we illustrate below, the corresponding sensing figure of merit of these hybrid systems can be several orders of magnitude larger than that of other plasmonic sensors, including standard nanohole arrays, surface-plasmon-resonance and magneto-optical surface-plasmon-resonance sensors, and sensors based on localized surface plasmon resonances.

6.1 Plasmonic sensors: the state of the art

Plasmonic structures are widely used in low-cost, label-free biosensors and the investigation of how to improve their sensitivity or to widen their range of applications is a central topic in the field of plasmonics [13, 14]. The most commonly used plasmonic sensors are based on the concept of SPR and its sensitivity to refractive index changes [5, 6]. These SPR-based sensors are commercially available and they are able to detect changes on the refractive index of the sensing medium as small as 10^{-7}. In the search for an improved bulk sensitivity of SPR-based sensors, researchers have proposed different strategies. Thus, for instance, it has been shown that the use of the MO properties of layered systems containing magnetic materials can, in principle, enhance the sensitivity of

these sensors [37–42]. Another possibility that is becoming increasingly popular is the use of nanohole arrays or perforated metallic membranes featuring arrays of sub-wavelength holes [105–119]. These sensors make use of the extraordinary optical transmission phenomenon [55, 56], which originates from the resonant excitation of surface plasmons in these periodically patterned nanostructures. Nanohole arrays exhibit a series of advantages over conventional SPR-based sensors. First of all, since these periodic systems do not require of additional prisms to excite the plasmonic modes, they can be more easily miniaturized and integrated in nanoscale devices. Also, nanohole arrays are compatible with imaging-based devices and can be implemented in a microarray format for multiplexed and high-throughput biosensing [120]. Besides, nanohole arrays can also be combined with microfluidic systems to implement real-time analysis of biomolecular binding kinetics. Furthermore, since these perforated membranes are based on metal films, one can use the transducer surface as an electrode to implement additional techniques either for manipulating or for detecting molecules such as electrochemistry, dielectrophoresis, or resistive heating [118]. Finally, the performance and operational parameters (wavelength, refractive index range, etc.) can be further tuned in a straightforward way by, for instance, modifying the geometrical parameters in these arrays (lattice parameter, hole size and shape, membrane thickness, etc.) [121] or by engineering the substrate [119].

In spite of the attractive features of nanohole-based sensors described above, conventional SPR sensors are still the choice for most sensing applications. This is not only due to the fact that nanohole arrays require somehow more sophisticated, and therefore more expensive, fabrication techniques, but also due to the fundamental fact that normally nanohole-based sensors do not reach the sensitivity and resolution that is routinely achieved with SPR sensors. This lower spectral resolution is mainly due to larger radiative losses, which immediately translate into broader resonance line widths. Thus, one of the major open problems in the topic of plasmonic sensors is to find novel strategies to considerably boost the throughput of nanohole arrays as biosensors.

6.2 Hybrid nanohole arrays as sensors

In this context, the goal of this chapter is to show that the performance of nanohole arrays as plasmonic sensors can be dramatically enhanced by using hybrid perforated membranes containing both ferromagnetic and

noble metals as the nanohole array transducer (Fig. 6.1). The idea is to make use of the MO properties of these systems in the spirit of MO-SPR sensors [37–42], rather than measurements of the transmission at normal incidence as in standard nanohole-based sensing experiments. To be precise, we propose to make use of the TMOKE.

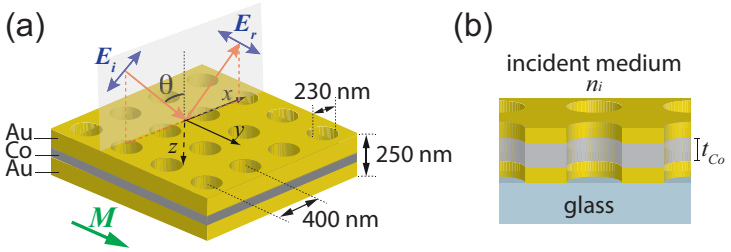

Figure 6.1: (a) Schematic representation of an Au-Co-Au perforated membrane with a periodic array of circular holes forming a square lattice. We display the values of different geometrical parameters such as the lattice constant, the hole diameter, the membrane total thickness, and the Co thickness, t_{Co}. We also indicate the Co magnetization, M, which is parallel to the plane of the membrane and perpendicular to the incidence plane. (b) Lateral cut of the hybrid membrane that is placed on a glass substrate.

In order to demonstrate the central idea of this work, we study the same structure as in chapter 5, a hybrid Au-Co-Au[1] perforated membrane with a periodic array of sub-wavelength circular holes forming a square lattice (Fig. 6.1(a)). Again, the Co layer is located in the middle of the structure and has a thickness t_{Co} (Fig. 6.1(b)). We consider that the substrate is made of glass with a refractive index of 1.5 in the whole explored wavelength range and the incident medium and the interior of the holes have a refractive index n_i ($n_i = 1$ for air). The dimensions of the membrane are the same as the ones stated in sec. 5.1 (see Fig. 6.1(a)).

As explained above, the sensing principle is based on the transverse MO Kerr effect. To be precise, the quantity of interest in this case is the TMOKE signal defined in sec. 2.2.3,

$$\mathrm{TMOKE} = \frac{R_{pp}(+M) - R_{pp}(-M)}{R_{pp}(+M) + R_{pp}(-M)}, \tag{6.1}$$

where in this case M is the magnetization of the Co layer. Let us remind that the TMOKE vanishes at normal incidence and therefore, it has to

[1] In our calculations, the optical constants of Au were taken from Ref. [102], while the optical and MO constants of Co were taken from Ref. [87].

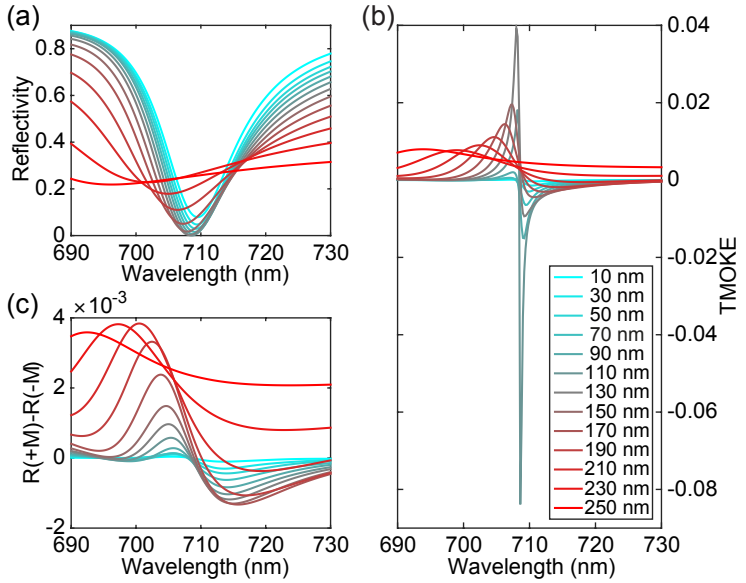

Figure 6.2: (a) Computed reflectivity, R_{pp}, for Au-Co-Au nanohole array where the Co layer is demagnetized ($M = 0$) as a function the wavelength of the incident light. The different curves correspond to different values of the Co thickness, t_{Co}, as indicated in the legend of panel (c). (b) The corresponding change in reflectivity upon reversal of the Co magnetization. (c) The corresponding TMOKE, as defined in Eq. (6.1).

be measured at a oblique incidence. Unless otherwise stated, we shall assume that the angle of incidence is $\theta = 45^{\mathrm{o}}$ and that the incident light propagates along the x-axis, as indicated in Fig. 6.1(a).

6.2.1 Optical and magneto-optical characterization

Let us start our analysis with the characterization of the optical and MO properties of the Au-Co-Au nanohole arrays assuming that the incident medium is air ($n_i = 1$). In Fig. 6.2(a) we show the reflectivity, R_{pp}, for a demagnetized sample ($M = 0$) as a function the wavelength and for different values of the Co thickness t_{Co}. We focus here on the wavelength range between 690 and 730 nm, which is where the important action takes place for our choice of geometrical parameters of the nanohole array. As one can see, the inclusion of Au in this membrane (or the reduction of the Co thickness) leads to the appearance of a pronounced minimum at around 709 nm where the reflectivity almost vanishes. As it will be shown in sec. 6.2.3, this minimum is due to the resonant excitation of a surface

plasmon polariton that appears in the air-Au interface. In Fig. 6.2(b) we display the corresponding change in reflectivity upon reversal of the magnetization, $R_{pp}(+M) - R_{pp}(-M)$. The main feature in this case is the change of sign that appears for many hybrid structures close to the reflectivity minimum. This change of sign stems from the small nonreciprocal variation in the surface plasmon wavevector induced by the magnetization of the Co layer [34]. This variation, which depends on the magnetization direction, shifts the reflectivity curves in opposite directions for different signs of M, which leads to a sign change in the difference $R_{pp}(+M) - R_{pp}(-M)$. Finally, we show in Fig. 6.2(c) the corresponding results for the TMOKE, as defined in Eq (6.1), which is our quantity of interest. As one can see, depending on the Co thickness, the TMOKE can adopt very large values accompanied by a change of sign close to the wavelength of the reflectivity minimum, exhibiting very sharp Fano-like line shapes. This line shape is especially sharp for a Co thickness $t_{\mathrm{Co}} = 110$ nm, which is the value that we shall consider for our analysis of the sensitivity and figure of merit for the rest of this chapter.

6.2.2 Sensitivity and figure of merit

Let us turn now to the central issue of this chapter, namely the use of these hybrid nanohole arrays for sensing applications. To illustrate this, we have studied how the TMOKE of the hybrid membrane with $t_{\mathrm{Co}} = 110$ nm is modified upon changing the refractive index of both the incident medium and the interior of the holes, n_i, presenting the results in Fig. 6.3(a). This analysis corresponds to what is referred to as flow-over sensing scheme [117], where the substrate is not modified during the sensing procedure. From the results shown in Fig. 6.3(a), one can see that the position of the Fano-like feature in the TMOKE curves is very sensitive to variations in n_i and is red shifted as n_i increases. This red shift is simply due to a change in the resonant condition of the surface plasmon excitation, which depends on the refractive index n_i (see sec. 6.2.3).

To quantify the sensing performance, we follow the usual practice and define the bulk refractive index sensitivity as $S = \Delta\lambda/\Delta n_i$, where $\Delta\lambda$ is the shift of the Fano-like feature and Δn_i is the change in the refractive index of the incident medium. As we show in Fig. 6.3(b), the sensitivity of our hybrid nanohole sensor is 659 nm/RIU. Since the actual accuracy in the tracking of the Fano-like feature also depends on its line width, the most relevant parameter defining the performance of this kind of devices is the figure of merit, obtained by dividing the bulk sensitivity S by the

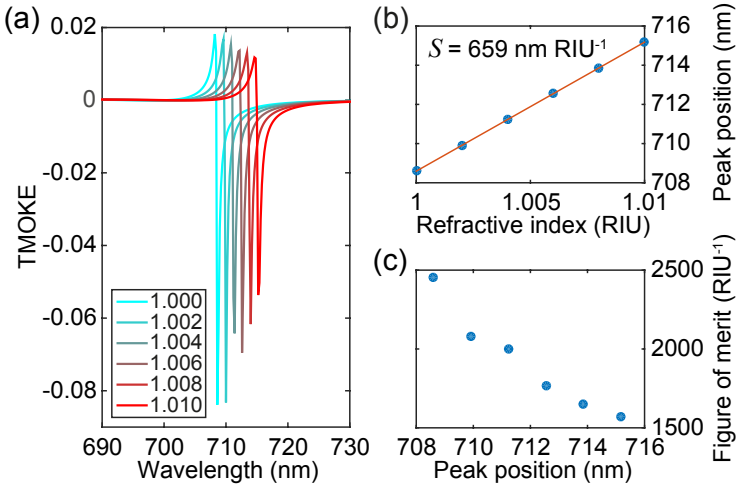

Figure 6.3: (a) TMOKE of a Au-Co-Au nanohole array with a Co thickness of 110 nm as a function of the wavelength of the incident light for different values of the refractive index of the incident medium, n_i, which is assumed to be the same as that of the holes. (b) Position of the Fano-like feature as a function of n_i. The blue symbols correspond to the results of panel (a) and the red solid line corresponds to a fit to a straight line, whose slope defines the bulk sensitivity of our device $S = \Delta\lambda/\Delta n_i = 659$ nm/RIU. (c) The corresponding figure of merit as a function of wavelength, see text for definition.

width of the Fano-like feature Γ, i.e., FoM $= S/\Gamma$. This quantity is widely accepted as a proper measure for the performance of plasmonic biosensors based on surface and localized plasmon resonances [14, 114, 122–124]. With these definitions, the extracted FoMs for our hybrid device reach huge values up to several thousands $(\text{RIU})^{-1}$, as we show in Fig. 6.3(c).

Calculation of Γ: fitting of TMOKE curves to Fano line shapes

To obtain Γ in an accurate manner, we fitted the TMOKE line shapes as a function of the wavelength, λ, to a Fano line shape of the form [114]

$$\text{TMOKE}(\lambda) = A + B\frac{(q\Gamma/2 + \lambda - \lambda_0)^2}{(\Gamma/2)^2 + (\lambda - \lambda_0)^2}, \tag{6.2}$$

where Γ describes the line width, λ_0 is the resonant wavelength that defines the position of the Fano-like feature, q is the Fano parameter, and A and B are constants describing the background and the overall peak height, respectively. In Fig. 6.4 we present the fits of the TMOKE curves shown in Fig. 6.3(a) to Fano line given by the above-mentioned

equation. The values of the different fit parameters for Fig. 6.4 are listed in Table Tab. 6.1. Notice that the fits are very accurate, which justifies our analysis of the TMOKE in terms of Fano line shapes.

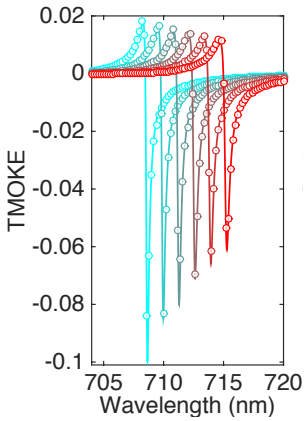

Figure 6.4: TMOKE vs. wavelength for different values of the refractive index of the incident medium for the cases reported in Fig. 6.3(a). The symbols correspond to the values of the TMOKE calculated with S-matrix formalism, whereas the solid lines correspond to the fits of those results to Fano line shapes (see Eq. (6.2)). The values of the fit parameters of the different curves are listed in Tab. 6.1.

Table 6.1: Parameter values of the fits of the TMOKE curves of Fig. 6.4 obtained using Eq. (6.2). Here, n_i is refractive index of the incident medium. The other parameters are described in the text.

n_i	λ_0 (nm)	q	Γ (nm)	A	B
1.000	708.596	-0.4284	0.2667	-0.09987	0.09938
1.002	709.908	-0.4335	0.3156	-0.08501	0.08451
1.004	711.223	-0.4343	0.3298	-0.08011	0.07956
1.006	712.546	-0.4324	0.3735	-0.07112	0.07057
1.008	713.857	-0.4407	0.3977	-0.06587	0.06529
1.010	715.182	-0.4367	0.4270	-0.06112	0.06054

6.2.3 Connection between Bragg SPPs excitation and the sensitivity to the refractive index

As we just explained, the origin of the reflectivity minima and the sharp TMOKE line shapes in our hybrid nanohole arrays is the excitation of a Bragg SPP in the interface between the upper gold layer and the incident

medium, which is a dielectric of refractive index n_i. This can be seen by means of an analysis of the resonant conditions for the excitation of these plasmon modes (see sec. 2.1.2 of chapter 2). Therefore, for a square lattice Eq. (2.6) tells us at which angle of incidence, θ, a SPP can couple to the incident light for a given wavelength.

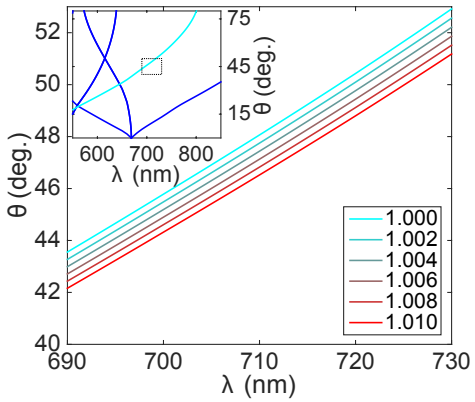

Figure 6.5: The main panel shows the angle of incidence at which a Bragg surface phonon polariton is excited at a given wavelength for an interface between an Au film and a dielectric corresponding to the medium of incidence. The different curves correspond to different values of the refractive index of the medium of incidence, as indicated in the legend. The inset, where light is assumed to come from the air, shows the corresponding dispersion relations for SPPs (dark blue lines) in a interface between Au and a glass of refractive index equal to 1.5, which corresponds to the substrate of our hybrid nanohole arrays. The light blue line corresponds to the SPP in an Au-air interface.

In the main panel of Fig. 6.5 we show the angle of incidence at which a Bragg SPP can be excited at a given wavelength in the interface between an Au film and the medium of incidence. The results are shown for different values of the refractive index n_i. These results show that the position of TMOKE sign change or the reflectivity minima (see Fig. 6.2(a)) roughly coincide with the SPP resonant condition derived with the help of Eq. (2.6). Moreover, the results of Fig. 6.5 allows us to understand why the relevant TMOKE features are red shifted when the refractive index n_i is increased. On the other hand, in the inset of Fig. 6.5 we also present the dispersion relation of the Bragg SPPs of an interface between an Au film and the substrate (a glass of refractive index $n_d = 1.5$), where it is assumed that light strikes from the air ($n_i = 1$). As one can see, there are no SPPs involving the substrate near $\theta = 45^o$ in the spectral range analyzed in this chapter. This fact rules out the possibility that the reflectivity minima (or the TMOKE features) discussed could be due

to the excitation of a SPP in the interface between the lower Au film and the substrate.

6.3 Comparison with existing SPR and MO-SPR sensors

To put the numbers of sec. 6.2.2 into perspective, let us first remind that conventional SPR-based sensors made of gold films using the Kretschmann configuration have a theoretical upper FoM limit of around 108 $(\mathrm{RIU})^{-1}$ [125], which is more than an order of magnitude smaller than the FoM of our hybrid nanohole arrays. In the context of nanohole-based sensors, let us mention that a very recent work based on high-quality Au nanohole arrays with engineered substrates has reported a similar bulk sensitivity of 671 nm/RIU, but a much smaller FoM of 42 $(\mathrm{RIU})^{-1}$ in a similar wavelength range [119]. To our knowledge, the record FoM in nanohole-based sensors is around 162 and it was obtained using the extraordinary light transmission phenomenon through high-quality factor subradiant dark modes [114]. Thus, we see that our proposal can indeed lead to an improvement of the record for the FoM by more than an order of magnitude. On the other hand, recent advances in plasmonic sensing that make use of localized SPRs have boosted their performance and FoMs of about 100-150 $(\mathrm{RIU})^{-1}$ have been recently reported [123, 124], which are still much smaller than the values found here.

To further illustrate the high performance of our proposal, we have also compared our hybrid nanohole arrays with a successful realization of a MO-SPR-based sensor, which has been shown to be superior to standard SPR sensors [40]. This sensor comprises a Au-Co-Au planar trilayer made of thin films (15 nm Au/6 nm Co/25 nm Au), it makes use of the Kretschmann configuration, and it utilizes the TMOKE as a sensing signal, in the same spirit as in our hybrid nanohole arrays. In Fig. 6.6 we show a comparison of the TMOKE signals and FoMs computed for both types of sensors. In this case, and following the usual practice in MO-SPR sensors, we have calculated the TMOKE as a function of the angle of incidence and for a fixed wavelength (709 nm for the nanoholes and 632 nm for the planar thin film trilayer, for which this MO-SPR sensor was optimized). Notice also that in this sensing scheme the TMOKE of the hybrid nanohole arrays exhibits Fano-like line shapes that are very well suited for sensing purposes. In particular, we have used Eq. (6.2) to

fit the TMOKE line shapes in Fig. 6.6(a)-(b) replacing the wavelength by the angle of incidence. As we summarize in Fig. 6.6(c), the performance of our hybrid perforated membranes is again much better than in this MO-SPR sensor, reaching huge FoMs of up to 6000, which are more than 50 times larger than in conventional SPR-based sensors.

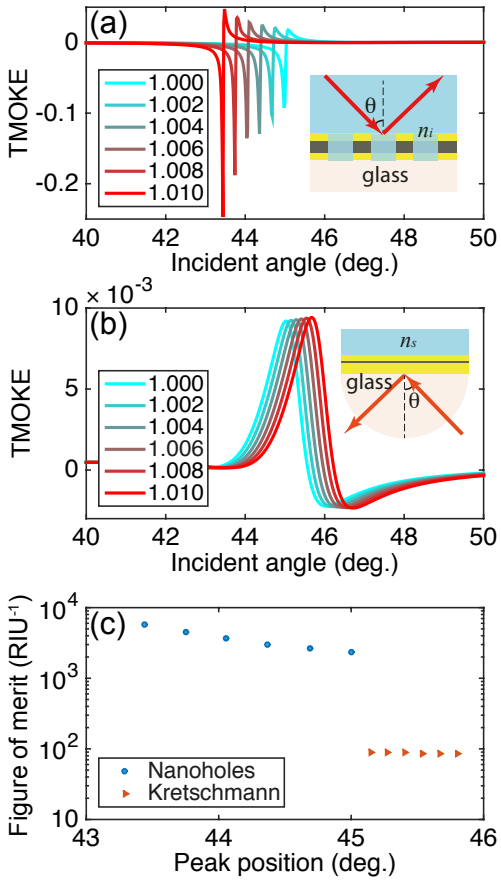

Figure 6.6: (a) TMOKE of a Au-Co-Au nanohole array with a Co thickness of 110 nm as a function of the angle of incidence and for a wavelength of 709 nm. The different curves correspond to different values of the refractive index of the incident medium. (b) The same as in panel (a) computed for a Au-Co-Au planar trilayer (15 nm Au/6 nm Co/25 nm Au) in the Kretschmann configuration and for a wavalength of 632 nm [40]. The prism in this scheme is a glass of refractive index equal to 1.5 and what is varied in this case is the refractive of the substrate, n_s. The inset shows a schematic representation of this MO-SPR sensor. (c) Comparison of the respective figures of merit of the sensors of panels (a) and (b).

It is fair to point out that our proposal certainly complicates the sensing setups. Apart from the additional difficulties in the fabrication method, the measurement of the TMOKE requires the incorporation of a magnet.

Moreover, the fact that the TMOKE has to be measured at a oblique incidence, in contrast to standard nanohole-based approaches, may influence the multiplexing capabilities of these sensors. However, we think that the tremendous improvement in the performance of the sensors clearly compensates those eventual disadvantages.

6.4 Feasibility

We would like to stress that the fabrication of the hybrid magnetoplasmonic crystals that we propose here is clearly feasible with present technology. In fact, hybrid nanohole arrays of various kinds have already been investigated experimentally [126, 127], including hybrid Au-Fe-Au magnetoplasmonic crystals fabricated by using self-assembled nanosphere lithography [128]. Let us also mention that the fabrication and characterization of cm^2 disordered nanohole arrays based on Au-Co multilayers have been recently reported [129], using a low-cost fabrication technique that also allows the fabrication of periodically ordered systems.

In this section we shall illustrate the case of a hexagonal lattice, since this is the arrangement that could be experimentally realized by self-assembly fabrication techniques, and show that the effects discussed in this chapter are rather universal and take place in different hole arrays. In order to obtain similar TMOKE features as in the square lattice case and in the same spectral range, we have chosen the geometrical parameters of the nanohole array with a triangular lattice as follows. First, the lattice parameter was chosen to be 462 nm to excite the relevant SPP in the upper Au film at the same wavelength as in the case of the square lattice described in this chapter. Second, the hole diameter was taken to be 246 nm in order to have the same filling factor as in the square lattice case. In Fig. 6.7 we show the computed TMOKE, bulk sensitivity, and figure of merit for a Au(70 nm)/Co(110 nm)/Au(70 nm) nanohole array with a triangular lattice of sub-wavelength circular holes with the geometrical parameters mentioned above.

As one can see, the results are very similar to those reported in Fig. 6.3, the main difference being that the TMOKE features are even sharper than in the square lattice case. This leads to an even higher figure of merit in the same spectral range, reaching huge values close to 3×10^4.

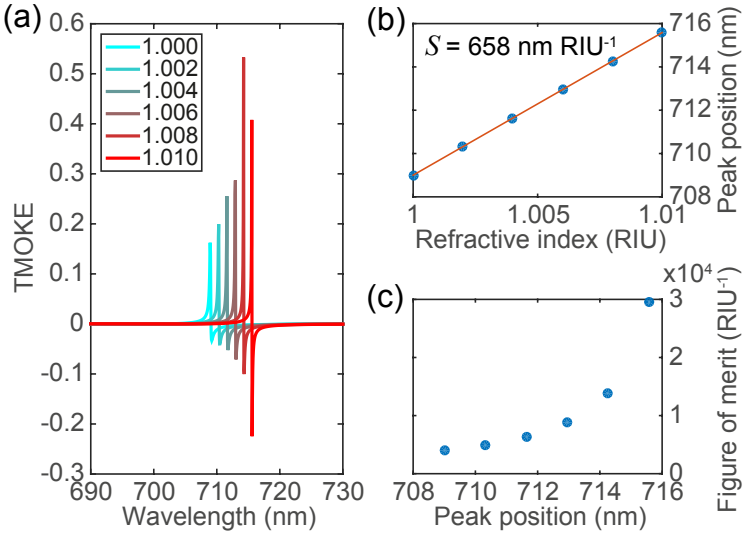

Figure 6.7: (a) TMOKE of a Au-Co-Au nanohole array with a triangular lattice of circular holes as a function of the wavelength of the incident light for different values of the refractive index of the incident medium, n_i. The thickness of the Co layer is 110 nm, the lattice parameter of the hole array is 462 nm, and the hole diameter is 246 nm. (b) The corresponding position of the Fano-like feature as a function of n_i. The blue symbols correspond to the results of panel (a) and the red solid line corresponds to a fit to a straight line, whose slope defines the bulk sensitivity of our device $S = \Delta\lambda/\Delta n_i = 658$ nm/RIU. (c) The corresponding figure of merit as a function of wavelength.

6.5 Conclusions

In summary, we have put forward a new feasible strategy for plasmonic sensing based on the use of hybrid magnetoplasmonic crystals and their MO properties. In particular, we have shown that the combination of the use of Au-Co-Au nanohole arrays with measurements of the transverse MO Kerr effect can lead to a tremendous enhancement of the figure of merit of this type of plasmonic sensors. In this respect, it is worth remarking that there is still plenty of room for improving the results reported here by modifying, for instance, the lattice parameters, hole shapes and sizes, membrane thickness, or by engineering the substrate. The impressive results that can be achieved with nanohole arrays with a hexagonal lattice reaffirm this idea, where figures of merit can be up to two orders of magnitude larger than those of the state-of-the-art plasmonic sensors. Thus, this proposal may resolve the central problem of nanohole-based sensors and it may also make them the natural choice for a wide variety of applications in the near future.

7 Summary conclusions

Throughout this thesis we have presented our contribution to the description of wave propagation in magnetoplasmonic systems. To conclude this dissertation, we proceed to summarize the main achievements reported in previous chapters.

First, we have presented a generalization of the scattering-matrix approach for the description of both the optical and magneto-optical properties of arbitrary periodically patterned multilayer structures comprising materials with any type of optical anisotropy. We have shown that the method presented is able to describe the magneto-optical effects in any configuration of the magnetic field, in particular the transverse and longitudinal magneto-optical Kerr effects, which were out of the scope of previous implementations of the scattering-matrix formalism. The key to succeed in this task has been solving the non-linear eigenvalue problem that describes the propagating eigenstates in periodically patterned layers where the permittivity tensor involves off-diagonal elements. Another important step forward in the implementation of this formalism has been the use of the so-called fast Fourier factorization, which has permitted to overcome the traditional convergence problems of scattering approaches when dealing with metallic periodic systems. All these elements have allowed us to develop a generalized scattering-matrix formalism, necessary to achieve the rest of the goals of this thesis.

The rest of the thesis has been devoted to the theoretical study of different magneto-optical effects in magnetoplasmonic nanohole arrays. With this in mind, we have first addressed three recent experiments conducted in ferromagnetic metallic films with hexagonal arrays of subwavelength holes where the magneto-optical activity in polar and transversal configurations had been measured. Here, our calculations performed with the scattering-matrix method developed in this thesis nicely reproduced the experimental results. Regarding the optical response of these ferromagnetic nanohole arrays, we could see different features at certain wavelengths (energies), such us dips in the reflectivity or pronounced maxima in the transmission, the so-called extraordinary optical transmission. At

those wavelengths, we also observed an enhancement of the TMOKE signal and of the Kerr rotation when the systems were in transversal and polar configurations, respectively. We have shown, via the calculation of Bragg plasmons, that the enhancement of the magneto-optical responses of our systems could be attributed to the excitation of surface plasmon polaritons at either the air-metal or metal-substrate interfaces. On the other hand, we have also analyzed the dependence of the optical and magneto-optical properties of the system with the hole size of the ferromagnetic membrane. We observed that the minima in the Kerr rotation were hole-size-dependent. The Kerr rotation minima were red-shifted when decreasing the hole diameter despite keeping the lattice periodicity constant. This was qualitatively explained by introducing an effective metal permittivity constant, directly proportional to the amount of metal (membrane) and dielectric (holes), in the dispersion relation used to compute the Bragg plasmons. This fact suggested that these nanohole arrays act as an "effective" material when supporting surface plasmon polaritons.

To go further in the study of the magnetoplasmonic nanohole arrays, we have proposed the incorporation of a noble metal into the structure in order to improve the plasmonic properties of the system, given that noble metals are characterized by lower losses which results in well defined plasmon resonances. Thus, the last part of this thesis was devoted to the theoretical study of Au-Co-Au films perforated with a periodic array of subwavelength holes. First, we have presented a study of the Faraday effect in such structures, where we have shown that the interplay between the extraordinary optical transmission and the magneto-optical activity leads to a resonant enhancement of the Faraday rotation, as compared to purely ferromagnetic membranes. In particular, we have determined the geometrical parameters for which this enhancement is optimized and showed that the inclusion of a noble metal like Au dramatically increases the magneto-optical signal (the polarization conversion) over a broad bandwidth. We have also shown that, for a certain wavelength range, placing the Co layer close to the upper or lower interfaces can maximize their performance as Faraday rotators, i.e., the system presents a very good trade-off between high transmittance and high Faraday rotation. We have attributed the enhanced performance to the excitation of the surface plasmon polaritons in the outer Au layer. We have shown that this excitation leads in turn to an enhancement of the electromagnetic field in the Co layer, which is reflected as an increase in the magneto-optical signal. Moreover, we have shown that the analysis of the Faraday rotation in these periodically perforated membranes provides a further

insight into the origin of the extraordinary optical transmission.

Finally, we have put forward the idea to use the aforementioned hybrid nanohole arrays as transducers in magneto-optical surface-plasmon-resonance sensors, where the sensing principle is based on measurements of the transverse magneto-optical Kerr effect. We have presented a detailed study that showed how the use of these hybrid structures leads to a tremendous enhancement of the performance of nanohole arrays as plasmonic sensors, which led to bulk figures of merit that are two orders of magnitude larger than those of any other type of plasmonic sensor. In this regard, it is worth remarking that there is still plenty of room for further optimization, investigating different lattice parameters, hole shapes and sizes, membrane thickness, or by engineering the substrate. Moreover, the sensing strategy proposed can make use of the different advantages of nanohole-based plasmonic sensors such as miniaturization, multiplexing, and its combination with microfluidics. Thus, we foresee that hybrid nanohole arrays will represent an important advance in sensing technology.

Conclusiones

A lo largo de la presente tesis doctoral hemos mostrado nuestra contribución a la descripción de la propagación de ondas en sistemas magnetoplasmónicos. A continuación, recogeremos los principales resultados expuestos a lo largo de los capítulos anteriores.

En primer lugar, se ha presentado una generalización del método de la matriz de *scattering* cuya finalidad es la descripción de las propiedades ópticas y magneto-ópticas de sistemas de multicapas nanoestructuradas de forma periódica formadas por materiales con cualquier tipo de anisotropía óptica. Hemos demostrado que el método desarrollado en la presente tesis doctoral es capaz de describir los efectos magneto-ópticos bajo cualquier configuración del campo magnético, en particular el efecto Kerr tanto transversal como longitudinal, cuya descripción quedaba hasta ahora fuera del alcance de las implementaciones previas del formalismo de la matriz de *scattering*. La clave del éxito para este cometido ha sido la resolución del problema de autovalores no-lineal que describe la propagación de los autoestados en capas periódicamente nanoestructuradas de materiales con elementos fuera de la diagonal del tensor dieléctrico. Otro hito importante a destacar en la implementación de este formalismo ha sido el uso de la denominada factorización rápida de Fourier, lo que ha permitido solventar los problemas de convergencia que tradicionalmente aparecen en el método de matriz de *scattering* al tratar de resolver sistemas periódicos metálicos. Todos estos elementos nos han permitido desarrollar un formalismo de matriz de *scattering* generalizado, que constituye la herramienta necesaria y fundamental sin la cual no se hubiera podido cumplir el resto de los objetivos fijados al comienzo de esta tesis.

Una vez desarrollado el marco teórico necesario, el resto de la tesis se ha dedicado al estudio teórico de los diferentes efectos magneto-ópticos en matrices ordenadas de nano-agujeros magnetoplasmónicas. Con esto en mente, hemos abordado tres experimentos recientes, realizados en películas metálicas ferromagnéticas perforadas con matrices hexagonales de agujeros cuyo tamaño es menor que el de la longitud de onda de la luz utilizada para medir la actividad magneto-óptica en configuraciones

polar y transversal. Bajo esta premisa experimental, los cálculos realizados utilizando el método de matriz de *scattering* generalizado presentado anteriormente reproducen de forma excelente los resultados experimentales. En cuanto a la respuesta óptica de estas láminas ferromagnéticas nanoestructuradas, se observan ciertos rasgos distintivos a determinadas longitudes de onda (energías), tales como estrechos mínimos en la reflectividad o máximos pronunciados en la transmisión, lo que se conoce como transmisión óptica extraordinaria. En esas longitudes de onda, también se observó una mejora de la señal al medir el efecto Kerr magneto-óptico en configuración transversal (TMOKE por sus siglas en inglés correspondientes a *"transverse magneto-optical Kerr effect"*) y de la rotación Kerr para configuraciones del sistema transversal y polar respectivamente. Hemos demostrado, a través del cálculo de los plasmones de Bragg, que la mejora de la respuesta magneto-óptica de estos sistemas podría atribuirse a la excitación de plasmones superficiales polaritones ya sea en la intercara aire-metal o metal-sustrato. Por otro lado, también hemos analizado la dependencia de las propiedades ópticas y magneto-ópticas del sistema con el tamaño de los agujeros de la membrana ferromagnética, observándose que los mínimos en la rotación Kerr dependen de dicho tamaño de agujero. Estos mínimos se desplazan al rojo (mayor longitud de onda) al disminuir el diámetro del agujero a pesar de mantener el parámetro de red, la distancia entre los centros de los agujeros, constante. Esto se explica de forma cualitativa mediante la introducción del concepto de permitividad efectiva del metal, que es directamente proporcional a la cantidad de metal (membrana ferromagnética) y dieléctrico (agujeros llenos de aire), en la relación de dispersión que se ha utilizado para calcular los plasmones de Bragg. Este hecho sugiere que estas redes de nano-agujeros ordenandos actúan como un material "efectivo" al soportar plasmones polaritones superficiales.

Con objeto de profundizar en el estudio de las redes magnetoplasmónicas de nano-agujeros, hemos propuesto la incorporación de un metal noble en la estructura con el fin de mejorar las propiedades plasmónicas del sistema; ya que es bien conocido en la literatura que los metales nobles se caracterizan por presentar menores pérdidas, lo que se traduce en resonancias de plasmón bien definidas. De este modo, la última parte de la presente tesis doctoral se ha dedicado al estudio teórico de multicapas híbridas compuestas por láminas de oro-cobalto-oro (Au-Co-Au) perforadas mediante una red periódica de agujeros sublongitud de onda. En primer lugar, hemos presentado un estudio del efecto Faraday en tales estructuras, demostrando que la interacción entre la transmisión óptica

extraordinaria y la actividad magneto-óptica conlleva un aumento de la rotación de Faraday, comparado con membranas puramente ferromagnéticas. En particular, hemos determinado los parámetros geométricos óptimos para maximizar este aumento y demostrado que la inclusión de una capa de un metal noble como el oro aumenta drásticamente la señal magneto-óptica (la conversión de polarización) para un ancho de banda muy amplio. También hemos demostrado que, durante un determinado rango de longitud de onda, la inclusión de la capa de cobalto cerca de las interfaces superior o inferior puede maximizar su uso como rotador de Faraday, es decir, el sistema presenta un muy buen equilibrio entre alta transmitancia y alta rotación de Faraday. Este rendimiento mejorado se atribuye a la excitación de plasmones superficiales polaritones en la capa exterior de oro. Tal y como hemos visto, esta excitación conduce a su vez a un aumento del campo electromagnético en la capa de cobalto, que se refleja en un aumento de la señal magneto-óptica. Por otra parte, hemos visto cómo el análisis de la rotación de Faraday en estas membranas perforadas periódicamente ofrece una mayor comprensión del origen de la transmisión óptica extraordinaria.

Para finalizar, se ha propuesto la utilización de las mencionadas redes periódicas de nano-agujeros híbridos como transductores en sensores magneto-ópticos de resonancia de plasmón superficial, en los que el principio de detección se basa en mediciones del efecto Kerr magneto-óptico en configuración transversal. Hemos presentado un estudio pormenorizado de cómo el uso de estas estructuras híbridas conduce a una tremenda mejora de su rendimiento como sensores plasmónicos, ya que presentan figuras de mérito al menos dos órdenes de magnitud mayores que las de cualquier otro tipo de sensor plasmónico. En este sentido, merece la pena señalar que todavía hay margen para una mayor optimización, por ejemplo, mediante la investigación de diferentes parámetros de red, formas y tamaños de los agujeros, espesor de la membrana, o mediante la ingeniería del sustrato. Además de esto, la técnica de detección propuesta puede hacer uso de las diferentes ventajas que presentan los sensores basados en redes plasmónicas de nano-agujeros tales como la miniaturización, la multiplexación, y su facilidad en la integración con dispositivos de microfluídica. Por lo tanto, estamos seguros de que las redes plasmónicas de nano-agujeros híbridos representarán un importante avance en la tecnología de sensores.

List of publications

- "Generalized scattering-matrix approach for magneto-optics in periodically patterned multilayer systems"
  B. Caballero, A. García-Martín and J. C. Cuevas.
  Physical Review B, vol. 85, p. 245103 (2012)
- "Influence of the magnetic field on the plasmonic properties of transparent Ni anti-dot arrays"
  E. Melander, E. Östman, J. Keller, J. Schmidt, E. Th. Papaioannou, V. Kapalis, U. B. Arnalds, **B. Caballero**, A. Garcia-Martin, J.C. Cuevas and B. Hjörvarsson.
  Applied Physics Letters, vol. 101, p. 063107 (2012)
- "Magnetic field modulation of chirooptical effects in magnetoplasmonic structures"
  G. Armelles, **B. Caballero**, P. Prieto, F. García, A. Cebollada, M. U. González and A. García-Martin.
  Nanoscale, vol. 6, p. 3737 (2014)
- "Magnetic field modification of optical magnetic dipoles"
  G. Armelles, **B. Caballero**, A. Cebollada, A. García-Martín and D. Meneses-Rodríguez.
  Nano Letters, vol. 15, p. 2045 (2015)
- "Observation of a hole-size-dependent energy shift of the surface-plasmon resonance in Ni antidot thin films"
  H. Fang, **B. Caballero**, E. Akinoglu, E. Papaioannou, A. García-Martín, J. C. Cuevas, M. Giersig and P. Fumagalli.
  Applied Physics Letters, vol. 106, p. 153104 (2015)
- "Faraday effect in hybrid magneto-plasmonic photonic crystals"
  B Caballero, A. García-Martín and J. C. Cuevas.
  Optics Express, vol. 17, p. 22238 (2015)
- "Hybrid magnetoplasmonic crystals boost the performance of nanohole arrays as plasmonic sensors"
  B Caballero, A. García-Martín and J. C. Cuevas.
  Submitted to ACS Photonics

Patent

- *"Sensor magnetoplasmónico basado en matrices híbridas perforadas, procedimientos y usos asociados"*
  B. Caballero, A. García-Martín and J. C. Cuevas.
  Patent registration number: P201531817. Date: 16 Dec 2015

Nomenclature

EM	Electromagnetic
EOT	Extraordinary optical transmission
FoM	Figure of merit
LSP	Localized surface plasmon
MO	Magneto-optical
MO-SPR	Magneto-optical surface-plasmon-resonance
MOKE	Magneto-optical Kerr effect
SPP	Surface plasmon polariton
SPR	Surface-plasmon-resonance
TMOKE	Transverse magneto-optical Kerr effect

Bibliography

[1] D. K. Gramotnev and S. I. Bozhevolnyi, "Plasmonics beyond the diffraction limit," Nat. Photonics **4**, 83–91 (2010).

[2] R. Zia, J. A. Schuller, A. Chandran, and M. L. Brongersma, "Plasmonics: the next chip-scale technology," Mater. Today **9**, 20–27 (2006).

[3] E. Ozbay, "Plasmonics: merging photonics and electronics at nanoscale dimensions," Science **311**, 189–93 (2006).

[4] M. Born and E. Wolf, *Principles of Optics* (Cambridge University Press, Cambridge, 1999).

[5] H. Raether, *Surface Plasmons on Smooth and Rough Surfaces and on Gratings*, vol. 111 of *Springer Tracts in Modern Physics* (Springer, Berlin, 1988).

[6] S. A. Maier, *Plasmonics: Fundamentals and Applications* (Springer, New york, 2007), 1st ed.

[7] W. L. Barnes, A. Dereux, and T. W. Ebbesen, "Surface plasmon subwavelength optics," Nature **424**, 824–830 (2003).

[8] J. A. Schuller, E. S. Barnard, W. Cai, Y. C. Jun, J. S. White, and M. L. Brongersma, "Plasmonics for extreme light concentration and manipulation," Nat. Mater. **9**, 193–204 (2010).

[9] A. Sommerfeld, "Ueber die Fortpflanzung elektrodynamischer Wellen längs eines Drahtes," Ann. der Phys. und Chemie **303**, 233–290 (1899).

[10] R. W. Wood, "On a remarkable case of uneven distribution of light in a diffraction grating spectrum," Philos. Mag. Ser. 6 **4**, 396–402 (1902).

[11] R. H. Ritchie, "Plasma Losses by Fast Electrons in Thin Films," Phys. Rev. **106**, 874–881 (1957).

[12] K. A. Willets and R. P. Van Duyne, "Localized surface plasmon resonance spectroscopy and sensing," Annu. Rev. Phys. Chem. **58**, 267–97 (2007).

[13] O. Tokel, F. Inci, and U. Demirci, "Advances in Plasmonic Technologies for Point of Care Applications," Chem. Rev. **114**, 5728–5752 (2014).

[14] M.-C. Estevez, M. A. Otte, B. Sepulveda, and L. M. Lechuga, "Trends and challenges of refractometric nanoplasmonic biosensors: a review," Anal. Chim. Acta **806**, 55–73 (2014).

[15] H. A. Atwater and A. Polman, "Plasmonics for improved photovoltaic devices," Nat. Mater. **9**, 865 (2010).

[16] T. Nikolajsen, K. Leosson, and S. I. Bozhevolnyi, "Surface plasmon polariton based modulators and switches operating at telecom wavelengths," Appl. Phys. Lett. **85**, 5833 (2004).

[17] J. Gosciniak, S. I. Bozhevolnyi, T. B. Andersen, V. S. Volkov, J. Kjelstrup-Hansen, L. Markey, and A. Dereux, "Thermo-optic control of dielectric-loaded plasmonic waveguide components," Opt. Express **18**, 1207–16 (2010).

[18] M. J. Dicken, L. A. Sweatlock, D. Pacifici, H. J. Lezec, K. Bhattacharya, and H. A. Atwater, "Electrooptic modulation in thin film barium titanate plasmonic interferometers," Nano Lett. **8**, 4048–52 (2008).

[19] J. A. Dionne, K. Diest, L. A. Sweatlock, and H. A. Atwater, "PlasMOStor: a metal-oxide-Si field effect plasmonic modulator," Nano Lett. **9**, 897–902 (2009).

[20] D. Pacifici, H. J. Lezec, and H. A. Atwater, "All-optical modulation by plasmonic excitation of CdSe quantum dots," Nat. Photonics **1**, 402–406 (2007).

[21] R. A. Pala, K. T. Shimizu, N. A. Melosh, and M. L. Brongersma, "A nonvolatile plasmonic switch employing photochromic molecules," Nano Lett. **8**, 1506–10 (2008).

[22] K. F. MacDonald, Z. L. Sámson, M. I. Stockman, and N. I. Zheludev, "Ultrafast active plasmonics," Nat. Photonics **3**, 55–58 (2008).

[23] V. V. Temnov, K. A. Nelson, G. Armelles, A. Cebollada, T. Thomay, A. Leitenstorfer, and R. Bratschitsch, "Femtosecond surface plasmon interferometry," Opt. Express **17**, 8423 (2009).

[24] J. González-Díaz, A. García-Martín, G. Armelles, J. García-Martín, C. Clavero, A. Cebollada, R. Lukaszew, J. Skuza, D. Kumah,

and R. Clarke, "Surface-magnetoplasmon nonreciprocity effects in noble-metal/ferromagnetic heterostructures," Phys. Rev. B **76** (2007).

[25] V. V. Temnov, G. Armelles, U. Woggon, D. Guzatov, A. Cebollada, A. Garcia-Martin, J.-M. Garcia-Martin, T. Thomay, A. Leitenstorfer, and R. Bratschitsch, "Active magneto-plasmonics in hybrid metal-ferromagnet structures," Nat. Photonics **4**, 107–111 (2010).

[26] D. Martín-Becerra, J. B. González-Díaz, V. V. Temnov, A. Cebollada, G. Armelles, T. Thomay, A. Leitenstorfer, R. Bratschitsch, A. García-Martín, and M. U. González, "Enhancement of the magnetic modulation of surface plasmon polaritons in Au/Co/Au films," Appl. Phys. Lett. **97**, 183114 (2010).

[27] J. F. Torrado, J. B. González-Díaz, M. U. González, A. García-Martín, and G. Armelles, "Magneto-optical effects in interacting localized and propagating surface plasmon modes." Opt. Express **18**, 15635–42 (2010).

[28] V. I. Belotelov, I. A. Akimov, M. Pohl, V. A. Kotov, S. Kasture, A. S. Vengurlekar, A. V. Gopal, D. R. Yakovlev, A. K. Zvezdin, and M. Bayer, "Enhanced magneto-optical effects in magnetoplasmonic crystals," Nat. Nanotechnol. **6**, 370–6 (2011).

[29] A. Battula, S. Chen, Y. Lu, R. J. Knize, and K. Reinhardt, "Tuning the extraordinary optical transmission through subwavelength hole array by applying a magnetic field," Opt. Lett. **32**, 2692 (2007).

[30] Y. Strelniker and D. Bergman, "Transmittance and transparency of subwavelength-perforated conducting films in the presence of a magnetic field," Phys. Rev. B **77**, 205113 (2008).

[31] V. Belotelov, L. Doskolovich, and A. Zvezdin, "Extraordinary Magneto-Optical Effects and Transmission through Metal-Dielectric Plasmonic Systems," Phys. Rev. Lett. **98**, 077401 (2007).

[32] G. A. Wurtz, W. Hendren, R. Pollard, R. Atkinson, L. L. Guyader, A. Kirilyuk, T. Rasing, I. I. Smolyaninov, and a. V. Zayats, "Controlling optical transmission through magneto-plasmonic crystals with an external magnetic field," New J. Phys. **10**, 105012 (2008).

[33] G. Armelles, A. Cebollada, A. García-Martín, J. M. García-Martín, M. U. González, J. B. González-Díaz, E. Ferreiro-Vila, and J. F. Torrado, "Magnetoplasmonic nanostructures: systems supporting both plasmonic and magnetic properties," J. Opt. A Pure Appl. Opt. **11**, 114023 (2009).

[34] G. Armelles, A. Cebollada, A. García-Martín, and M. U. González, "Magnetoplasmonics: Combining Magnetic and Plasmonic Functionalities," Adv. Opt. Mater. **1**, 10 (2013).

[35] A. V. Kimel, A. Kirilyuk, P. A. Usachev, R. V. Pisarev, A. M. Balbashov, and T. Rasing, "Ultrafast non-thermal control of magnetization by instantaneous photomagnetic pulses," Nature **435**, 655–657 (2005).

[36] C. Hermann, V. Kosobukin, G. Lampel, J. Peretti, V. Safarov, and P. Bertrand, "Surface-enhanced magneto-optics in metallic multilayer films," Phys. Rev. B **64**, 235422 (2001).

[37] B. Sepúlveda, A. Calle, L. M. Lechuga, and G. Armelles, "Highly sensitive detection of biomolecules with the magneto-optic surface-plasmon-resonance sensor," Opt. Lett. **31**, 1085 (2006).

[38] D. Regatos, D. Fariña, A. Calle, A. Cebollada, B. Sepúlveda, G. Armelles, and L. M. Lechuga, "Au/Fe/Au multilayer transducers for magneto-optic surface plasmon resonance sensing," J. Appl. Phys. **108**, 054502 (2010).

[39] D. Regatos, B. Sepúlveda, D. Fariña, L. G. Carrascosa, and L. M. Lechuga, "Suitable combination of noble/ferromagnetic metal multilayers for enhanced magneto-plasmonic biosensing," Opt. Express **19**, 8336 (2011).

[40] M. G. Manera, G. Montagna, E. Ferreiro-Vila, L. González-García, J. R. Sánchez-Valencia, A. R. González-Elipe, A. Cebollada, J. M. Garcia-Martin, A. Garcia-Martin, G. Armelles, and R. Rella, "Enhanced gas sensing performance of TiO2 functionalized magneto-optical SPR sensors," J. Mater. Chem. **21**, 16049 (2011).

[41] M. G. Manera, E. Ferreiro-Vila, A. Cebollada, J. M. García-Martín, A. García-Martín, G. Giancane, L. Valli, and R. Rella, "Ethane-bridged Zn porphyrins dimers in Langmuir-Schäfer thin films: spectroscopic, morphologic, and magneto-optical surface plasmon resonance characterization," J. Phys. Chem. C **116**, 10734–10742 (2012).

[42] M. G. Manera, E. Ferreiro-Vila, J. M. Garcia-Martin, A. Garcia-Martin, and R. Rella, "Enhanced antibody recognition with a magneto-optic surface plasmon resonance (MO-SPR) sensor," Biosens. Bioelectron. **58**, 114–20 (2014).

[43] J. B. González-Díaz, B. Sepúlveda, A. García-Martín, and

G. Armelles, "Cobalt dependence of the magneto-optical response in magnetoplasmonic nanodisks," Appl. Phys. Lett. **97**, 043114 (2010).

[44] J. C. Banthí, D. Meneses-Rodríguez, F. García, M. U. González, A. García-Martín, A. Cebollada, and G. Armelles, "High magneto-optical activity and low optical losses in metal-dielectric Au/Co/Au-SiO(2) magnetoplasmonic nanodisks." Adv. Mater. **24**, OP36–41 (2012).

[45] V. E. Kochergin, A. Y. Toporov, and M. V. Valeiko, "Polariton enhancement of the Faraday magnetooptic effect," J. Exp. Theor. Phys. Lett. **68**, 400–403 (1998).

[46] J. Y. Chin, T. Steinle, T. Wehlus, D. Dregely, T. Weiss, V. I. Belotelov, B. Stritzker, and H. Giessen, "Nonreciprocal plasmonics enables giant enhancement of thin-film Faraday rotation," Nat. Commun. **4**, 1599 (2013).

[47] A. Kuz'michev, L. Kreilkamp, M. Nur-E-Alam, E. Bezus, M. Vasiliev, I. Akimov, K. Alameh, M. Bayer, and V. Belotelov, "Tunable Optical Nanocavity of Iron-garnet with a Buried Metal Layer," Materials (Basel). **8**, 3012–3023 (2015).

[48] L. E. Kreilkamp, V. I. Belotelov, J. Y. Chin, S. Neutzner, D. Dregely, T. Wehlus, I. A. Akimov, M. Bayer, B. Stritzker, and H. Giessen, "Waveguide-Plasmon Polaritons Enhance Transverse Magneto-Optical Kerr Effect," Phys. Rev. X **3**, 041019 (2013).

[49] L. Novotny and B. Hecht, *Principles of Nano-Optics* (Cambridge University Press, Cambridge, 2006).

[50] D. Whittaker and I. Culshaw, "Scattering-matrix treatment of patterned multilayer photonic structures," Phys. Rev. B **60**, 2610–2618 (1999).

[51] S. G. Tikhodeev, A. L. Yablonskii, E. A. Muljarov, N. A. Gippius, and T. Ishihara, "Quasiguided modes and optical properties of photonic crystal slabs," Phys. Rev. B **66**, 045102 (2002).

[52] N. Anttu and H. Q. Xu, "Scattering matrix method for optical excitation of surface plasmons in metal films with periodic arrays of subwavelength holes," Phys. Rev. B **83**, 165431 (2011).

[53] A. García-Martín, G. Armelles, and S. Pereira, "Light transport in photonic crystals composed of magneto-optically active materials," Phys. Rev. B **71**, 1–8 (2005).

[54] M. Liscidini, D. Gerace, L. C. Andreani, and J. E. Sipe, "Scattering-matrix analysis of periodically patterned multilayers with asymmetric unit cells and birefringent media," Phys. Rev. B **77**, 035324 (2008).

[55] F. J. Garcia-Vidal, T. W. Ebbesen, and L. Kuipers, "Light passing through subwavelength apertures," Rev. Mod. Phys. **82**, 729–787 (2010).

[56] T. W. Ebbesen, H. J. Lezec, H. F. Ghaemi, T. Thio, and P. A. Wolff, "Extraordinary optical transmission through sub-wavelength hole arrays," Nature **391**, 667–669 (1998).

[57] L. Martín-Moreno, F. García-Vidal, H. Lezec, K. Pellerin, T. Thio, J. Pendry, and T. Ebbesen, "Theory of extraordinary optical transmission through subwavelength hole arrays," Phys. Rev. Lett. **86**, 1114–1117 (2001).

[58] C. Genet and T. W. Ebbesen, "Light in tiny holes," Nature **445**, 39–46 (2007).

[59] R. Gordon, A. Brolo, D. Sinton, and K. Kavanagh, "Resonant optical transmission through hole-arrays in metal films: physics and applications," Laser Photon. Rev. **4**, 311–335 (2009).

[60] G. Ctistis, E. Papaioannou, P. Patoka, J. Gutek, P. Fumagalli, and M. Giersig, "Optical and magnetic properties of hexagonal arrays of subwavelength holes in optically thin cobalt films," Nano Lett. **9**, 1–6 (2009).

[61] E. T. Papaioannou, V. Kapaklis, M. Giersig, P. Fumagalli, A. Garcia-Martin, E. Ferreiro-Vila, and G. Ctistis, "Magneto-optic enhancement and magnetic properties in Fe antidot films with hexagonal symmetry," Phys. Rev. B **81**, 054424 (2010).

[62] J. F. Torrado, E. T. Papaioannou, G. Ctistis, P. Patoka, M. Giersig, G. Armelles, and A. Garcia-Martin, "Plasmon induced modification of the transverse magneto-optical response in Fe antidot arrays," Phys. status solidi - Rapid Res. Lett. **4**, 271–273 (2010).

[63] E. T. Papaioannou, V. Kapaklis, E. Melander, B. Hjörvarsson, S. D. Pappas, P. Patoka, M. Giersig, P. Fumagalli, A. Garcia-Martin, and G. Ctistis, "Surface plasmons and magneto-optic activity in hexagonal Ni anti-dot arrays," Opt. Express **19**, 23867–77 (2011).

[64] J. B. González-Díaz, A. García-Martín, J. M. García-Martín, A. Cebollada, G. Armelles, B. Sepúlveda, Y. Alaverdyan, and M. Käll,

"Plasmonic Au/Co/Au nanosandwiches with enhanced magneto-optical activity," Small **4**, 202–5 (2008).

[65] C. F. Bohren and D. R. Huffman, *Absorption and Scattering of Light by Small Particles* (Wiley-VCH, Berlin, 1998).

[66] E. Hutter and J. H. Fendler, "Exploitation of Localized Surface Plasmon Resonance," Adv. Mater. **16**, 1685–1706 (2004).

[67] W. L. Barnes, "Surface plasmon-polariton length scales: a route to sub-wavelength optics," J. Opt. A Pure Appl. Opt. **8**, S87–S93 (2006).

[68] A. V. Zayats, I. I. Smolyaninov, and A. A. Maradudin, "Nano-optics of surface plasmon polaritons," Phys. Rep. **408**, 131–314 (2005).

[69] A. Otto, "Excitation of nonradiative surface plasma waves in silver by the method of frustrated total reflection," Z. Phys. **216**, 398–410 (1968).

[70] E. Kretschmann and H. Raether, "Radiative Decay of Non Radiative Surface Plasmons Excited by Light," Z. Naturforsch. A **23**, 2135–2136 (1968).

[71] H. Ditlbacher, J. R. Krenn, N. Felidj, B. Lamprecht, G. Schider, M. Salerno, A. Leitner, and F. R. Aussenegg, "Fluorescence imaging of surface plasmon fields," Appl. Phys. Lett. **80**, 404 (2002).

[72] A. Zvezdin and V. Kotov, *Modern Magnetooptics and Magnetooptical Materials* (IOP Publishing, Bristol, 1997).

[73] S. Sugano and N. Kojima, *Magneto-Optics* (Springer, New York, 2000).

[74] M. Faraday, "Experimental Researches in Electricity," Phil. Trans. R. Soc. Lond. **136**, 1–20 (1846).

[75] J. Kerr, "XLIII. On rotation of the plane of polarization by reflection from the pole of a magnet," Philos. Mag. **3**, 321–343 (1877).

[76] C. Dehesa-Martínez, L. Blanco-Gutierrez, M. Vélez, J. Díaz, L. M. Alvarez-Prado, and J. M. Alameda, "Magneto-optical transverse Kerr effect in multilayers," Phys. Rev. B **64**, 024417 (2001).

[77] M. Plihal and A. A. Maradudin, "Photonic band structure of two-dimensional systems: The triangular lattice," Phys. Rev. B **44**, 8565–8571 (1991).

[78] I. Gohberg, P. Lancaster, and L. Rodman, *Matrix Polynomials* (Academic Press, New York, 1982).

[79] M. Mansuripur, "Analysis of multilayer thin-film structures containing magneto-optic and anisotropic media at oblique incidence using 2x2 matrices," J. Appl. Phys. **67**, 6466 (1990).

[80] M. Neviere and E. Popov, *Light Propagation in Periodic Media: Differential Theory and Design* (Marcel Dekker, New york, 2003).

[81] L. Li, "Use of Fourier series in the analysis of discontinuous periodic structures," J. Opt. Soc. Am. A **13**, 1870 (1996).

[82] E. Popov and M. Nevière, "Maxwell equations in Fourier space: fast-converging formulation for diffraction by arbitrary shaped, periodic, anisotropic media," J. Opt. Soc. Am. A **18**, 2886 (2001).

[83] A. David, H. Benisty, and C. Weisbuch, "Fast factorization rule and plane-wave expansion method for two-dimensional photonic crystals with arbitrary hole-shape," Phys. Rev. B **73**, 075107 (2006).

[84] R. Antos and M. Veis, "Fourier factorization with complex polarization bases in the plane-wave expansion method applied to two-dimensional photonic crystals," Opt. Express **18**, 27511–24 (2010).

[85] E. Melander, E. Östman, J. Keller, J. Schmidt, E. T. Papaioannou, V. Kapaklis, U. B. Arnalds, B. Caballero, A. García-Martín, J. C. Cuevas, and B. Hjörvarsson, "Influence of the magnetic field on the plasmonic properties of transparent Ni anti-dot arrays," Appl. Phys. Lett. **101**, 063107 (2012).

[86] H. Fang, B. Caballero, E. M. Akinoglu, E. T. Papaioannou, A. García-Martín, J. C. Cuevas, M. Giersig, and P. Fumagalli, "Observation of a hole-size-dependent energy shift of the surface-plasmon resonance in Ni antidot thin films," Appl. Phys. Lett. **106**, 153104 (2015).

[87] E. Ferreiro-Vila, J. González-Díaz, R. Fermento, M. González, A. García-Martín, J. García-Martín, A. Cebollada, G. Armelles, D. Meneses-Rodríguez, and E. Sandoval, "Intertwined magneto-optical and plasmonic effects in Ag/Co/Ag layered structures," Phys. Rev. B **80**, 125132 (2009).

[88] P. Poulopoulos, V. Kapaklis, P. E. Jönsson, E. T. Papaioannou, A. Delimitis, S. D. Pappas, D. Trachylis, and C. Politis, "Positive surface and perpendicular magnetic anisotropy in natural nanomorphous Ni/NiO multilayers," Appl. Phys. Lett. **96**, 202503 (2010).

[89] R. Saiki, A. Kaduwela, M. Sagurton, J. Osterwalder, D. Friedman, C. Fadley, and C. Brundle, "X-ray photoelectron diffraction and

low-energy electron diffraction study of the interaction of oxygen with the Ni(001) surface: c(2 x 2) to saturated oxide," Surf. Sci. **282**, 33–61 (1993).

[90] V. Bonanni, S. Bonetti, T. Pakizeh, Z. Pirzadeh, J. Chen, J. Nogués, P. Vavassori, R. Hillenbrand, J. Åkerman, and A. Dmitriev, "Designer magnetoplasmonics with nickel nanoferromagnets." Nano Lett. **11**, 5333–8 (2011).

[91] J. Chen, P. Albella, Z. Pirzadeh, P. Alonso-González, F. Huth, S. Bonetti, V. Bonanni, J. Åkerman, J. Nogués, P. Vavassori, A. Dmitriev, J. Aizpurua, and R. Hillenbrand, "Plasmonic nickel nanoantennas," Small **7**, 2341–7 (2011).

[92] A. A. Grunin, A. G. Zhdanov, A. A. Ezhov, E. A. Ganshina, and A. A. Fedyanin, "Surface-plasmon-induced enhancement of magneto-optical Kerr effect in all-nickel subwavelength nanogratings," Appl. Phys. Lett. **97**, 261908 (2010).

[93] J. F. Torrado, J. B. González-Díaz, G. Armelles, A. García-Martín, A. Altube, M. López-García, J. F. Galisteo-López, A. Blanco, and C. López, "Tunable magneto-photonic response of nickel nanostructures," Appl. Phys. Lett. **99**, 193109 (2011).

[94] S. Visnovsky, V. Parizek, M. Nyvlt, P. Kielar, V. Prosser, and R. Krishnan, "Magneto-optical Kerr spectra of nickel," J. Magn. Magn. Mater. **127**, 135–139 (1993).

[95] K. Mok, C. Scarlat, G. J. Kovács, L. Li, V. Zviagin, J. McCord, M. Helm, and H. Schmidt, "Thickness independent magneto-optical coupling constant of nickel films in the visible spectral range," J. Appl. Phys. **110**, 123110 (2011).

[96] R. W. Wood, "Anomalous Diffraction Gratings," Phys. Rev. **48**, 928–936 (1935).

[97] V. Belotelov and A. Zvezdin, "Magnetooptics and extraordinary transmission of the perforated metallic films magnetized in polar geometry," J. Magn. Magn. Mater. **300**, e260–e263 (2006).

[98] A. B. Khanikaev, A. V. Baryshev, A. A. Fedyanin, A. B. Granovsky, and M. Inoue, "Anomalous Faraday effect of a system with extraordinary optical transmittance," Opt. Express **15**, 6612–22 (2007).

[99] C. Clavero, K. Yang, J. R. Skuza, and R. A. Lukaszew, "Magnetic field modulation of intense surface plasmon polaritons." Opt. Express **18**, 7743–52 (2010).

[100] D. Meneses-Rodríguez, E. Ferreiro-Vila, P. Prieto, J. Anguita, M. U. González, J. M. García-Martín, A. Cebollada, A. García-Martín, and G. Armelles, "Probing the electromagnetic field distribution within a metallic nanodisk," Small **7**, 3317–23 (2011).

[101] J. F. Torrado, J. B. González-Díaz, A. García-Martín, and G. Armelles, "Unraveling the relationship between electromagnetic field intensity and the magnetic modulation of the wave vector of coupled surface plasmon polaritons," New J. Phys. **15**, 075025 (2013).

[102] P. B. Johnson and R. W. Christy, "Optical Constants of the Noble Metals," Phys. Rev. B **6**, 4370–4379 (1972).

[103] F. Przybilla, A. Degiron, J.-Y. Laluet, C. Genet, and T. W. Ebbesen, "Optical transmission in perforated noble and transition metal films," J. Opt. A Pure Appl. Opt. **8**, 458–463 (2006).

[104] A. Krishnan, T. Thio, T. Kim, H. Lezec, T. Ebbesen, P. Wolff, J. Pendry, L. Martin-Moreno, and F. Garcia-Vidal, "Evanescently coupled resonance in surface plasmon enhanced transmission," Opt. Commun. **200**, 1–7 (2001).

[105] A. G. Brolo, R. Gordon, B. Leathem, and K. L. Kavanagh, "Surface Plasmon Sensor Based on the Enhanced Light Transmission through Arrays of Nanoholes in Gold Films," Langmuir **20**, 4813–4815 (2004).

[106] A. De Leebeeck, L. K. S. Kumar, V. de Lange, D. Sinton, R. Gordon, and A. G. Brolo, "On-chip surface-based detection with nanohole arrays," Anal. Chem. **79**, 4094–100 (2007).

[107] G. C. Schatz, J. M. McMahon, and S. K. Gray, "Tailoring the parameters of nanohole arrays in gold films for sensing applications," Proc. SPIE **6641**, 664103–664103–8 (2007).

[108] R. Gordon, D. Sinton, K. L. Kavanagh, and A. G. Brolo, "A new generation of sensors based on extraordinary optical transmission," Acc. Chem. Res. **41**, 1049–57 (2008).

[109] F. Eftekhari, R. Gordon, J. Ferreira, A. G. Brolo, and D. Sinton, "Polarization-dependent sensing of a self-assembled monolayer using biaxial nanohole arrays," Appl. Phys. Lett. **92**, 253103 (2008).

[110] A. Artar, A. A. Yanik, and H. Altug, "Fabry-Pérot nanocavities in multilayered plasmonic crystals for enhanced biosensing," Appl. Phys. Lett. **95**, 051105 (2009).

[111] J.-F. Masson, M.-P. Murray-Méthot, and L. S. Live, "Nanohole arrays in chemical analysis: manufacturing methods and applications," Analyst **135**, 1483–9 (2010).

[112] A. A. Yanik, M. Huang, O. Kamohara, A. Artar, T. W. Geisbert, J. H. Connor, and H. Altug, "An optofluidic nanoplasmonic biosensor for direct detection of live viruses from biological media," Nano Lett. **10**, 4962–9 (2010).

[113] A. A. Yanik, M. Huang, A. Artar, T.-Y. Chang, and H. Altug, "Integrated nanoplasmonic-nanofluidic biosensors with targeted delivery of analytes," Appl. Phys. Lett. **96**, 021101 (2010).

[114] A. A. Yanik, A. E. Cetin, M. Huang, A. Artar, S. H. Mousavi, A. Khanikaev, J. H. Connor, G. Shvets, and H. Altug, "Seeing protein monolayers with naked eye through plasmonic Fano resonances," Proc. Natl. Acad. Sci. U. S. A. **108**, 11784–9 (2011).

[115] A.-P. Blanchard-Dionne, L. Guyot, S. Patskovsky, R. Gordon, and M. Meunier, "Intensity based surface plasmon resonance sensor using a nanohole rectangular array," Opt. Express **19**, 15041–6 (2011).

[116] M. Huang, B. C. Galarreta, A. E. Cetin, and H. Altug, "Actively transporting virus like analytes with optofluidics for rapid and ultrasensitive biodetection," Lab Chip **13**, 4841–7 (2013).

[117] C. Escobedo, "On-chip nanohole array based sensing: a review," Lab Chip **13**, 2445–63 (2013).

[118] A. B. Dahlin, "Sensing applications based on plasmonic nanopores: The hole story," Analyst **140**, 4748–59 (2015).

[119] A. E. Cetin, D. Etezadi, B. C. Galarreta, M. P. Busson, Y. Eksioglu, and H. Altug, "Plasmonic Nanohole Arrays on a Robust Hybrid Substrate for Highly Sensitive Label-Free Biosensing," ACS Photonics **2**, 1167–1174 (2015).

[120] T.-Y. Chang, M. Huang, A. A. Yanik, H.-Y. Tsai, P. Shi, S. Aksu, M. F. Yanik, and H. Altug, "Large-scale plasmonic microarrays for label-free high-throughput screening," Lab Chip **11**, 3596–602 (2011).

[121] A. Lesuffleur, L. Kumar, A. Brolo, K. Kavanagh, and R. Gordon, "Apex-Enhanced Raman Spectroscopy Using Double-Hole Arrays in a Gold Film," J. Phys. Chem. C **111**, 2347–2350 (2007).

[122] M. A. Otte, B. Sepúlveda, W. Ni, J. P. Juste, L. M. Liz-Marzán, and L. M. Lechuga, "Identification of the optimal spectral region

for plasmonic and nanoplasmonic sensing," ACS Nano **4**, 349–57 (2010).

[123] Y. Shen, J. Zhou, T. Liu, Y. Tao, R. Jiang, M. Liu, G. Xiao, J. Zhu, Z.-K. Zhou, X. Wang, C. Jin, and J. Wang, "Plasmonic gold mushroom arrays with refractive index sensing figures of merit approaching the theoretical limit," Nat. Commun. **4**, 2381 (2013).

[124] N. Maccaferri, K. E Gregorczyk, T. V. A. G. de Oliveira, M. Kataja, S. van Dijken, Z. Pirzadeh, A. Dmitriev, J. Åkerman, M. Knez, and P. Vavassori, "Ultrasensitive and label-free molecular-level detection enabled by light phase control in magnetoplasmonic nanoantennas," Nat. Commun. **6**, 6150 (2015).

[125] J. Homola, *Surface Plasmon Resonance Based Sensors* (Springer, New York, 2006).

[126] Y. Ikenoya, M. Susa, J. Shi, Y. Nakamura, A. B. Dahlin, and T. Sannomiya, "Optical Resonances in Short-Range Ordered Nanoholes in Ultrathin Aluminum/Aluminum Nitride Multilayers," J. Phys. Chem. C **117**, 6373–6382 (2013).

[127] A. B. Dahlin, M. Mapar, K. Xiong, F. Mazzotta, F. Höök, and T. Sannomiya, "Plasmonic Nanopores in Metal-Insulator-Metal Films," Adv. Opt. Mater. **2**, 556–564 (2014).

[128] P. Patoka, T. Skeren, M. Hilgendorff, L. Zhi, T. Paudel, K. Kempa, and M. Giersig, "Transmission of light through magnetic nanocavities," Small **7**, 3096–100 (2011).

[129] G. Armelles, B. Caballero, A. Cebollada, A. Garcia-Martin, and D. Meneses-Rodríguez, "Magnetic field modification of optical magnetic dipoles," Nano Lett. **15**, 2045–9 (2015).